

# Laser-cooling and Collisions of Ultracold YO Molecules

by

**Justin J. Bureau**

B.A., University of Washington, 2018

M.S., University of Colorado, Boulder, 2021

A thesis submitted to the  
Faculty of the Graduate School of the  
University of Colorado in partial fulfillment  
of the requirements for the degree of  
Doctor of Philosophy  
Department of Physics  
2024

Committee Members:

Jun Ye, Chair

James K. Thompson

Eric Cornell

John Bohn

Greg Rieker

Burau, Justin J. (M.S Physics)

Laser-cooling and Collisions of Ultracold YO Molecules

Thesis directed by Prof. Jun Ye

Ultracold polar molecules provide an exciting platform for the study of many subfields of physics. Some of the studies include spin-models, quantum information, strongly correlated and exotic phases of matter, ultracold chemistry, and beyond-standard model searches. This makes them a very versatile testbed as any individual molecule could potentially be used for all the above-mentioned studies.

In this thesis, I will describe my work on the direct laser-cooling of molecules, specifically the YO molecule. The work spans over different magneto-optical-trapping mechanisms, sub-Doppler cooling, conservative trapping, and collisional studies. Some of the highlights of my work are the demonstration of the first sub-Doppler molecular MOT, and the study of bulk gas collisions in a true single partial wave regime. In the culmination of this work, we achieve a record phase space density of  $\text{PSD} = 2.5 \times 10^{-5}$  in a bulk dilute gas of YO molecules pushing laser-cooled molecules into the ultracold regime.

## Dedication

To my parents John and Pamela Burau and Yujin Park.

## Acknowledgements

I would like to thank Jun for the opportunity to work on such a challenging and interesting project. Jun was always enthusiastic and supportive and gave me a lot of free reign on the experiment. He always matched my intensity and his passion for physics was always inspiring. Additionally, I would like to thank everyone I worked with over the years including Shiqian, Yewei, Ian, Kameron, Parul, and the newest members of the experiment Mengjie, Simon, and Logan. I would also like to thank all the professors whose passion in the classes I took was infectious and drove me to pursue exciting new routes in the experiment. Also, I would like to thank everyone in Jun's group for the interesting conversations over the years.

I would also like to thank all the groups in JILA as a whole. Over my time at JILA, I do not believe there was a single group where I was not knocking on doors looking for another AOM, optic etc. in the short term to try a new experiment.

## Contents

<b>Chapter</b>	
<b>1</b> Introduction	<b>1</b>
1.1 Why Polar Molecules? . . . . .	1
1.2 Why Ultracold Molecules, and How do We Make Them? . . . . .	3
<b>2</b> Molecular Structure of YO Molecules	<b>6</b>
2.1 Electronic Structure . . . . .	8
2.1.1 Angular Momentum and Hund's Cases . . . . .	9
2.1.2 Term Symbols . . . . .	12
2.1.3 YO Level Structure . . . . .	14
2.1.4 The $A'^2\Delta_{3/2}, J = 3/2^\pm$ State . . . . .	30
2.2 Rotational Transitions . . . . .	35
2.3 Vibrational Transitions . . . . .	38
2.4 Zeeman Splitting . . . . .	39
2.4.1 Zeeman Splitting of $X^2\Sigma^+, N = 0^+, N = 1^-$ . . . . .	39
2.4.2 Zeeman Splitting of $A^2\Pi_{1/2}, J = 1/2^\pm$ . . . . .	40
<b>3</b> Laser-cooling of YO Molecules	<b>45</b>
3.1 Type-I vs. Type-II Transitions . . . . .	45
3.2 Doppler Cooling Theory and Slowing . . . . .	47
3.2.1 Doppler Cooling Theory . . . . .	47

3.2.2	Chirped Laser Slowing . . . . .	51
3.3	Sub-Doppler Cooling . . . . .	57
3.3.1	The Dipole Force . . . . .	57
3.3.2	Polarization Gradient Cooling . . . . .	60
3.3.3	$\Lambda$ -Enhanced Gray Molasses Cooling . . . . .	63
3.3.4	Sub-Doppler Cooling of YO Molecules . . . . .	65
<b>4</b>	<b>Magneto-Optical Trapping of YO Molecules</b>	<b>73</b>
4.1	Theory of Molecular MOTs . . . . .	73
4.2	Dual-Frequency MOT of YO . . . . .	75
4.3	Blue-Detuned MOT . . . . .	80
<b>5</b>	<b>Conservative Trapping of YO Molecules</b>	<b>88</b>
5.1	Technical Implementation of 1064 nm Systems . . . . .	91
5.2	Loading and Cooling of YO Molecules in a 1D Optical lattice . . . . .	97
<b>6</b>	<b>Collisions of YO Molecules</b>	<b>105</b>
6.1	Theory of Ultracold Collisions . . . . .	105
6.2	Collisions of YO Molecules . . . . .	110
<b>7</b>	<b>Conclusion and Future Prospects</b>	<b>121</b>
7.1	Magnetic Trapping . . . . .	121
7.2	Microwave Shielding of YO . . . . .	122
7.3	Narrowline-Cooling of YO Molecules . . . . .	125
	<b>Bibliography</b>	<b>126</b>

## Appendix

## Tables

### Table

2.1	Quantum Numbers . . . . .	11
2.2	Electronic State Parameters . . . . .	14
2.3	Hyperfine Splitting Hamiltonian . . . . .	19
4.1	Type I vs. Type II Cooling Mechanisms . . . . .	76

## Figures

### Figure

1.1	Polar Molecule Applications . . . . .	2
1.2	Energy Scaling of Internal Degrees of Freedom . . . . .	3
2.1	Molecular Degrees of Freedom . . . . .	7
2.2	Hund's Cases . . . . .	10
2.3	Hyperfine Splitting of G States . . . . .	19
2.4	YO Level Structure . . . . .	20
2.5	Ground State Vibrational Potential . . . . .	22
2.6	Vibrational Wavefunctions . . . . .	23
2.7	Frank Condon Factors . . . . .	24
2.8	Branching Ratios Pi State . . . . .	25
2.9	Branching Ratios Delta State N0 and N1 . . . . .	26
2.10	Branching Ratios Delta N2 . . . . .	27
2.11	Branching Ratios Delta N3 . . . . .	28
2.12	Delta State Branching . . . . .	32
2.13	Delta State Stark Splitting . . . . .	33
2.14	Experimental Stark Splitting . . . . .	34
2.15	Microwave Sweeping . . . . .	36
2.16	Rabi Oscillations . . . . .	37

2.17	Zeeman Shift N1 . . . . .	41
2.18	Zeeman Shift N0 . . . . .	42
2.19	Zeeman Shift Pi State . . . . .	43
3.1	Type I vs Type II Transitions . . . . .	46
3.2	DFM Damping Coefficient Simulation . . . . .	49
3.3	Full Laser-cooling Diagram of YO . . . . .	52
3.4	Slowing Tones . . . . .	53
3.5	Experimental Apparatus . . . . .	55
3.6	Slowing Improvement with New Vibrational Repumps . . . . .	56
3.7	Polarization Gradient Cooling . . . . .	60
3.8	$\Lambda$ -Enhanced GMC . . . . .	66
3.9	GMC vs. Intensity and One-photon . . . . .	67
3.10	GMC vs. Two-photon Detuning . . . . .	69
3.11	Temperature Measurement of Molecules . . . . .	70
3.12	GMC vs. Shim Field . . . . .	71
4.1	MOT Type II Transitions . . . . .	75
4.2	DFM Detunings . . . . .	76
4.3	Gradient Coils . . . . .	78
4.4	DFM Properties . . . . .	80
4.5	DFM vs. BDM Tones . . . . .	81
4.6	BDM Scans vs. Intensity . . . . .	83
4.7	BDM Scans vs. Two-photon Detuning . . . . .	84
4.8	BDM Scans vs. One-photon Detuning . . . . .	85
4.9	BDM Properties and Compression . . . . .	86
5.1	Total Polarizability . . . . .	90

5.2	Pointing and Parametric Heating . . . . .	91
5.3	Polarization Stability of Nufern Fiber Amplifier . . . . .	92
5.4	Optics Diagram of Nufern . . . . .	93
5.5	Optics Diagram of Preci . . . . .	94
5.6	1064 nm Beam Propagation . . . . .	95
5.7	ODT vs. Tilt angle . . . . .	98
5.8	Lattice lifetime and Heating Rate . . . . .	99
5.9	Lattice Loading vs. GMC Intensity and Detuning . . . . .	100
5.10	Lattice GMC cooling vs. Two-photon detuning . . . . .	101
5.11	Lattice GMC Cooling vs. Intensity . . . . .	103
6.1	Collisional Theory . . . . .	106
6.2	Van der Waals Potential and XODT Loading . . . . .	112
6.3	Two-Body Loss in N1 . . . . .	114
6.4	State Preparation and Two-Body Loss in N0 . . . . .	116
6.5	Theoretical Collisional Ratios . . . . .	118
6.6	Microwave Shielding Setup . . . . .	120
7.1	magnetictrap . . . . .	123
7.2	microwavetheory . . . . .	124

# Chapter 1

## Introduction

### 1.1 Why Polar Molecules?

Polar molecules provide an exciting and diverse system for probing fundamental physics. Unlike atoms, polar molecules have intrinsic strong electric dipole moments in their body-fixed frames. These moments can be manipulated with either DC or oscillating microwave fields by mixing rotational levels which have extremely long lifetimes allowing for potential, long coherence and storage times. Since a typical electric dipole-dipole interaction in polar molecules is ten thousand times stronger than that of typical magnetic dipole-dipole interactions, the applications with polar molecules cover a wide variety of fields. Some of these applications include simulating spin models [44, 14], quantum information [35, 5, 24, 52, 40, 61, 82], ultracold chemistry [46, 66, 15], searches for the electron EDM [58, 2], the promise to study strongly correlated phases [10, 23] and exotic states of matter [56, 32, 63]. Figure 1.1 shows some of these applications diagrammatically.

We see that these applications are broad and cover many aspects of different physical fields. Spin models, strongly correlated phases, and exotic phases of matter probe interesting condensed matter physics which can be difficult to simulate due to the sheer number of interacting particles. Searches for the electron EDM with polar molecules allow tabletop experiments to probe wide mass ranges of potential beyond standard model particles which are out of reach even today at large facilities like the LHC, and place tight constraints on potential beyond standard model theories such as SUSY. Polar molecules are an interesting platform for quantum information as the rich internal structure could allow for shelving and continuous loading of qubits mid-operation and

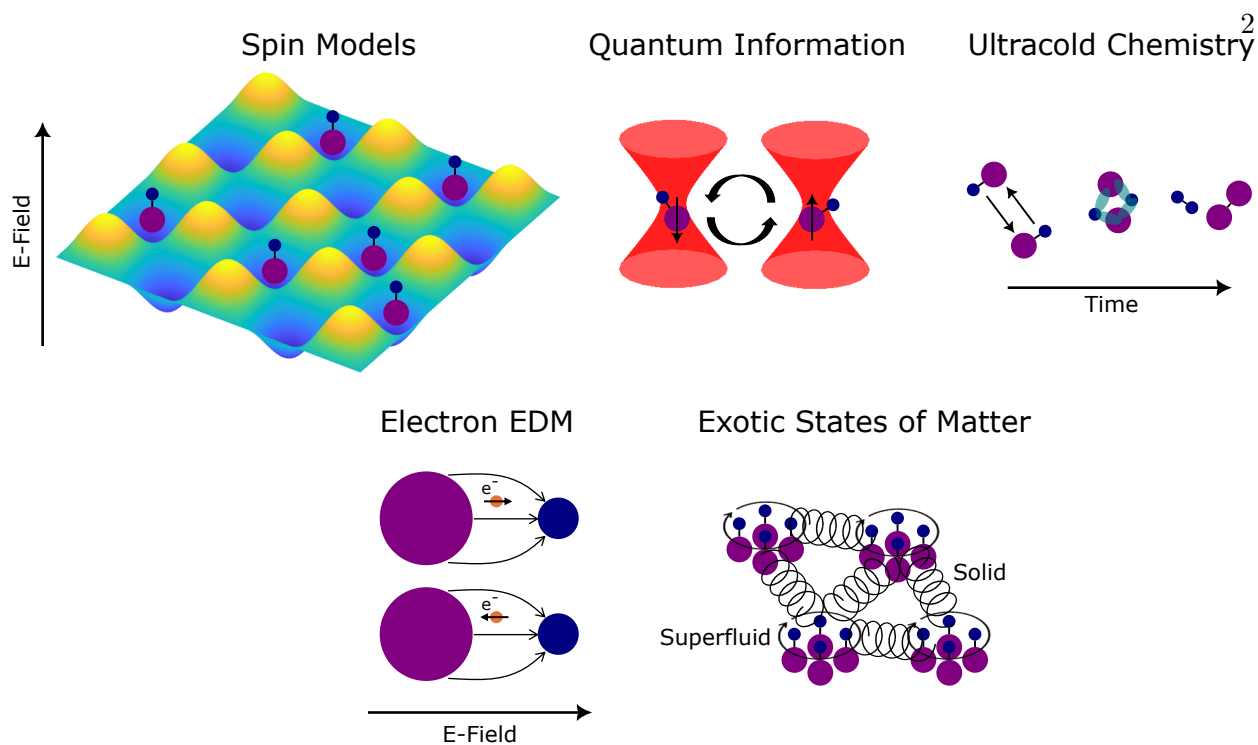


Figure 1.1: Shown are some applications of polar molecules to probe and study different fundamental physics.

also mid-circuit readout for error correction. Since the interaction is based on electric dipole-dipole interactions the range of these interactions is quite long and coherent Rabi oscillations have already been seen between optical tweezers several  $\mu\text{m}$  apart. Ultracold chemistry with polar molecules is an exciting avenue. At ultracold temperatures, arbitrary state preparation can be done and only the lowest partial wave is dominant in the scattering cross-section between the molecules. As such, tight control over the system can be achieved and intermediate reaction products and the resulting reactant products can be detected vs. time. This allows a measurement of the intermediate complex lifetimes and quantum state mapping of the products depending on the initial state preparation which is a difficult problem for ab initio theory.

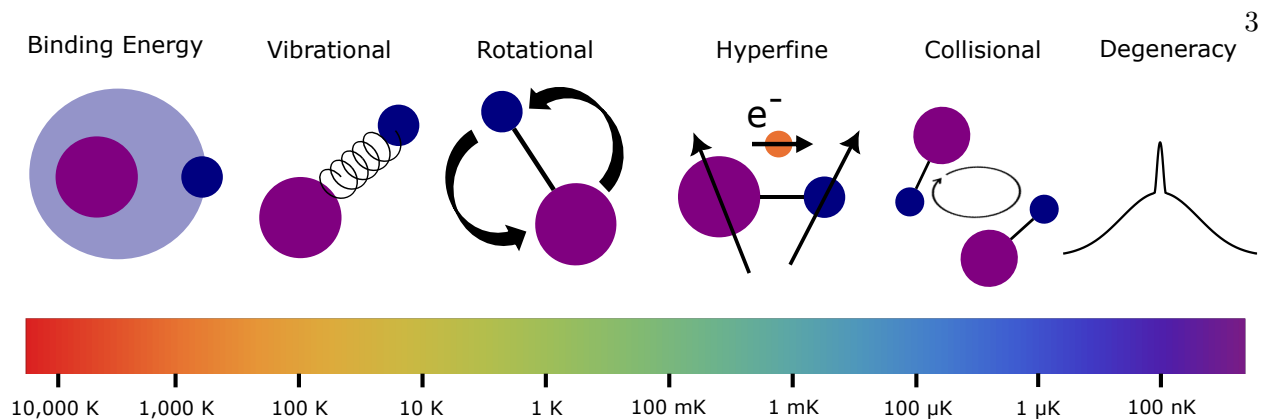


Figure 1.2: The relevant energy scaling of molecular degrees of freedom and interactions are shown vs. temperature.

## 1.2 Why Ultracold Molecules, and How do We Make Them?

Before discussing why and how to make ultracold molecules it is useful to define the definition of ultracold. Generally in the field of AMO physics, the rule of thumb is that ultracold corresponds to a velocity distribution with an average temperature of  $< 1 \mu\text{K}$ . This definition is a good rule of thumb, however it does miss much of the physics involved in ultracold gases. A better definition that I prefer is ultracold is defined as when the collisional processes of a distinguishable dilute gas of atoms or molecules are dominated only by one partial wave. In this definition, the intrinsic properties of the molecules are accounted for depending on the interaction typically dipole-dipole or van der Waals along with the centrifugal barrier heights. If this condition is met then the collisional cross-section can be defined as a simple hard sphere scattering with a characteristic scattering length  $a$ , and in this limit, the temperature of the gas would be called ultracold.

The reason we want the molecules to be in the ultracold regime is if the temperature of the molecules is high then the intrinsic properties of the molecule are "bleached" out from Doppler broadening of the relevant degrees of freedom. In this case, we cannot take advantage of the unique properties of the molecules in the true quantum regime. Additionally, many of the fundamental physics that one would study with molecules rely on well-controlled coherent interactions with

applied optical, microwave, or DC fields which again are compromised if the ensemble thermal energy of the gas is too high. The relevant energy scaling of a typical diatomic molecule is shown in Fig.1.2. We see from the figure that to access the ultracold regime the molecules need to be at extremely low temperatures at around  $1 \mu\text{K}$ . To reach degeneracy the molecules need to be cooled even further typically through evaporative cooling to temperatures around  $100 \text{ nK}$  or lower.

By far the most successful way to produce molecules at ultracold temperatures is through the association of atoms. This is done by laser-cooling two atomic species generally alkali earth atoms which are the most simple atoms to laser cool and associating them through a Feshbach resonance as these atoms also have  $1 \mu_B$  magnetic moment in their ground state. STIRAP pulses are then applied to coherently transfer the molecules into their absolute ground state. This methodology was first used in our lab on KRb molecules [51] and has become widely successful in creating dense gases of dipolar molecules [33, 50, 55, 59, 71]. Additionally, with shielding of inelastic loss three molecular species have been brought to quantum degeneracy [22, 75, 62, 13, 7].

Thus far, no directly laser-cooled molecule has been brought to degeneracy, and only really in this work on YO molecules can you say that laser-cooled molecules have finally made it to the ultracold regime with a bulk dilute gas. However, laser-cooled molecules have advantages over magneto-associated molecules. One advantage is molecular readout can be done without destroying the molecules which will be an advantage in the future particularly when the experiment demands in-situ readout of different internal spin states in the molecule. Additionally, molecules that can be laser-cooled are generally found in nature and are much more exciting for ultracold chemistry studies. Also, a much wider array of molecules can be laser-cooled including heavier molecules for EDM studies including polyatomic molecules.

In this thesis, I will only concentrate on laser-cooling YO molecules. This molecule is unique in its level structure, and it has been found in this work that YO molecules are very amenable to laser-cooling and achieve the highest phase space densities of any laser-cooled species both in free space, magneto-optical-traps, and in conservative traps. With its large dipole moment of  $4.5 \text{ Debye}$  in the ground state, it remains a very exciting molecule for studying Bose-Hubbard spin models

and exploring exotic states of matter.

## Chapter 2

### Molecular Structure of YO Molecules

Before discussing laser-cooling and preparation of cold molecules in single quantum states, it is necessary to understand the structure of molecules and their additional degrees of freedom. In this thesis, we will only concentrate on the structure of diatomic molecules, in particular, the YO molecule. However many of the facets that will be discussed apply to polyatomics except with reduced symmetry. Molecules enjoy important properties of atoms in that oscillating electric and magnetic fields can resonantly drive electronic transitions between atomic orbitals, and static fields can shift the internal energy of individual spin states. This allows for state manipulation and cooling to ultralow temperatures. However, molecules have additional degrees of freedom in that they can vibrate and rotate. These vibrations and rotations can also be manipulated with oscillating and static fields in heteronuclear molecules that are not present in atoms. It is precisely these extra degrees of freedom that create a physical system unique for certain fundamental studies.

A diagram of the relevant energy scaling of electronic, vibrational, and rotational states is shown in Fig.2.1. The scaling of electronic transitions matches well with alkali and alkaline earth metals used in typical AMO experiments with transition frequencies of several hundred THz lying within or just outside the visible. The next energy scale is vibrational which creates a large density of states in each electronic state. The frequency span between vibrational levels is typically in the tens of THz range. It is important to note that as the vibrational quantum number increases the spacing of the vibrational levels decreases showing a prominent anharmonicity.

This of course makes sense as the equilibrium position of the nuclei increases with increasing

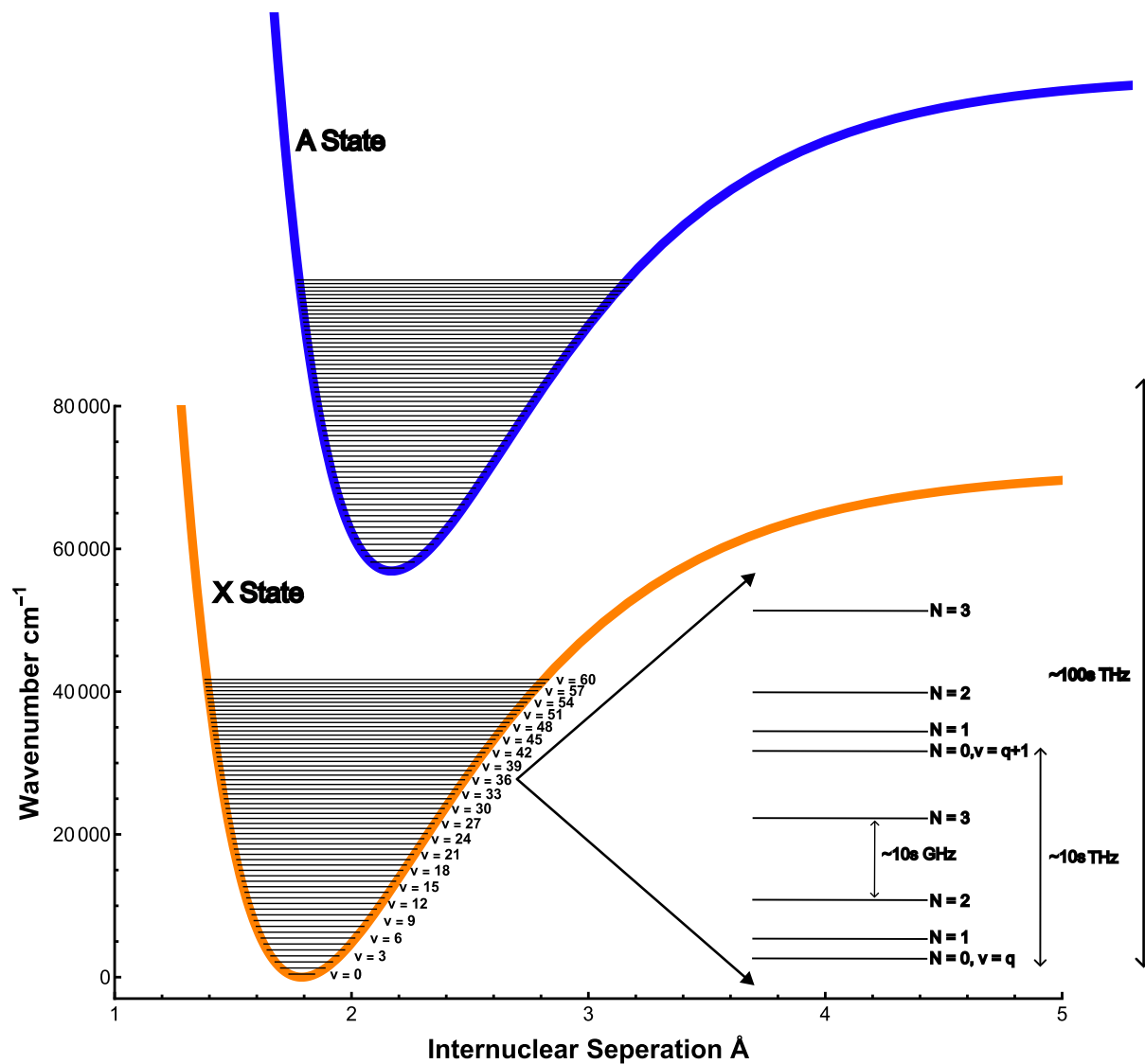


Figure 2.1: Unlike atoms, molecules have additional degrees of freedom in that they can vibrate and rotate. The electronic, vibrational, and rotational degrees of freedom have drastically different energy scalings associated with them as shown diagrammatically above.

vibrational quanta, the electrostatic force between the atoms must decrease until the molecules disassociate. This can be seen with the tailing off of the potential energy curves in Fig.2.1. The next energy scale is rotational which has typical energy spacings of 1-10 GHz for the lowest rotational transitions. This further increases the densities of states as now every electronic state has a ladder of vibrational energy levels and every vibrational level has a ladder of rotational levels. In addition to vibrational and rotational levels, there are the familiar fine structure and hyperfine structure from electron and nuclear spin couplings that add even more states which will be discussed in detail later. These contributions typically have splittings of 10s of THz and 1-0.001 GHz respectively, and will be discussed in detail later.

It now appears daunting to attempt to laser cool even the most simple of molecules due to the large density of states. However, these contributions are well resolvable, and choosing molecules with the right properties and being a little clever allows for efficient cooling, trapping, and manipulation of the molecules. Additionally, the beauty of molecules is revealed with this complex structure in that they can be coherently manipulated over a wide range of the electromagnetic spectrum from the visible to rf. The next few sections are dedicated to each degree of freedom discussed above in more detail.

## 2.1 Electronic Structure

We are mainly interested in achieving expressions for the electric transition dipole moments (E1) between the various degrees of freedom in the molecule as these matrix elements reveal information on the ability to manipulate the molecules with microwave and laser fields. In this thesis, we ignore any weak forbidden transitions (M1 and E2). As such, to find the matrix elements we need to determine the various wavefunctions for each internal state which immediately does not seem like an easy task given the complexity of the internal structure of the molecule. However, a powerful approximation is generally valid that greatly simplifies the effect of each contribution to the molecular structure into a simple product of the individual wavefunctions.

This approximation is called the Born-Oppenheimer approximation which states that the

ratio of electronic and nuclear energy levels is given by [9] (Chapter 2.1),

$$\frac{\Delta E_{nucl}}{\Delta E_{electronic}} \approx \left(\frac{m}{M}\right)^{1/2}, \quad (2.1)$$

where  $m$  is the mass of the electron and  $M$  is the mass of the nuclei. This means that the acceleration of the electrons from the electrostatic interaction is much greater than that of the nuclei. As such, the velocities experienced are much higher, and electron dynamics happen on a time scale of 1 fs. In the molecule fixed frame, the nuclei can be considered fixed in space. This is further extended as the nuclear motion of vibration and rotation is also weighted in their energy by further powers of the mass ratio. This allows us to write the total molecular Hamiltonian to a very good approximation as the sum of the electronic, vibrational, and rotational degrees of freedom and the total wavefunction as a simple product,

$$|\Psi_{Molecule}\rangle = |\Psi_{Electronic}\rangle \times |\Psi_{Vibrational}\rangle \times |\Psi_{Rotational}\rangle. \quad (2.2)$$

This product allows an intuitive calculation of the transition dipole moments for electronic transitions.

### 2.1.1 Angular Momentum and Hund's Cases

Due to the numerous magnetic couplings present in molecules every electronic state has a different set of "good quantum numbers" depending on the energy scaling of molecular interactions. The order of coupling and the good quantum numbers are well described diagrammatically by Hund's cases. The quantum numbers relevant to cooling YO molecules are given in the Table.2.1. Most of these quantum numbers are familiar to atomic systems with the addition of the vibrational and rotational quantum numbers. The Hund's cases describing the angular momentum coupling are given in Fig.2.2.

The first coupling case that will be discussed is Hund's case (a). In this case, the electrostatic interaction between the nuclei is much greater than the spin-orbit interaction, which is much greater

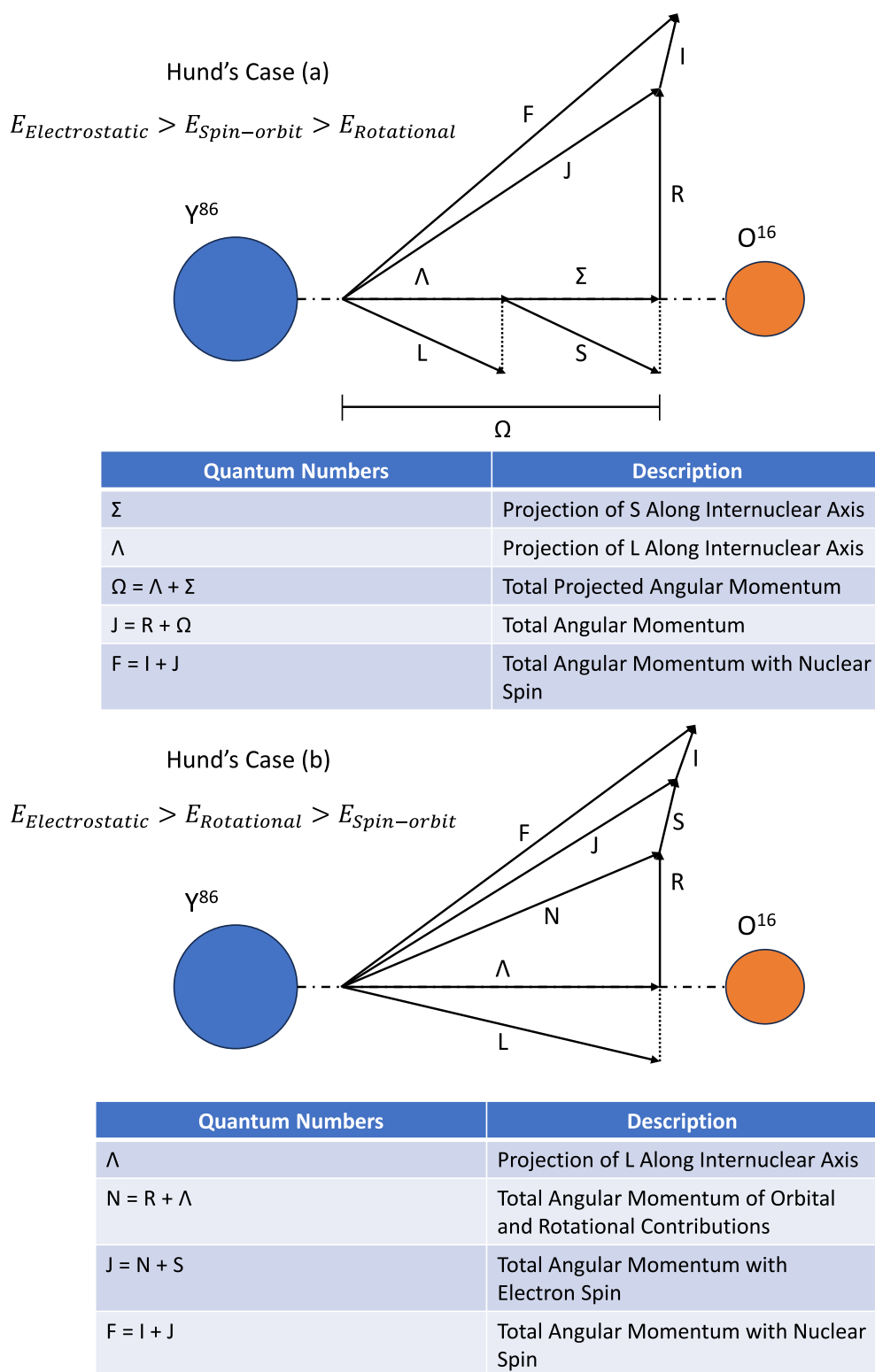


Figure 2.2: Shown are the angular momentum coupling cases relevant to the YO molecule. Hund's case (a) describes the coupling in  $A^2\Pi_{1/2}$  and  $A'^2\Delta_{3/2}$  states. Hund's case (b) describes the coupling in the  $X^2\Sigma^+$  and  $B^2\Sigma^+$  states.

Quantum Numbers	
Symbol	Definition
<b>I</b>	<b>Total Nuclear Spin of Nuclei</b>
<b>S</b>	<b>Total Electron Spin of Relevant Valence Electrons</b>
<b>L</b>	<b>Total Orbital Angular Momentum of Valence Electrons</b>
<b>R</b>	<b>Total Angular Momentum from Rotation of Nuclei</b>
<b>v</b>	<b>Total Number of Vibrational Quanta</b>

Table 2.1: Description of the relevant quantum numbers for laser-cooling of YO molecules.

than the rotational energy [8]. As reference the typical energy spacing between electronic levels is  $\approx 10000 \text{ cm}^{-1}$ , the spin orbit interaction has energy of  $\approx 100 \text{ cm}^{-1}$  and the rotational energy is of order  $\approx 1 \text{ cm}^{-1}$ . The strong electrostatic energy locks the electronic orbital angular momentum  $L$  to precess around the internuclear axis of the nuclei. The spin-orbit interaction is strong enough to cause the electron spin to also precess along the internuclear axis as the rotational energy is very small. As such, the orbital angular momentum and the spin angular momentum have projections along the internuclear axis with quantum numbers  $\Lambda$  and  $\Sigma$ . The sum of these two projections is defined as  $\Omega$  as shown diagrammatically in the top representation in Fig.2.2.  $\Omega$  then couples to  $R$  to form the total angular momentum  $J$  excluding nuclear spin. Adding, nuclear spin  $I$  couples to  $J$  to form  $F$ . Hund's case (a) is a good representation of the excited electronic states that are used prominently throughout the rest of this work for Doppler cooling. One interesting consequence of the coupling of the orbital angular momentum to the internuclear axis is the projection of  $\Lambda$  is degenerate as it can be projected towards either nuclei. This actually has a profound effect on the electronic structure with states with non-zero  $\Lambda$ . This degeneracy is known as lambda doubling and creates two states with opposite parity that can be represented as linear combinations of the different angular momentum projections. This degeneracy is lifted due to second-order spin-orbit coupling and the rotational Coriolis effect [9] (pg. 328). Due to coupling with other states with projection  $|\Lambda| - 1$ , lambda doubling has the largest effect for states which have angular projection  $|\Lambda| = 1$ .

The second case is Hund's case (b) and occurs when the electrostatic interaction is still the

largest interaction, but the rotational interaction is larger than the spin-orbit interaction. In this case, the orbital angular momentum is still projected along the internuclear axis however since the spin-orbit term is small the electron spin does not couple strongly to the internuclear axis. As such,  $\Lambda$  couples to  $R$  first to form  $N$ , which then couples to  $S$  to form  $J$ .  $J$  then couples to  $I$  to form  $F$ . Hund's case (b) will be important for states with  $\Lambda = 0$  such as the ground state of the YO molecule and future possible repumping on higher excited states. Since  $\Lambda = 0$ , there are no parity doublets in the ground state of YO. Instead, states of opposite parity are formed by the rotational ladder in each vibrational manifold which allows E1 transitions between different rotational states. Another interesting aspect to note is that Hund's cases are only really true in the lowest rotational manifolds. If the rotational manifolds become increasingly populated the spin-orbit interaction breaks down and the good quantum numbers can change as the transition to a different Hund's case occurs.

### 2.1.2 Term Symbols

Now with an understanding of the relevant magnetic couplings of the different angular momenta, how do you label a particular quantum spin state? The labeling is given below for a heteronuclear diatomic molecule and specifically for the YO molecule, and is quite similar to the term symbols used for atoms except with the additional degrees of freedom,

$$v = (0, 1, 2\dots), K^{2S+1}\Lambda_{\Omega}^{\pm}, J = \Omega + (R = 0, 1, 2\dots), (G), F, m_F \quad (2.3)$$

the first term simply represents the vibrational level with the associated occupied electronic state which was previously shown in Fig.2.1. The second term is a term that is similar to the labeling of the atomic states. Here  $K$  is just a placeholder and will not be seen throughout the rest of this thesis. The values of  $K$  are letters labeled, X,A,B,C... and denote the relative energy scaling of the electronic state. X is reserved for the ground state, the first excited state A, the next excited state B... and so on. This convention however is not followed and you will see interesting states like A' which simply means that transition was found at a later time and had lower energy than the

previously labeled states.  $S$  is the total spin of the valence electrons and YO which has one valence electron is fixed to  $S = 1/2$  indicating spin doublets. The  $\Lambda$  term had been previously defined for both Hund's case (a) and (b). The labeling convention takes the form of  $\Lambda = 0,1,2,\dots \rightarrow \Sigma, \Pi, \Delta, \dots$ . An important note is that this  $\Sigma$  has nothing to do with the projection of the electron spin and is simply a label.  $\Omega$  has been previously defined and can be thought of as essentially denoting the spin-orbit state for nonzero  $\Lambda$ . The plus or minus superscript denotes the reflection symmetry of the state with a plane that contains the internuclear axis and is only valid for states with  $\Lambda = 0$ . The next term is the total angular momentum  $J$  and takes values from  $J = \Omega + (R = 0,1,2,\dots)$ . In  $\Sigma$  states the quantum number  $R = N$  as  $\Lambda$  is zero. As such, throughout this thesis, the rotational states will be labeled  $N$  in the ground state. The next quantum number  $G$  is a special case that is only applicable to  $\Sigma$  states in YO like the ground state. It is defined as  $G = I + S$  and has to do with the fact the YO has a massive Fermi contact interaction. This means the electron spin density with the  $Y^{89}$  nucleus, which has a nuclear spin  $I = 1/2$ , is large ( $O^{16}$  has no nuclear spin). It is so large the Hund's case (b) scheme described earlier is altered as  $I$  and  $S$  first couple together and then couple to the rotation. This is critically important and is responsible for many of the facets of laser-cooling and in particular the hyper-efficient ground state sub-Doppler cooling present in YO molecules. A simple basis transformation for  $G$  is given by a Wigner 6-J matrix that allows a transformation to the standard Hund's case (b) with more specific details given in [9] (pg.156) and [83],

$$|((I, S)G, N), F\rangle = \sum_J (-1)^{S+I+F+N} ((2G+1)(2J+1))^{1/2} \begin{Bmatrix} I & S & J \\ N & F & J \end{Bmatrix} |(I, (S, N)J), F\rangle. \quad (2.4)$$

While this expression may seem intimidating to a young grad student reading this thesis, such expressions are extremely common as transformations to different bases happen constantly when discussing molecules as shown in the previous section. However this expression is straightforward to understand and states exactly what was stated in the previous paragraph, the ket on the left-hand side states  $I$  and  $S$  couple together to first form  $G$ , which then couples to  $N$  to form  $F$ . This can

be represented with a Wigner-6J symbol as three angular momenta are being coupled with some prefactors summed over J times the ket on the right-hand side which is the standard Hund case (b) coupling where S and N couple together to form J, which then couples to I to form F.

### 2.1.3 YO Level Structure

YO Spectroscopic Parameters				
Electronic Level Symbol	Orbital Configuration	Lifetime $\tau$	Linewidth $\Gamma/(2\pi)$	Intrinsic Dipole Moment
$X^2\Sigma^+$	$11\sigma^1 15\pi^4 12\sigma^1$	<b>NA</b>	<b>NA</b>	<b>4.5 D</b>
$A^2\Pi_{1/2}$	$11\sigma^1 15\pi^4 6\pi^1$	<b>33 ns</b>	<b>4.8 MHz</b>	<b>3.7 D</b>
$A'^2\Delta_{3/2}$	$11\sigma^1 15\pi^4 2\delta^1$	<b>23 <math>\mu</math>s</b>	<b>6.9 kHz</b>	<b>7.5 D (Theory)</b>
$B^2\Sigma^+$	$11\sigma^1 15\pi^4 13\sigma^1$	<b>30 ns</b>	<b>5.3 MHz</b>	<b>1.7 D (Theory)</b>

Table 2.2: Molecular orbital configurations, lifetimes, and dipole moments of relevant electronic states for laser-cooling [65, 85].

Now that molecular term symbols and the different angular momenta cases have been described, we can turn to the molecule relevant to this thesis. That molecule, is the  $Y^{86}O^{16}$  molecule pronounced yttrium-monoxide. It is an interesting molecule that consists of an element residing in the rare earth third column of the periodic table and of oxygen. This molecule has been the study of numerous theoretical and experimental articles as this molecule is prominent in astrophysical observations around cool stars [65]. Additionally, it acts as a test bed for ab-initio studies of open-shell transition metal diatomic molecules [65].

The relevant states, orbital configurations, lifetimes, and dipole moments are given in Table.2.2. We see that in the absolute ground state,  $X^2\Sigma^+$  YO features a large permanent dipole moment of 4.5 Debye that makes it very suitable for fundamental quantum simulation studies. Additionally, its appreciably large mass of 105 amu provides low recoil temperatures for sub-Doppler cooling. YO features excited states namely the  $A^2\Pi_{1/2}$  that has a short lifetime of 33 ns allowing scattering large amounts of photons for laser-cooling in a short amount of time. Uniquely to current trapped laser-cooled molecules YO features an intermediate  $A'^2\Delta_{3/2}$  state with a lifetime of 23  $\mu$ s that allows for recoil-limited cooling in traditional optical molasses. YO also is an open shell molecule as seen from the orbital configurations meaning that a strong magnetic moment exists in

the ground state allowing for ground state cooling and also magnetic trapping.

Successful laser-cooling is facilitated by scattering photons off a strong transition normally in the optical or near IR spectral region. The spontaneous emission rate is given by the well-known equation below which can be derived from the Wigner-Weisskopf theory of coupling of excited electronic states to vacuum modes,

$$\Gamma_{spon} = \sum_i \frac{\omega_{i \rightarrow e}^3 |\langle \Psi_e | \mu | \Psi_i \rangle|^2}{3\pi\epsilon_0 \hbar c^3} \quad (2.5)$$

where  $\omega$  is the angular transition frequency. As such, the higher the transition frequency the higher the spontaneous emission rate and the higher the photon scattering rate. The sum over  $i$  is the sum over all lower energy states to a particular excited state in the molecule given by  $|\Psi_e\rangle$ . Here  $\langle \Psi_i | \mu | \Psi_g \rangle$  is the matrix elements of the transition dipole moment. These matrix elements are the single most important expressions for laser-cooling of a molecule or atom! In the following discussion, we assume only E1 transitions and the dipole moment are induced by the interacting laser field. To understand why this expression is so important we will write out the definition in the Born-Oppenheimer approximation discussed earlier, and we will analyze each term. Analyzing each term in the expression reveals what molecules can and can't be laser-cooled and why YO does meet the criteria for laser-cooling. The transition dipole moment is defined in [9] (pg. 269) and is,

$$\mu_e = \left[ \int_{\alpha} \psi_v^*(R_{\alpha}) \psi'_v(R_{\alpha}) dV_{\alpha} \right] \times [\langle J, M_J | \mu | J', M'_J \rangle] \times \left[ -e \int_k \psi_v^*(r_k, R_{\alpha}) \sum_k r_k \psi'_v(r_k, R_{\alpha}) dV_k \right]. \quad (2.6)$$

Here  $k$  represents the  $k$ th electron,  $\alpha$  represents the  $\alpha$ th nucleus,  $r_i$  is the position of each electron,  $R_{\alpha}$  is the position of the nuclei,  $J$  and  $M_J$  are the total angular momenta and its projection along the internuclear axis,  $e$  is the charge of the electron, the prime subscript represents the lower energy electronic level. An important point that needs to be reemphasized is the three terms here are all intrinsic properties of the molecule. The first term represents the overlap of the vibrational wavefunctions and its square is known as the Frank-Condon factors. This term is the most stringent

term for what molecules can be laser cooled and may be familiar to those who perform cooling to the ground band in tightly confining optical traps or ion traps. The second term is the geometric factor from the different angular momenta between the excited and lower energy state. We will see clever choices of the internal states limit the branching from this term. The last term is the familiar term for the transition moment in atoms which is just the matrix elements of the position operator.

We will begin with the third term, the term boils down to choosing molecules with strong dipole-allowed transitions. This term is normally deduced from performing fluorescence spectroscopy and looking at the decay after exciting a particular state. Once the lifetime is known both Eq.2.6,2.5 can be used to determine its magnitude. If no spectroscopy is known sophisticated coupled cluster methods can be used to roughly determine this term [84]. Generally, this term is not the limiting factor for laser-cooled molecules and strong excited state transitions normally exist. In YO as stated previously numerous strong transitions exist so we already have one-third of Eq.2.6 accounted for in favor of cooling YO molecules.

### 2.1.3.1 Frank-Condon Factors and Energy Level Diagrams of YO

To determine the Frank-Condon factors we will need to calculate the vibrational wavefunctions and perform the integral in the first term in Eq.2.6. To do so we need to have a Hamiltonian (that is hopefully simple) to define the energy level structure that we can use to diagonalize Schrodinger's equation. We can make a simple approximation of what a diatomic molecule is in a semi-classical picture. The approximation is to assume that a diatomic molecule is an anharmonic non-rigid rotor [9] (pg. 243). The picture of this is a spring connecting to the two nuclei that have higher order distortion constants to approximate the anharmonicity to a harmonic oscillator. In the vibrating rotor approximation as the molecule vibrates the moment of inertia changes of the molecule changes which creates a mean rotational constant,

$$B_v = \frac{h}{8\pi^2 c \mu} \left( \frac{1}{\bar{R}^2} \right) \quad (2.7)$$

where  $R$  is the distance between the nuclei and is averaged over the motion [9] and  $\mu$  is the reduced mass of the nuclei. Additionally, as the molecule rotates faster the equilibrium position also increases, and is known as centrifugal distortion. This adds higher-order constants to deal with the divergence from a rigid rotor.

In these approximations, we will write down two equations. The first will describe excited  $^2\Pi$  and  $^2\Delta$  states and the second will describe  $^2\Sigma$  states. The equations are as follows,

$$\begin{aligned}
 H_{\Pi,\Delta} &= T_v \pm A_{v,J} + B_v J(J+1) - D_v J^2(J+1)^2 + H_v J^3(J+1)^3 + (-1)^{\pm 1 + J - 1/2} (p_{v,J} + 2q_{v,J})(J+1/2)/2 \\
 A_{v,J} &= A_v + AJ_v(J(J+1)) + AJJ_v(J^2(J+1)^2) \\
 p_{v,J} &= p_v + pJ_v(J(J+1)) + pJJ_v(J^2(J+1)^2) \\
 q_{v,J} &= q_v + qJ_v(J(J+1)).
 \end{aligned}
 \tag{2.8}$$

The first term  $T_v$  describes the energy offset of the particular electronic state and the specific vibrational state in that electronic state. The subscript  $v$  on all the terms absorbs the anharmonic distortion of the constants into the constants themselves. What this means is for every vibrational state in each electronic state there is a new set of constants to describe that state. The next in the top equation with the  $\pm$  is the spin-orbit constant where the sign denotes the state of interest for example  $A^2\Pi_{1/2}$  or  $A^2\Pi_{3/2}$ . The next three terms should seem familiar and are just the energy levels of a rigid rotor with higher order terms  $D_v$  and  $H_v$  to account for the centrifugal distortion where  $J$  is the total angular momentum excluding nuclear spin. Here we explicitly write out the centrifugal distortion terms and do not absorb them into each constant. The last term describes the lambda doubling which was described earlier in the discussion with Hund's cases. The terms  $p_{v,J}$  and  $q_{v,J}$  describe the admixing states with  $|\Lambda| - 1$  which lifts the degeneracy of the parity doublet [9] (pg. 531). The next three equations describe the centrifugal distortion of the spin-orbit constant and lambda doubling constants. The spin-orbit constants  $AJ_v$  and  $AJJ_v$  represent the higher-order distortion constants. The same notion is followed for both  $p_{v,J}$  and  $q_{v,J}$ .

The second equation applicable to  ${}^2\Sigma$  states is simpler as there is no parity doublets or spin-orbit coupling. It is as follows,

$$H_{\Sigma} = T_v + B_v N(N + 1) - D_v N^2(N + 1)^2 + H_v N^3(N + 1)^3 \quad (2.9)$$

where the constants have the same definition as before however  $J$  has been replaced by  $N$ . This is great for describing rotational splitting however, we care deeply about the exact hyperfine ground state structure to account for the electron and nuclear spin. Therefore we will add in an effective Hamiltonian which describes their unique coupling to form  $G$ . The Hamiltonian that describes the hyperfine splitting is the Frosch and Foley Hamiltonian given as [9] (pg. 935),

$$H_{\text{hyperfine}} = \gamma_v S \cdot N + b_v I \cdot S + c_v I_z S_z + C_{I,v} I \cdot N, \quad (2.10)$$

where the constants  $\gamma_v, b_v, c_v$  and  $C_{I,v}$  represent the strength of the spin-rotation, contact, dipolar, and nuclear spin-rotation interactions. Each of these constants again is dependent on each vibrational manifold accounting for any anharmonicity. Additionally, the constants also are dependent on the specific rotational level with higher-order distortion terms added to them. This effective Hamiltonian is quite complicated to diagonalize and good references discussing each term are given in [83] and [9] (pg. 746). Here we just quote the result and its consequences on the level structure. First, we introduce two new constants  $b_{f,v} = b_v + t_v$  and  $t_v = c_v/3$  which are called the Fermi-contact constant and the dipolar hyperfine term. The Hamiltonian only diagonal in  $N$  takes the form of given in Table.2.3. We see that the triplet states in  $G = 1$  from the coupling of  $I$  and  $S$  are lifted by the spin-rotation interaction. This is shown diagrammatically in Fig.2.3. In the special case of when  $N = 0$  the degeneracy is not lifted and there is only hyperfine manifold in  $G = 1$ .

Now that we have simple Hamiltonians to describe the energy level structure, what are the actual constants? Thankfully lots of spectroscopy has been done on YO as stated previously. The spectroscopic parameters for the  $X^2\Sigma^+$  ground state and the  $A^2\Pi_{1/2,3/2}$  states are given in [6] (Table. 4). For the  $B^2\Sigma^+$  and  $A'^2\Delta_{3/2,5/2}$  states the constants can be found in [43] (Table. 3), and

YO $^2\Sigma$ Hyperfine Splitting				
	$\mathbf{G}' = 1,$ $\mathbf{F}' = \mathbf{N} + 1$	$\mathbf{G}' = 1,$ $\mathbf{F}' = \mathbf{N}$	$\mathbf{G}' = 0,$ $\mathbf{F}' = \mathbf{N}$	$\mathbf{G}' = 1,$ $\mathbf{F}' = \mathbf{N} - 1$
$\mathbf{G} = 1,$ $\mathbf{F} = \mathbf{N} + 1$	$\frac{\gamma_v N}{2} + \frac{b_{f,v}}{4} - t_v \frac{N}{4N+6}$	0	0	0
$\mathbf{G} = 1,$ $\mathbf{F} = \mathbf{N}$	0	$\frac{\gamma_v}{2} + \frac{b_{f,v}}{4} - \frac{t_v}{2}$	$\frac{\gamma_v}{2} (N(N+1))^{1/2}$	0
$\mathbf{G} = 0,$ $\mathbf{F} = \mathbf{N}$	0	$\frac{\gamma_v}{2} (N(N+1))^{1/2}$	$-\frac{3b_{f,v}}{4}$	0
$\mathbf{G} = 1,$ $\mathbf{F} = \mathbf{N} - 1$	0	0	0	$-\frac{\gamma_v(N+1)}{2} + \frac{b_{f,v}}{4} - t_v \frac{N+1}{4N-2}$

Table 2.3: Effective Hamiltonian diagonal in N for hyperfine splitting for  $^2\Sigma$  states in YO [9] (pg. 748).

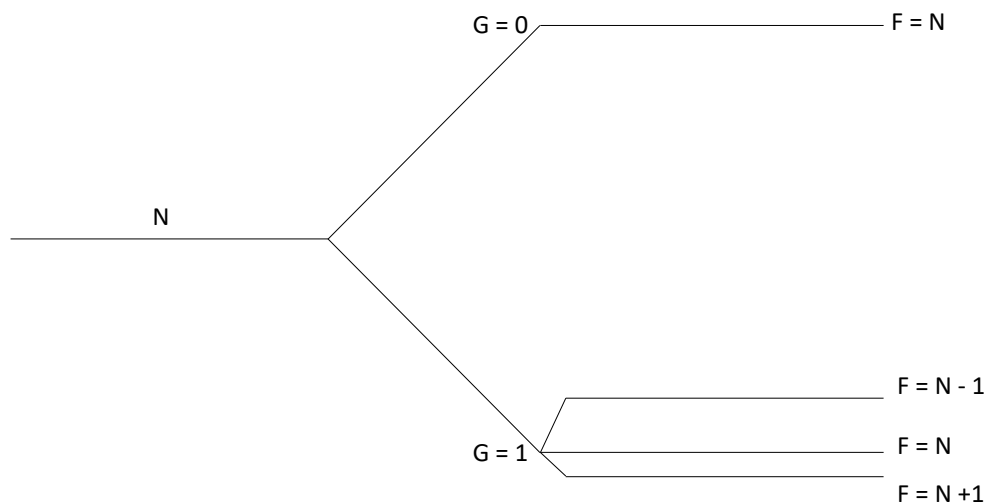


Figure 2.3: Shown qualitatively is the hyperfine splitting of  $^2\Sigma$  states in YO. The triplet states in  $G = 1$  from the coupling of I and S are lifted by the spin-rotation interaction.

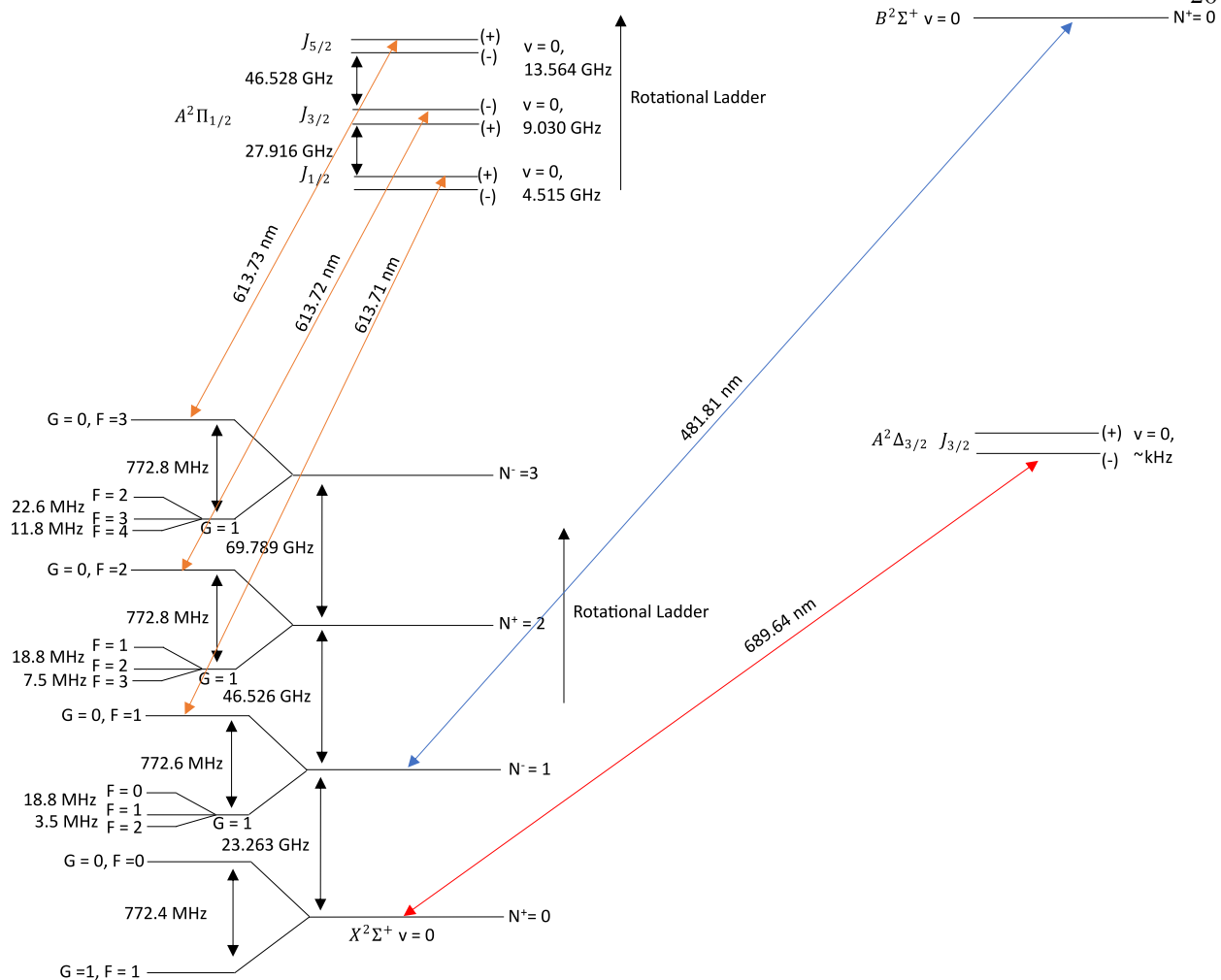


Figure 2.4: Shown qualitatively are the relevant electronic states for laser-cooling YO molecules.

[64] and [65] (Table 4). The hyperfine constants for the ground state can be found in [17] (Table. 2).

So what does the level structure of YO look like? Using the spectroscopy in the above references and Eq.2.8 and 2.9 we can construct a basic energy level structure shown in Fig.2.4. In the bottom is the ground state of YO where the  $v = 0, X^2\Sigma^+$  state is shown with the first four rotational states and the hyperfine splitting in each state. We see the rotational constant is  $B = 2h\pi \times 23.263$  GHz, and the hyperfine splitting between the  $G = 0$  and  $G = 1$  manifolds is roughly 772.5 MHz which is unique to current laser-cooled molecules. Above is the  $v = 0, A^2\Pi_{1/2}$

state with the first three states of the rotational ladder shown. We see that each angular momentum state is comprised of two different manifolds with opposite parity from  $\Lambda$  doubling as previously discussed, with a splitting that goes roughly  $(J + 1/2) \times 4.5$  GHz. Here we neglect the hyperfine splitting in the excited states as it will be discussed later.

An advantage of using Eq.2.8 and 2.9 is you can simply subtract the two equations between two particular states to get the transition energies. Shown are three such transition wavelengths between  $v = 0, X^2\Sigma^+ \rightarrow v = 0, A^2\Pi_{1/2}$ , each climbing up the rotational ladder. Fortunately, transitions that climb up the ladder only differ in frequency by  $\approx 10$  GHz which is a fact we will take advantage of when discussing the geometric branching ratios. The other two states of interest are the  $v = 0, A^2\Delta_{3/2}$  state and the  $v = 0, B^2\Sigma^+$  shown on the right side of the figure. Something of interest is the delta state is lower in energy than the  $v = 0, A^2\Pi_{1/2}$  state which immediately sets alarms for laser-cooling as we will see. Also, of interest is the small parity doublet in the delta state of around a few kHz based on recent data. This also will cause issues for laser-cooling. The  $v = 0, B^2\Sigma^+$  has not been taken advantage of as of yet in the experiment, but I introduce it as it remains a promising candidate for vibrational repumping.

So how do we get the vibrational branching ratios and by extension the Frank-Condon factors? We can use a method based on the WKB approximation called the RKR (Rydberg-Klein-Rees) method [9] (pg.280). This methodology works by inverting the experimental data and using Eq.2.8 and 2.9 which provide quantization of the energy levels to create potential energy curves. These quantized energy levels are subject to a strict phase relation that allows for the determination of the classical turning points for any given energy. Therefore the vibrational potential can be determined. Such a potential is shown in Fig.2.5 which has been calculated by this author using the RKR method, and represents the vibrational potential of the  $X^2\Sigma^+$  ground state. Every third vibrational level has been labeled just for legibility.

With the knowledge of the vibrational potential functions, we can determine the vibrational wavefunctions for each electronic state to get the Frank-Condon factors. A curve is generated for each state as similar to what is shown in Fig.2.5. The vibrational potentials for each electronic state

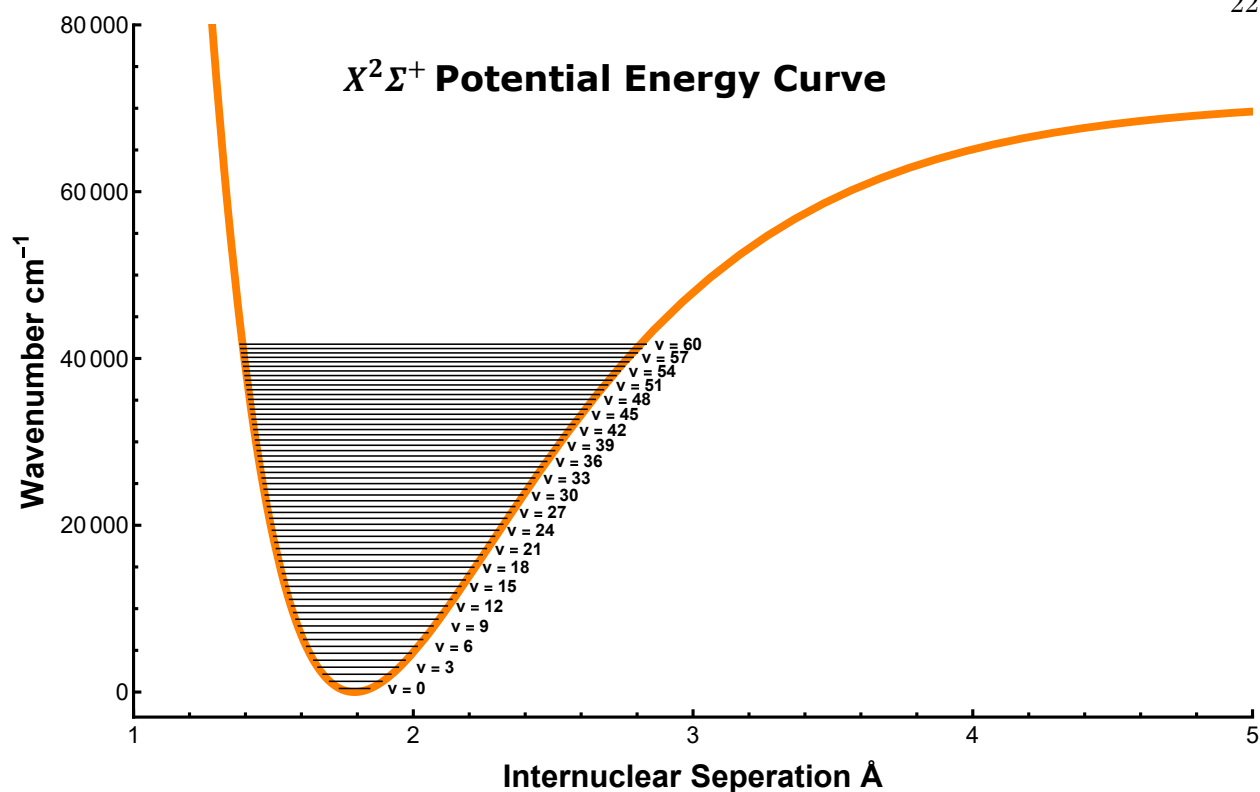


Figure 2.5: Shown is the vibrational potential energy curve of the  $X^2\Sigma^+$  of YO vs internuclear distance calculated by this author using the RKR method. Every third vibrational eigenenergy is shown.

are then plugged into Schrodinger's equation. Numerically diagonalizing Schrodinger's equation gives the vibrational wavefunctions for each state. The wavefunctions for each state of interest are shown in Fig.2.6. One thing that you can immediately notice is that the wavefunctions are all centered around 1.8 angstroms except the  $B^2\Sigma^+$  state and  $A'^2\Delta_{3/2}$  state. From this observation, we can expect a good overlap of the wavefunctions and strong (diagonal) Frank-Condon factors except maybe for the  $B^2\Sigma^+$  state which has the largest deviation of the equilibrium position compared to the other electronic states. We can also see that the spatial extent for the  $v = 0$  wavefunctions is very similar for all electronic states. This also indicates that there should be decent overlap of the wavefunctions.

Now with the wavefunctions, we can calculate the first term in Eq.2.6,  $\int_{\alpha} \psi_v^*(R_{\alpha})\psi'_v(R_{\alpha})dV_{\alpha}$ , to get the vibrational branching ratios between the different electronic states. The Frank-Condon

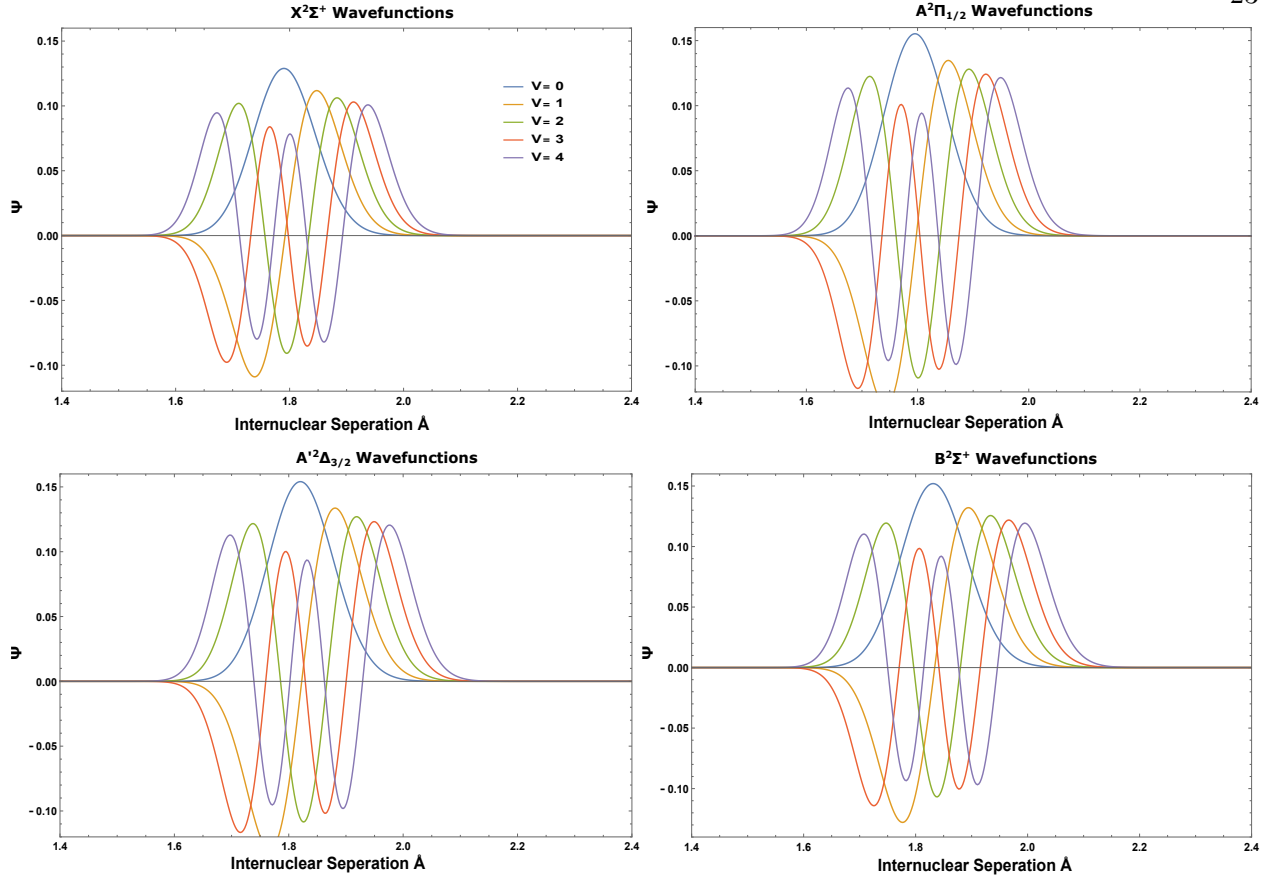


Figure 2.6: Shown are the vibrational wavefunctions  $\Psi$  calculated by this author for the lowest vibrational states in YO for each relevant electronic state. The plots show the wavefunction amplitude vs internuclear distance.

factors which are the square of the branching ratios are given in the tables in Fig.2.7. The Franck-Condon factors are labeled  $q$  and the excited state is given a prime superscript and the lower state has no superscript. Immediately we can see that the vibrational overlap of the  $v = 0, X^2\Sigma^+ \rightarrow v = 0, A^2\Pi_{1/2}$  is very good and any transition between  $v = n, X^2\Sigma^+ \rightarrow v = n, A^2\Pi_{1/2}$  is good meaning the Franck-Condon factors are very diagonal. This has a great consequence in that we can scatter  $1/0.0065 = 150$  photons before decaying to  $v = 1, X^2\Sigma^+$  and  $1/0.0005 = 2000$  photons before decaying to  $v = 2, X^2\Sigma^+$ . As such, we only need two vibrational repump lasers to slow, trap, and cool YO molecules. Additionally, we find that  $v = 0, B^2\Sigma^+ \rightarrow v = 0, X^2\Sigma^+$  transition has good enough branching for repumping purposes. The other two tables involving the  $A'^2\Delta_{3/2}$  are

$q_{v,v}$	$A^2\Pi_{1/2} \rightarrow X^2\Sigma^+$	$q_{v,v}$	$B^2\Sigma^+ \rightarrow X^2\Sigma^+$	$q_{v,v}$	$A^2\Pi_{1/2} \rightarrow A'^2\Delta_{3/2}$	$q_{v,v}$	$A'^2\Delta_{3/2} \rightarrow X^2\Sigma^+$
0,0	0.9930	0,0	0.7536	0,0	0.9078	0,0	0.8539
0,1	0.0065	0,1	0.2093	0,1	0.0858	0,1	0.1340
0,2	0.0005	0,2	0.0330	0,2	0.0060	0,2	0.0114
1,0	0.0069	1,0	0.2140	1,0	0.0895	1,0	0.1352
1,1	0.9773	1,1	0.3751	1,1	0.7425	1,1	0.6018
1,2	0.0143	1,2	0.3099	1,2	0.1505	1,2	0.2290

Figure 2.7: Shown are this author's calculations of the vibrational branching ratios (Frank-Condon factors) between the relevant electronic states in YO.

for reference and will be discussed later. Something that should be noted is that the square of the transition dipole moment is directly proportional to these factors. This means that the transition strengths are suppressed by these factors, and the repump lasers need appreciable power in them to efficiently power broaden the transitions.

As stated before, the property of diagonal Frank-Condon factors is a stringent requirement and greatly limits the number of molecules that can be laser-cooled. This requirement was highlighted in 2004 by Di-Rosa [26] and has been the bane of laser-cooling exotic molecules. However, the number of molecules that have been laser-cooled at the time of this thesis has been growing drastically since the beginning of my time in the lab, and there are a large number of molecules out there that have this property where many have not even been identified yet! However, for this work, we find that YO molecules are definitely amenable to laser-cooling with limited branching. Now with the vibrational branching ratios calculated, we can turn our attention to the geometric factors or the second term in Eq.2.6.

### 2.1.3.2 Geometric/Angular Momentum Branching Ratios

It seems maybe obvious that to laser cool a molecule, it must have limited vibrational branching or diagonal Frank-Condon factors and indeed this is an extremely important aspect of what

$A^2\Pi_{1/2}^-, J = 1/2, \rightarrow X^2\Sigma^+, N = 0^+$						$A^2\Pi_{1/2}^-, J = 1/2 \rightarrow X^2\Sigma^+, N = 2^+$					
		Excited F states						Excited F states			
		F = 0	F = 1	F = 1	F = 1			F = 0	F = 1	F = 1	F = 1
Ground States		mf = 0	mf = -1	mf = 0	mf = 1	Ground States		mf = 0	mf = -1	mf = 0	mf = 1
G = 0, F = 0	mf = 0	0	351/542	351/542	351/542	G = 0, F = 2	mf = -2	0	7/612	0	0
G = 1, F = 1	mf = -1	351/542	351/542	351/542	0	G = 0, F = 2	mf = -1	0	1/175	1/175	0
G = 1, F = 1	mf = 0	351/542	351/542	0	351/542	G = 0, F = 2	mf = 0	0	1/525	7/918	1/525
G = 1, F = 0	mf = 1	351/542	0	351/542	351/542	G = 0, F = 2	mf = 1	0	0	1/175	1/175
$A^2\Pi_{1/2}^+, J = 1/2 \rightarrow X^2\Sigma^+, N = 1^-$						G = 0, F = 2	mf = 2	0	0	0	7/612
						G = 1, F = 1	mf = -1	11/577	1/210	1/210	0
Ground States		mf = 0	mf = -1	mf = 0	mf = 1	G = 1, F = 1	mf = 0	11/577	1/210	0	1/210
						G = 1, F = 1	mf = 1	11/577	0	1/210	1/210
G = 0, F = 1	mf = -1	8/27	1/54	1/54	0	G = 1, F = 2	mf = -2	0	7/408	0	0
G = 0, F = 1	mf = 0	8/27	1/54	0	1/54	G = 1, F = 2	mf = -1	0	7/816	7/816	0
G = 0, F = 1	mf = 1	8/27	0	1/54	1/54	G = 1, F = 2	mf = 0	0	1/350	7/612	1/350
G = 1, F = 0	mf = 0	0	2/9	2/9	2/9	G = 1, F = 2	mf = 1	0	0	7/816	7/816
G = 1, F = 1	mf = -1	1/27	25/108	25/108	0	G = 1, F = 2	mf = 2	0	0	0	7/408
G = 1, F = 1	mf = 0	1/27	25/108	0	25/108	G = 1, F = 3	mf = -3	0	0	0	0
G = 1, F = 1	mf = 1	1/27	0	25/108	25/108	G = 1, F = 3	mf = -2	0	0	0	0
G = 1, F = 2	mf = -2	0	1/6	0	0	G = 1, F = 3	mf = -1	0	0	0	0
G = 1, F = 2	mf = -1	0	1/12	1/12	0	G = 1, F = 3	mf = 0	0	0	0	0
G = 1, F = 2	mf = 0	0	1/36	1/9	1/36	G = 1, F = 3	mf = 1	0	0	0	0
G = 1, F = 2	mf = 1	0	0	1/12	1/12	G = 1, F = 3	mf = 2	0	0	0	0
G = 1, F = 2	mf = 2	0	0	0	1/6	G = 1, F = 3	mf = 3	0	0	0	0

Figure 2.8: Shown are this author's calculations of the rotational branching ratios of the  $A^2\Pi_{1/2}, J = 1/2^\pm \rightarrow X^2\Sigma^+$  states.

molecules can be laser cooled. However, how does one deal with the angular momentum branching? It seems very complicated as if you scatter a photon of an excited electronic state it can have massive branching to a large amount of rotational and hyperfine states. In this section, we will calculate all the angular momentum branching ratios.

So, we are interested in calculating the second term in Eq.2.6  $\langle J, M_J | \mu | J', M_J' \rangle$ . Immediately we can see that these matrix elements are a simplification as the bra and ket are already on the same basis. We know however that different electronic states are represented by different Hund's cases and therefore each electronic state has a set of good quantum numbers. Thankfully these basis transformations are very common and the conversion from Hund's case (b) to Hund's case (a) is the most common. First, we note that the excited state can be written as a linear combination of

$A'^2\Delta_{3/2-}, J = 3/2 \rightarrow X^2\Sigma^+, N = 0^+$									
Ground States		Excited F states							
		F = 1 mf = -1	F = 1 mf = 0	F = 1 mf = 1	F = 2 mf = -2	F = 2 mf = -1	F = 2 mf = 0	F = 2 mf = 1	F = 2 mf = 2
G = 0, F = 0	mf = 0	1/3	1/3	1/3	0	0	0	0	0
G = 1, F = 1	mf = -1	1/12	1/12	0	1/2	1/4	1/12	0	0
G = 1, F = 1	mf = 0	1/12	0	1/12	0	1/4	1/3	1/4	0
G = 1, F = 1	mf = 1	0	1/12	1/12	0	0	1/12	1/4	1/2
$A'^2\Delta_{3/2+}, J = 3/2 \rightarrow X^2\Sigma^+, N = 1^-$									
Ground States		Excited F states							
		F = 1 mf = -1	F = 1 mf = 0	F = 1 mf = 1	F = 2 mf = -2	F = 2 mf = -1	F = 2 mf = 0	F = 2 mf = 1	F = 2 mf = 2
G = 0, F = 1	mf = -1	1/36	1/36	0	49/150	49/300	49/900	0	0
G = 0, F = 1	mf = 0	1/36	0	1/36	0	49/300	49/225	49/300	0
G = 0, F = 1	mf = 1	0	1/36	1/36	0	0	49/900	49/300	49/150
G = 1, F = 0	mf = 0	1/3	1/3	1/3	0	0	0	0	0
G = 1, F = 1	mf = -1	2/9	2/9	0	16/75	8/75	8/225	0	0
G = 1, F = 1	mf = 0	2/9	0	2/9	0	8/75	32/225	8/75	0
G = 1, F = 1	mf = 1	0	2/9	2/9	0	0	8/225	8/75	16/75
G = 1, F = 2	mf = -2	1/25	0	0	6/25	3/25	0	0	0
G = 1, F = 2	mf = -1	1/50	1/50	0	3/25	3/50	9/50	0	0
G = 1, F = 2	mf = 0	1/150	2/75	1/150	0	9/50	0	9/50	0
G = 1, F = 2	mf = 1	0	1/50	1/50	0	0	9/50	3/50	3/25
G = 1, F = 2	mf = 2	0	0	1/25	0	0	0	3/25	6/25

Figure 2.9: Shown are this author's calculations of the rotational branching ratios of the  $A'^2\Delta_{3/2}, J = 3/2^{\pm} \rightarrow X^2\Sigma^+, N = 0^+, 1^-$  states.

$A'^2\Delta_{3/2-}, J = 3/2 \rightarrow X^2\Sigma^+, N = 2^+$									
Ground States		Excited F states							
		F = 1 mf = -1	F = 1 mf = 0	F = 1 mf = 1	F = 2 mf = -2	F = 2 mf = -1	F = 2 mf = 0	F = 2 mf = 1	F = 2 mf = 2
G = 0, F = 2	mf = -2	1/250	0	0	49/375	49/750	0	0	0
G = 0, F = 2	mf = -1	1/500	1/500	0	49/750	18/551	49/500	0	0
G = 0, F = 2	mf = 0	0	1/375	0	0	49/500	0	49/500	0
G = 0, F = 2	mf = 1	0	1/500	1/500	0	0	49/500	18/551	49/750
G = 0, F = 2	mf = 2	0	0	1/250	0	0	0	49/750	49/375
G = 1, F = 1	mf = -1	1/6	1/6	0	1/25	1/50	1/150	0	0
G = 1, F = 1	mf = 0	1/6	0	1/6	0	1/50	2/75	1/50	0
G = 1, F = 1	mf = 1	0	1/6	1/6	0	0	1/150	1/50	1/25
G = 1, F = 2	mf = -2	12/125	0	0	109/958	45/791	0	0	0
G = 1, F = 2	mf = -1	6/125	6/125	0	45/791	19/668	32/375	0	0
G = 1, F = 2	mf = 0	2/125	8/125	2/125	0	32/375	0	32/375	0
G = 1, F = 2	mf = 1	0	6/125	6/125	0	0	32/375	19/668	45/791
G = 1, F = 2	mf = 2	0	0	12/125	0	0	0	45/791	109/958
G = 1, F = 3	mf = -3	0	0	0	1/15	0	0	0	0
G = 1, F = 3	mf = -2	0	0	0	1/45	2/45	0	0	0
G = 1, F = 3	mf = -1	0	0	0	1/225	8/225	2/75	0	0
G = 1, F = 3	mf = 0	0	0	0	0	1/75	1/25	1/75	0
G = 1, F = 3	mf = 1	0	0	0	0	0	2/75	8/225	1/225
G = 1, F = 3	mf = 2	0	0	0	0	0	0	2/45	1/45
G = 1, F = 3	mf = 3	0	0	0	0	0	0	0	1/15

Figure 2.10: Shown are this author's calculations of the rotational branching ratios of the  $A'^2\Delta_{3/2-}, J = 3/2 \rightarrow X^2\Sigma^+, N = 2^+$  state.

$A'^2\Delta_{3/2^+}, J = 3/2 \rightarrow X^2\Sigma^+, N = 3^-$									
Ground States		Excited F states							
		F = 1 mf = -1	F = 1 mf = 0	F = 1 mf = 1	F = 2 mf = -2	F = 2 mf = -1	F = 2 mf = 0	F = 2 mf = 1	F = 2 mf = 2
G = 0, F = 3	mf = -3	0	0	0	1/35	0	0	0	0
G = 0, F = 3	mf = -2	0	0	0	1/105	2/105	0	0	0
G = 0, F = 3	mf = -1	0	0	0	1/525	8/525	2/175	0	0
G = 0, F = 3	mf = 0	0	0	0	0	1/175	3/175	1/175	0
G = 0, F = 3	mf = 1	0	0	0	0	0	2/175	8/525	1/525
G = 1, F = 3	mf = 2	0	0	0	0	0	0	2/105	1/105
G = 1, F = 3	mf = 3	0	0	0	0	0	0	0	1/35
G = 1, F = 2	mf = -2	3/50	0	0	1/225	1/450	0	0	0
G = 1, F = 2	mf = -1	3/100	3/100	0	1/450	1/900	1/300	0	0
G = 1, F = 2	mf = 0	1/100	1/25	1/100	0	1/300	0	1/300	0
G = 1, F = 2	mf = 1	0	3/100	3/100	0	0	1/300	1/900	1/450
G = 1, F = 2	mf = 2	0	0	3/50	0	0	0	1/450	1/225
G = 1, F = 3	mf = -3	0	0	0	4/105	0	0	0	0
G = 1, F = 3	mf = -2	0	0	0	4/315	8/315	0	0	0
G = 1, F = 3	mf = -1	0	0	0	1/394	9/443	8/525	0	0
G = 1, F = 3	mf = 0	0	0	0	0	4/525	4/175	4/525	0
G = 1, F = 3	mf = 1	0	0	0	0	0	8/525	9/443	1/394
G = 1, F = 3	mf = 2	0	0	0	0	0	0	8/315	4/315
G = 1, F = 3	mf = 3	0	0	0	0	0	0	0	4/105
G = 1, F = 4	mf = -4	0	0	0	0	0	0	0	0
G = 1, F = 4	mf = -3	0	0	0	0	0	0	0	0
G = 1, F = 4	mf = -2	0	0	0	0	0	0	0	0
G = 1, F = 4	mf = -1	0	0	0	0	0	0	0	0
G = 1, F = 4	mf = 0	0	0	0	0	0	0	0	0
G = 1, F = 4	mf = 1	0	0	0	0	0	0	0	0
G = 1, F = 4	mf = 2	0	0	0	0	0	0	0	0
G = 1, F = 4	mf = 3	0	0	0	0	0	0	0	0
G = 1, F = 4	mf = 4	0	0	0	0	0	0	0	0

Figure 2.11: Shown are this author's calculations of the rotational branching ratios of the  $A'^2\Delta_{3/2^+}, J = 3/2^+ \rightarrow X^2\Sigma^+, N = 3^-$  state.

different parity-conserving functions as we discussed when talking about lambda doubling [9] (pg. 619). Explicitly the excited states can be written as,

$$|\Lambda; J, |\Omega|; \pm\rangle = \frac{1}{\sqrt{2}}(|\Lambda = 1; S, \Sigma, J, \Omega; M_J\rangle \pm (-1)^{J-S} |\Lambda = -1; S, \Sigma, J, -\Omega; M_J\rangle). \quad (2.11)$$

Again this is the standard basis expansion of the Hund's case (a) state and is called the  $a_\beta$  basis. Now we transform the Hund's case (b) states into the Hund's case (a) basis and the transformation is given in [9] (pg. 230) and is as follows,

$$|\Lambda; N, S, J\rangle = \sum_{\Sigma=-S}^S (-1)^{J-S+\Lambda} (2N+1)^{1/2} \begin{pmatrix} J & S & N \\ \Omega & -\Sigma & -\Lambda \end{pmatrix} |\Lambda; S, \Sigma, J, \Omega\rangle. \quad (2.12)$$

However, as we recall, in YO the Fermi contact interaction is large and we need to perform another basis transformation given by Eq.2.4 to go from the  $b_{\beta S}$  to the  $b_{\beta J}$  basis [9] (pg. 233). After the transformation, to calculate the actual matrix elements it is better to write the dipole operator in tensor notation as we can exploit the Wigner-Eckhart theorem to get all the matrix elements. We recast  $\langle J, M_J | \mu | J', M_J'\rangle$  into  $\langle \Psi_f | T_p^1(d) | \Psi_i \rangle$  where  $T_p^1(d)$  is a rank one spherical tensor operator where  $p = 0, \pm 1$  and denotes the polarization of the driving field. We can then follow the procedures in [9] (sections 5.5.3 - 5.5.5) and with a good summary in [78] we find,

$$\begin{aligned} \langle \Psi_f | T_p^1(d) | \Psi_i \rangle &= (-1)^{F'-M'_f} \begin{pmatrix} F' & I & F \\ -M'_F & p & M_f \end{pmatrix} (-1)^{F+J'+I+1} ((2F'+1)(2F+1))^{1/2} \begin{Bmatrix} J & F & I \\ F' & J' & 1 \end{Bmatrix} \\ &\times \sum_{q=-1}^1 (-1)^{J-\Omega'} ((2J'+1)(2J+1))^{1/2} \begin{pmatrix} J' & 1 & J \\ -\Omega & q & \Omega \end{pmatrix} \langle \Lambda', S', \Sigma' | T_q^1(d) | \Lambda, S, \Sigma \rangle. \quad (2.13) \end{aligned}$$

The last term does not need to be calculated as it is common to all branches and we are looking for the relative branching ratios. Evaluating these terms in Matlab gives us the branching ratios which are summarized in Tables.2.8, 2.9, 2.10, 2.11.

First turning our attention to Fig.2.8 something profound has revealed itself. First, if we were to drive a transition from  $X^2\Sigma^+, N = 0^+, 2^+ \rightarrow A^2\Pi_{1/2}, J = 1/2^-$  we have branching back to the ground state for both  $N = 0$  and  $N = 2$ . However, if we drive  $X^2\Sigma^+, N = 1^- \rightarrow A^2\Pi_{1/2}, J = 1/2^+$  we only have branching back to  $X^2\Sigma^+, N = 1^-$ . There is no branching to  $N = 3$  as that would require two photons! This was pointed out in our group by Ben Stuhl in the important paper [68]. This simple and clever choice of laser-cooling from  $N = 1$  instead of  $N = 0$  to limit rotational branching opened the field and allowed all concurrent work on laser-cooled molecules from all groups. As such, on YO we will laser cool the molecule from  $N = 1$  rotational state and the molecules will spend the majority of their time there unless we optically pump or coherently transfer them to a different rotational state. The other tables show the branching from the  $A'^2\Delta_{3/2}, J = 3/2^\pm \rightarrow X^2\Sigma^+, N = 0^+, 1^-, 2^+, 3^-$  state and unfortunately branching is allowed to the lowest 4 rotational states. As such, if there is any mixing of the parity doublets in the  $A'^2\Delta_{3/2}, J = 3/2^\pm$  massive branching can open up which we will discuss more in the next section.

To summarize the last two subsections to laser cool a molecule pick a molecule with diagonal Frank-Condon factors and laser cool from the  $N = 1$  rotational ground state to limit rotational branching.

#### 2.1.4 The $A'^2\Delta_{3/2}, J = 3/2^\pm$ State

Unique to near ultracold ( $\approx 1\mu\text{K}$ ) laser-cooled molecules YO features a low-lying intermediate  $\Delta$  state. In the previous sections, I mentioned multiple times that we would give further discussion to this state and we will discuss it in detail in this section. This state causes nothing but problems for the laser-cooling of YO molecules but can potentially be used narrowline cooling similar to the methodologies used in alkaline earth atoms.

This state is weakly dipole allowed and gains its transition strength from spin-orbit and Coriolis coupling to the  $^2\Pi$  state. These are the same interactions that are responsible for lifting the degeneracy of lambda doublets in states with non-zero  $\Lambda$ . The lifetime of this state has been measured in our lab to be  $\tau = 23 \mu\text{s}$  corresponding to a linewidth of  $\Gamma = 2\pi \times 6.9 \text{ kHz}$  suspiciously

similar to the linewidth of the  $^3P_1$  transition in strontium atoms and at the nearly the same wavelength at 689.6 nm.

So why is this state a problem? First this state is lower in energy than the  $A^2\Pi$  state and this transition from the  $A^2\Pi$  is strongly allowed as such spontaneous emission of photons can pump molecules into the  $A'^2\Delta_{3/2}, J = 3/2^-$  from  $A^2\Pi_{1/2}, J = 1/2^-$  as we want to perform laser-cooling on this particular  $^2\Pi$  manifold. The transition between these flips parity for an E1 transition. Therefore once you are pumped into the  $A'^2\Delta_{3/2}, J = 3/2^-$  you can only decay back to  $X^2\Sigma^+, N = 0^+, 2^+$  as we calculated in the previous sections with the angular momentum branching ratios in Fig.2.9 and 2.10. It seems we have come to a possible wall as in the previous section we made the claim we want to laser cool from  $X^2\Sigma^+, N = 1^- \rightarrow A^2\Pi_{1/2}, J = 1/2^+$  to prevent branching to other rotational states as this particular transition is closed. However, now we know in YO that the transition is not closed and the branching through the  $A^2\Pi_{1/2}, J = 1/2^+ \rightarrow A'^2\Delta_{3/2}, J = 3/2^- \rightarrow X^2\Sigma^+, N = 0^+, 2^+$  is on the  $3 \times 10^{-4}$  level or it takes roughly 3300 photons which is on the same order as  $v = 0, A^2\Pi_{1/2}, J = 1/2^+ \rightarrow v = 2, X^2\Sigma^+, N = 1^-$  vibrational branching. Additionally, the Frank-Condon factors from the  $A'^2\Delta_{3/2}, J = 3/2^- \rightarrow X^2\Sigma^+, N = 0^+, 2^+$  are poor as we can see from Fig.2.7. Using these Frank-Condon factors we see that we will populate the  $v = 0, 1, 2, X^2\Sigma^+, N = 0^+, 2^+$  states by the time we perform all the slowing, magneto-optical trapping, sub-Doppler cooling and conservative trapping. For a visual reference, these branchings are shown explicitly in Fig.2.12.

We are not done quite yet as there is another issue that the parity doublet in the  $A'^2\Delta_{3/2}, J = 3/2^\pm$  is small on the order of a few kHz and the dipole moment is large at 7.5 D. This means any stray electric fields generated by our in vacuum MOT coils or viewports will mix these parity doublets. To be more concrete the Hamiltonian for the stark shift between parity doublet hyperfine manifolds is [9] (pg. 551),

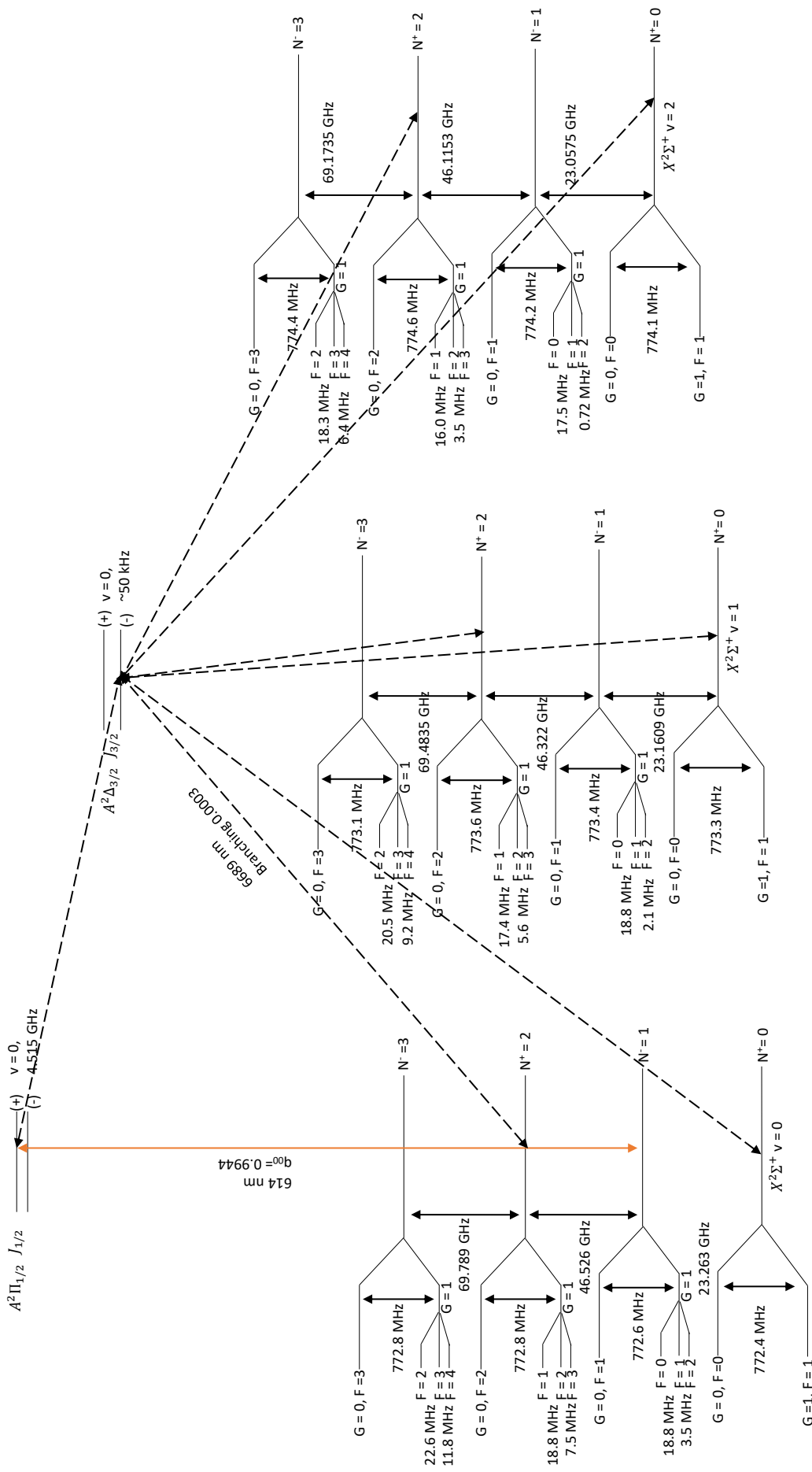


Figure 2.12: Shown is the branching from the  $A^2\Delta_{3/2}, J = 3/2^+ \rightarrow X^2\Sigma^+, N = 0^+, 2^+$  ground states. We see that rotational closure is broken on the order of 3000 photon scatters.

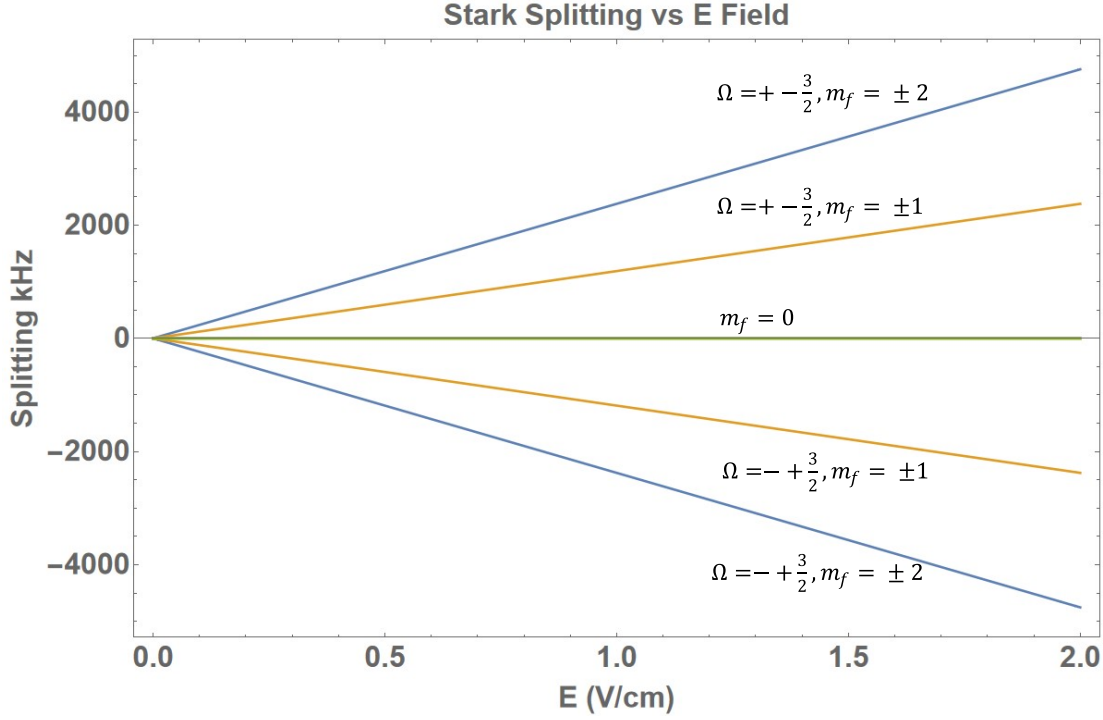


Figure 2.13: Theoretical stark splitting of hyperfine spin states with an applied field in the  $A^2\Delta_{3/2}, J = 3/2^\pm, F = 2$  manifold.

$$\langle J, \Omega, I, F, M_F | -T_{p=0}^1(\mu_e)T_{p=0}^1(E) | J, \Omega, I, F, M_F \rangle = -\frac{\mu_0 E_0 M_F \Omega [J(J+1) + F(F+1) - I(I+1)]}{2F(F+1)J(J+1)} \quad (2.14)$$

Here  $E_0$  is the electric field strength in V/cm. Putting this interaction into a simple  $2 \times 2$  matrix with an energy splitting of 50 kHz and diagonalizing it gives a theoretical curve shown in Fig.2.13. Here we see a strong concern in that small stray fields completely mix the  $A^2\Delta_{3/2}, J = 3/2$  state. To check these calculations we can perform high-resolution stark spectroscopy ourselves. The spectroscopy is shown in Fig.2.14. This spectroscopy is performed by applying an electric field by turning our in-vac MOT coils from parallel to a series configuration with 1 M $\Omega$  resistors on each coil to prevent any B-fields from being generated. The molecules are then released from our blue-detuned MOT and are optically pumped into the  $X^2\Sigma^+, N = 0^+, F = 1$  state. Light at 689.6 nm

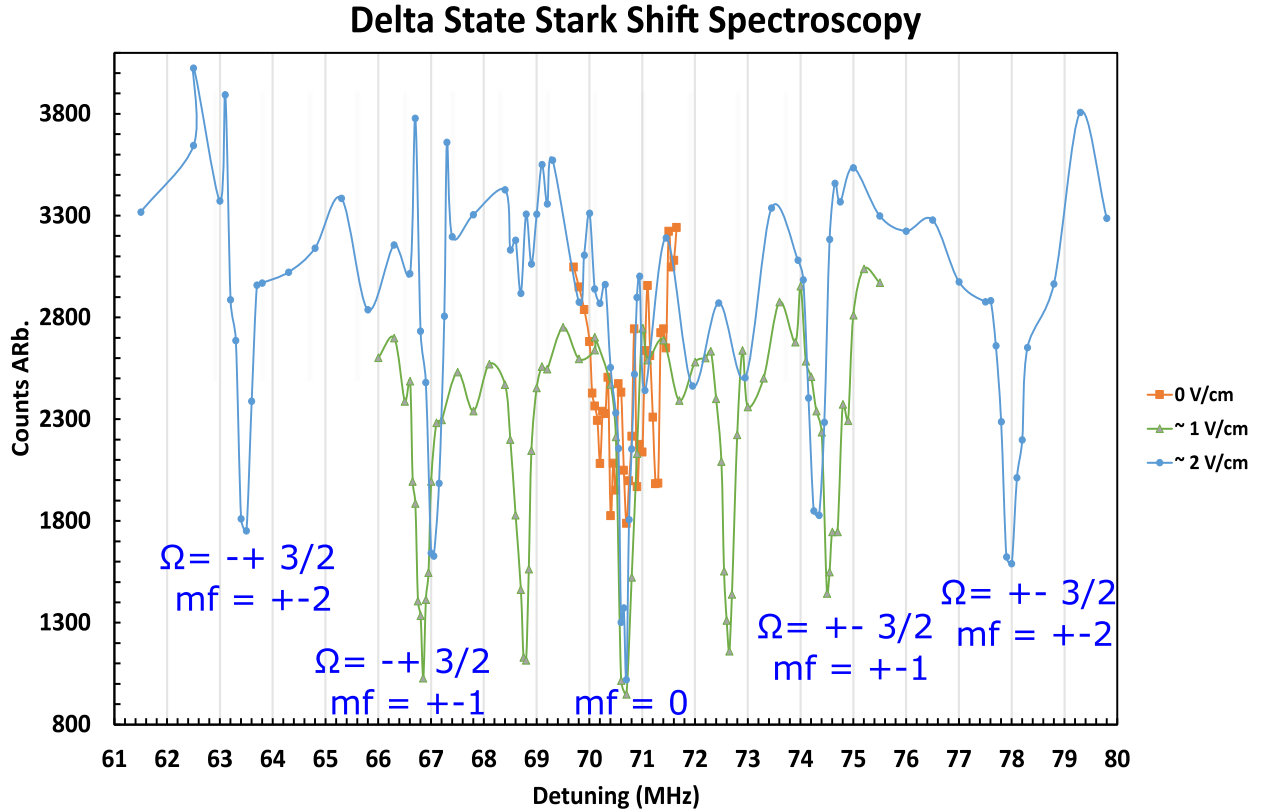


Figure 2.14: Stark splitting of the  $X^2\Sigma^+, N = 0^+, F = 1 \rightarrow A'^2\Delta_{3/2}, J = 3/2^\pm, F = 2$  transition. Shown is depletion spectroscopy with different applied electric fields.

driving the  $X^2\Sigma^+, N = 0^+, F = 1 \rightarrow A'^2\Delta_{3/2}, J = 3/2, F = 2$  is then applied for a few milliseconds and the detuning is stepped. This depletes all the population into the  $X^2\Sigma^+, N = 2^+$  manifold as we expect from the angular momentum branching ratios. The linewidths are limited by Doppler and power broadening to 130 kHz. We find good agreement with the theoretical predictions.

We can see that at zero field there are stray fields present that mix the  $A'^2\Delta_{3/2}, J = 3/2$  state. This is also unwanted as it opens all rotational state branching from the  $A'^2\Delta_{3/2}, J = 3/2$  specifically  $A'^2\Delta_{3/2}, J = 3/2^\pm \rightarrow X^2\Sigma^+, N = 0^+, 1^-, 2^+, 3^-$  with no applied field. This can be visualized using Fig.2.12 except there is now branching to all the odd rotational states as well. It seems that YO maybe is not a great candidate for laser-cooling as the rotational branching seems like a technical nightmare to implement all the rotational and vibrational repumps to keep photons

scattering on the  $X^2\Sigma^+, N = 1^- \rightarrow A^2\Pi_{1/2}, J = 1/2^+$  transition. I am happy to say that we do indeed apply all these repumps in the experiment using a combination of many lasers and microwave mixing of many different rotational states. This was an important part of the middle part of my dissertation work. We will see that is most certainly worth cooling YO molecules even if the upfront cost to do so is very technically challenging as the sub-Doppler cooling in YO is extremely robust and reaches the lowest temperatures by any laser-cooled molecular species, especially in the presence of optical conservative trapping light.

## 2.2 Rotational Transitions

Rotational transitions occur at 10's of GHz for YO molecules and form an important tool for both coherent manipulation for state transfer and mixing of different rotational states to effectively optically repump many rotational manifolds with a single laser. We will only discuss rotational transitions in the ground state. Therefore the angular momentum coupling is given by Hund's case (b) Fig.2.2. The Hamiltonian for rotational transitions in Hund's case (b) basis is given in [9] (pg. 266) as,

$$\begin{aligned} \langle N', \Lambda', S, J', M'_J | -T_{p=0}^1(\mu_e)T_{p=0}^1(E) | N, \Lambda, S, J, M_J \rangle = \\ E_0(t)\mu_0(-1)^{J'+J+N'+S'-M'_J} \begin{pmatrix} J' & 1 & J \\ -M'_J & 0 & M_J \end{pmatrix} ((2J+1)(2J'+1))^{1/2} \begin{Bmatrix} J' & N' & S \\ N & J & 1 \end{Bmatrix} \\ \times (-1)^{N'-\Lambda'} \begin{pmatrix} N' & 1 & N \\ -\Lambda' & 0 & \Lambda' \end{pmatrix} ((2N'+1)(2N+1))^{1/2}. \quad (2.15) \end{aligned}$$

First, the two 3J matrices constrain the transition to follow  $N' = N \pm 1$  and the standard selection rule for E1 transitions  $\Delta J = 0, \pm 1$ . Further, since YO has a unique Hund's case (b) coupling from the large Fermi contact interaction, using Eq.2.4 there is an additional selection rule that  $\Delta G = 0$  as a transition that changes G is a spin flip and is a M1 transition. However, I will mention that these M1 transitions may become of use in the future with a new microwave design for

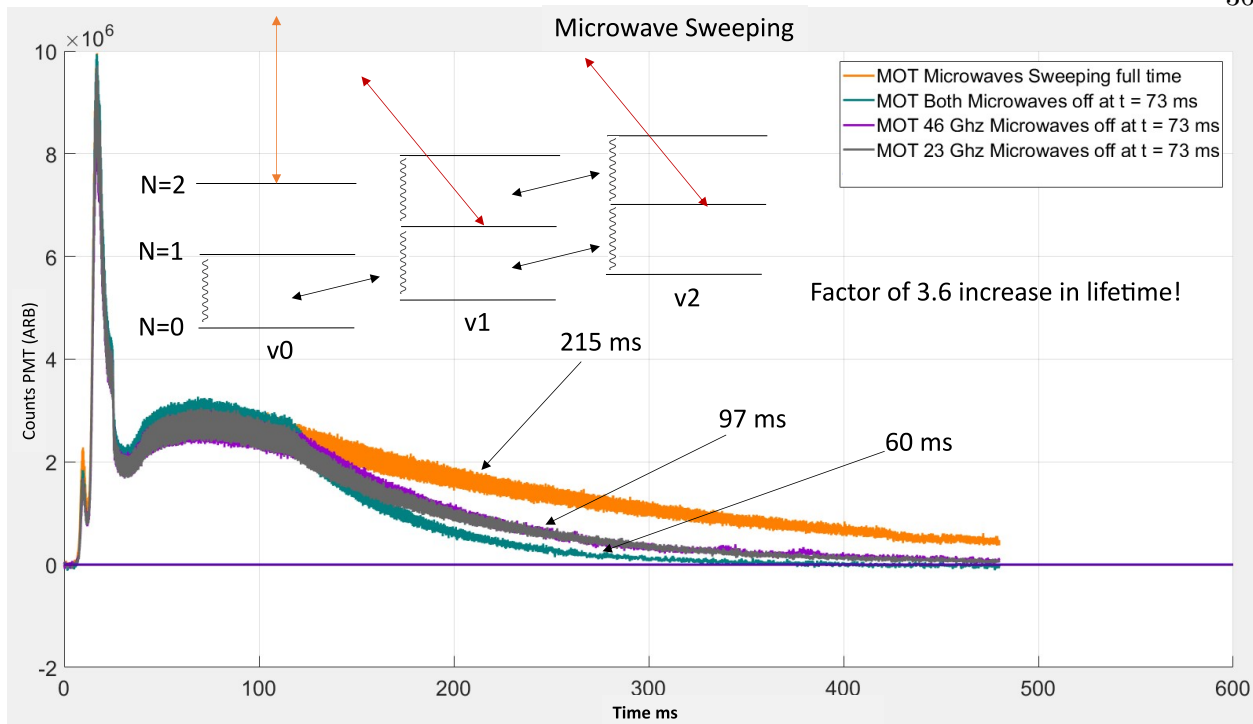


Figure 2.15: Shown is the application of microwave sweeping to repump the  $X^2\Sigma^+$ ,  $N = 0^+, 1^-, 2^+$  states during the Dual Frequency MOT which will be discussed in chapter 4. Fluorescence of the MOT is readout vs time with a PMT. Microwaves are swept at 40 kHz across the vibrational manifolds on both  $N = 0 \rightarrow N = 1$  and  $N = 1 \rightarrow N = 2$ . We can see with the application of sweeping microwaves that the lifetime in the MOT increases by a factor of 3.6. Note the legend is offset from the trace by exactly 40 ms, this is just an experimental artifact from the timing setup.

microwave shielding of inelastic collisions. They would allow efficient single-spin state transfer to specific spin manifolds between  $N = 1$  and  $N = 0$  with less optical pumping. The exact transition frequencies from  $N = 0 \rightarrow N = 1$  are given in [69] to the kHz level. For transitions between  $N = 1 \rightarrow N = 2$  the splittings are calculated and shown in Fig.2.12.

Since we have large rotational branching from the  $^2\Delta$  state can you mix all the population over several rotational manifolds while applying a couple of lasers to repump the vibrational branching? The answer is yes, shown in Fig.2.15 is the application of different microwave sweeps during the dual-frequency MOT which will be discussed in Chapter 4. Microwaves are swept at 40 kHz with a triangle waveform across the vibrational manifolds on both  $N = 0 \rightarrow N = 1$  and  $N = 1 \rightarrow N = 2$ . Lasers are applied on  $N = 1$  to repump the vibrational population buildup back into  $v = 0$ .

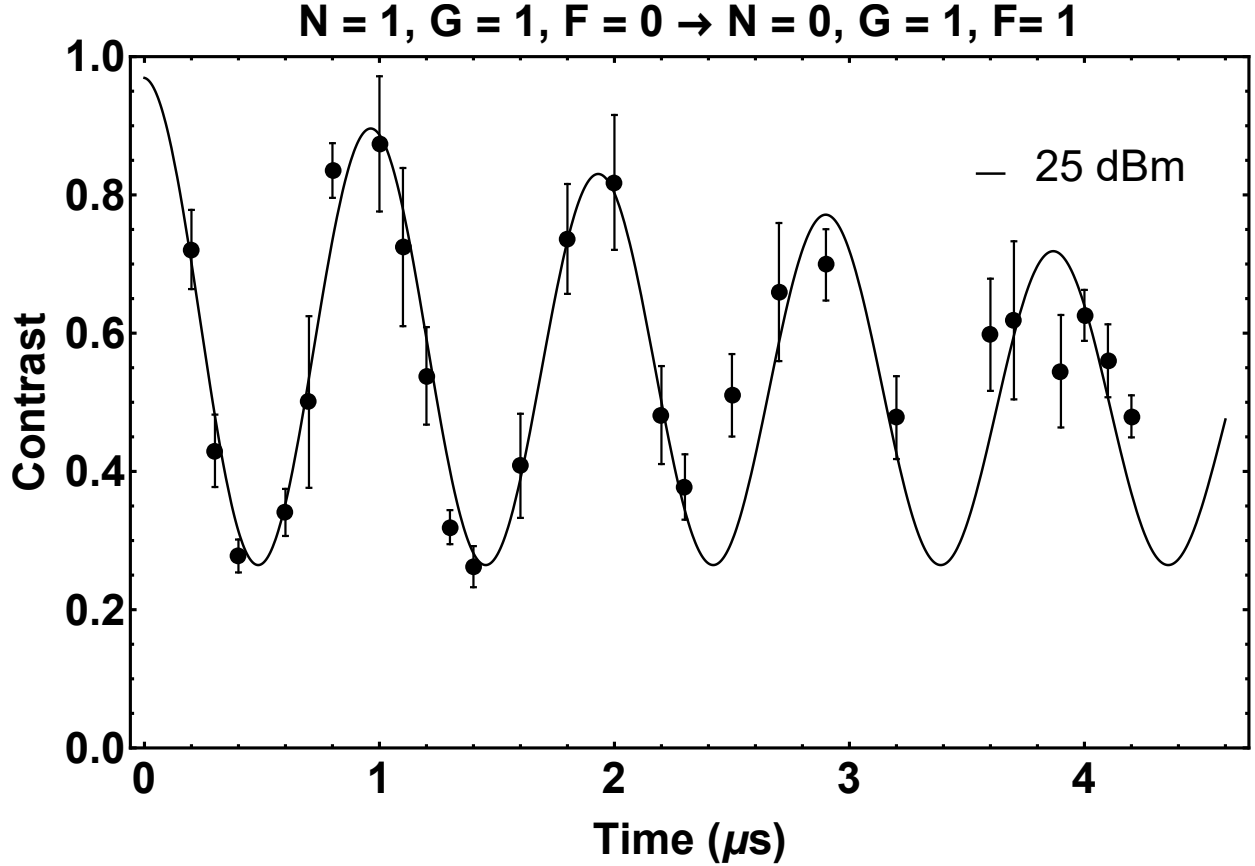


Figure 2.16: Shown is Rabi oscillations between  $X^2\Sigma^+, N = 1^-, G = 1, F = 0 \rightarrow X^2\Sigma^+, N = 0^+, G = 1, F = 1$ . Rabi rates of around 1 MHz are achieved. The contrast is limited by the decoherence rate of around  $8.8 \mu\text{s}$  due to inhomogeneous microwave fields in our metal vacuum chamber. The output power of the microwave horn was 25 dBm.

On  $v = 0$  instead of microwaves mixing  $N = 1 \rightarrow N = 2$  another laser is applied driving the  $X^2\Sigma^+, N = 2^+, \rightarrow A^2\Pi_{1/2}, J = 3/2^-, F = 2$  transition. This optically pumps the population into  $X^2\Sigma^+, N = 0^+$  which is mixed back into  $N = 1$  with microwaves on  $N = 0 \rightarrow N = 1$ . We can see with the application of sweeping microwaves that the lifetime in the MOT increases by a factor of 3.6. This was a fortunate discovery as the increase in MOT lifetimes allowed the advent of the blue-detuned MOT which has a small spring constant and therefore a slow compression speed as will be discussed later.

Beyond just mixing the population we can coherently drive different rotational states for

single spin state preparation of the molecules. Shown in Fig.2.16 between  $X^2\Sigma^+, N = 1^-, G = 1, F = 0 \rightarrow X^2\Sigma^+, N = 0^+, G = 1, F = 1$  we can achieve appreciably fast Rabi rates of around 1 MHz which allow Landau-Zener sweeps on the order of  $\approx 10 \mu\text{s}$ . With our new microwave shielding setup we hope to achieve Rabi frequencies on the order of 30 MHz.

### 2.3 Vibrational Transitions

This section will briefly discuss vibrational transitions as they set a fundamental limit of the experimental run time. The transition dipole moment of a vibrational transition can be written as [9] (pg. 267),

$$\mu_e(v', v) = \mu_0 + \left(\frac{d\mu_e}{dR}\right)_0 \langle v' | q | v \pm 1 \rangle + \frac{1}{2} \left(\frac{d^2\mu_e}{d^2R}\right)_0 \langle v' | q | v, v \pm 2 \rangle + \dots \quad (2.16)$$

Here a harmonic approximation has been used to Taylor expand around the internuclear equilibrium position of the vibrational potentials instead of using the full solution of the wavefunctions as was done earlier in Fig.2.6. The subscript 0 means we are evaluating these derivatives at the equilibrium position. As such to drive a transition between  $v \rightarrow v + 1$  the moment is proportional to the derivative of the dipole moment. Since we know the energy spacing of the vibrational levels extremely well from previous spectroscopy Eq.2.8. We can write the transition dipole moment as,

$$\mu_e(v + 1, v) = \left(\frac{v + 1}{2}\right)^{1/2} \left(\frac{\hbar}{m\omega_e}\right)^{1/2} \left(\frac{d\mu_e}{dR}\right)_0. \quad (2.17)$$

Here  $\omega_e$  is the energy spacing of the vibrational levels in the  $X^2\Sigma$  in YO which has a wavelength of  $11.6 \mu\text{m}$ . The reason we are discussing this is that Black-Body-Radiation (BBR) can drive vibrational transitions at room temperatures at an appreciable rate. This sets the fundamental limit of the lifetime of the experiment especially if you are doing coherent quantum gas studies. The excitation rate from BBR is [76],

$$\Gamma_i^{BBRabs} = \frac{8\pi^2}{3\epsilon_0\hbar c^3} \sum_f \frac{\nu_{fi}^3 \mu_{fi}^2}{e^{h\nu_{fi}/k_b T} - 1}. \quad (2.18)$$

The summation is over all states accessible from the initial state  $i$ . If we plug in all the numbers at room temperature we get a lifetime of 5.4 s. If we put the molecules in an environment at 100 K by surrounding the molecules with a cryo shield the lifetime increases to over 20,000 s. In the future when evaporative cooling is applied the time left to perform fundamental studies of a degenerate gas of YO molecules will be very limited. In that case, some form of BBR shielding will be required held at lower than room temperatures.

## 2.4 Zeeman Splitting

This section will discuss Zeeman splitting of both the  $X^2\Sigma^+, N = 0^+, N = 1^-$  and  $A^2\Pi_{1/2}, J = 1/2^\pm$  states. Understanding the Zeeman structure of both these states is crucial for magneto-optical trapping, coherent state transfer of the molecules, and sub-Doppler cooling. The relative differential shifts are also important for the blue-detuned MOT and sub-Doppler cooling between different G manifolds in the ground state.

### 2.4.1 Zeeman Splitting of $X^2\Sigma^+, N = 0^+, N = 1^-$

Due to various angular momenta in molecules, there are many magnetic moments to consider when we discuss the interaction of a particular electronic state with an applied magnetic field. However, for YO it is an open shell molecule meaning we have a strong  $1 \mu_B$  in the ground state from the electron spin. It turns out all other magnetic couplings are proportional to the nuclear Bohr-magneton  $\mu_N$ . This means all other magnetic coupling will be suppressed in strength by the electron to proton mass ratio  $\frac{m_e}{m_p}$  and their interactions in the fields we apply on this experiment will be on the kHz level. Therefore we will only consider the contribution to the magnetic moment from the electron spin solely.

The interaction with an applied B-Field in the  $X^2\Sigma^+$  can easily be written out using [9] (section 5.5.4) and Eq.2.4 with a good summary also found in [83]. We find that the Hamiltonian governing the Zeeman interaction is,

$$\begin{aligned}
H_Z^{Zeeman} = & \langle ((I, S)G, N), F | g_s \mu_B B_Z T_0^1(S) | ((I, S)G', N), F' \rangle = \\
& g_s \mu_B B_Z (-1)^{F-m_f} ((2G' + 1)(2G + 1)(2F' + 1)(2F + 1)(2S + 1)(S(S + 1))^{1/2} \begin{pmatrix} F & 1 & F' \\ -m_F & 0 & m'_f \end{pmatrix} \\
& \times (-1)^{F+N+1+G} \begin{Bmatrix} G' & F' & N \\ F & G & 1 \end{Bmatrix} (-1)^{G+I+1+S} \begin{Bmatrix} S & G' & I \\ G & S & 1 \end{Bmatrix}. \quad (2.19)
\end{aligned}$$

With the Zeeman interaction, we can also add the Hamiltonian in table Table.2.3 to see the splitting in the full energy landscape. We then obtain the splittings for  $X^2\Sigma^+, N = 1^-$  and  $X^2\Sigma^+, N = 0^+$  shown in Fig.2.17 and Fig.2.18. Qualitatively we can observe a couple properties of the Zeeman interaction. First, for the  $G = 0$  manifolds, the interaction is relatively weak and flat at low fields  $> 10$  Gauss as expected for the spin singlet. However, as the field strength increases the coupling of  $G = I + S$  begins to break down and the interaction becomes that of independent electronic spins transitioning into the Paschen-Bach regime at even higher fields. We see similar behavior in the  $G = 1$  manifolds, but the interaction energies are much more significant as they are the magnetically sensitive triplet states. In either case, we see the shift is only approximately linear up to around  $\approx 5$  Gauss and then roughly linear again in fields of around  $\approx 25 - 50$  Gauss.

#### 2.4.2 Zeeman Splitting of $A^2\Pi_{1/2}, J = 1/2^\pm$

In the excited state, the standard Hund's case (a) basis Fig.2.2 gives good quantum numbers. The Zeeman interaction can be written in a simple form [72],

$$H_Z^{Zeeman} = \mu_B B_Z \frac{g_I \Lambda + g_S \Sigma}{J(J + 1)} \Omega M_F. \quad (2.20)$$

You can make an immediate observation about the magnetic interaction in the  $A^2\Pi_{1/2}, J = 1/2^\pm$  state. The observation is that the projection of the orbital angular momentum along the internuclear axis  $\Lambda$  and the projection of the electronic spin along the internuclear axis  $\Sigma$  are in opposite directions. Additionally, the interaction is weighted by the factor of  $J(J + 1)$ . As such, we

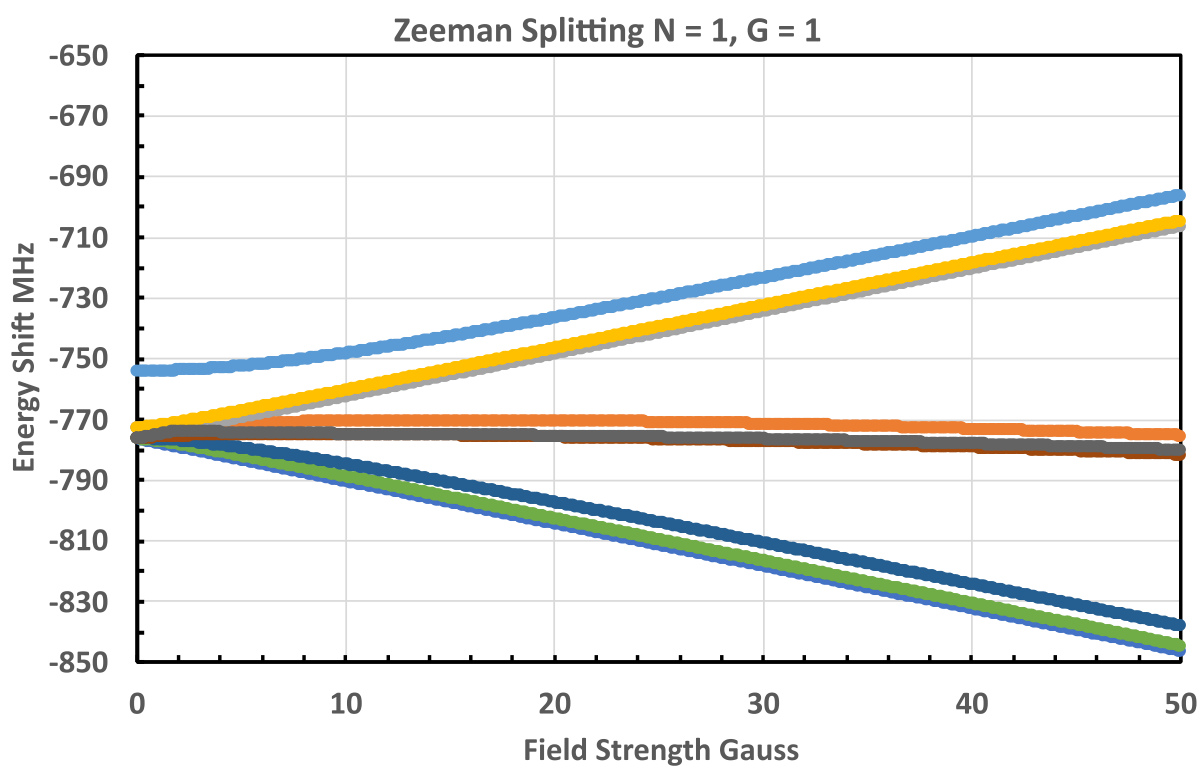
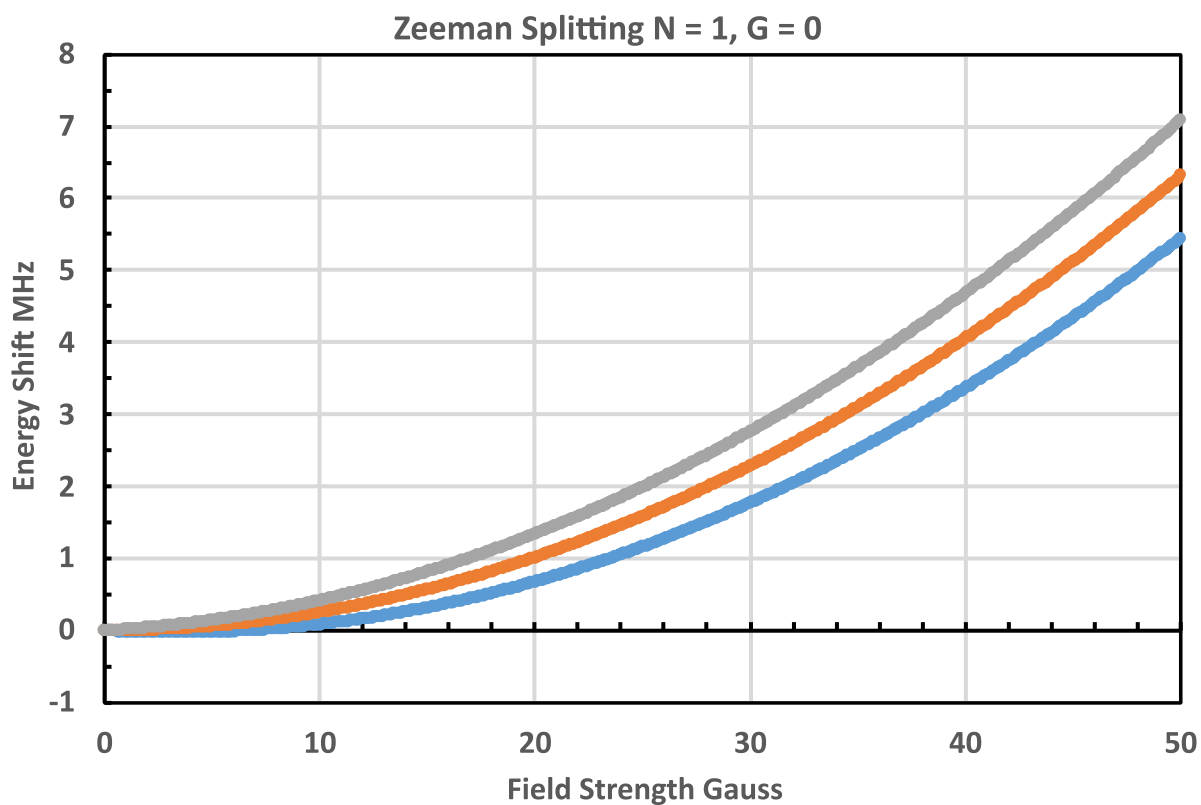


Figure 2.17: Zeeman splittings of the  $X^2\Sigma^+, N = 1^-$  states.

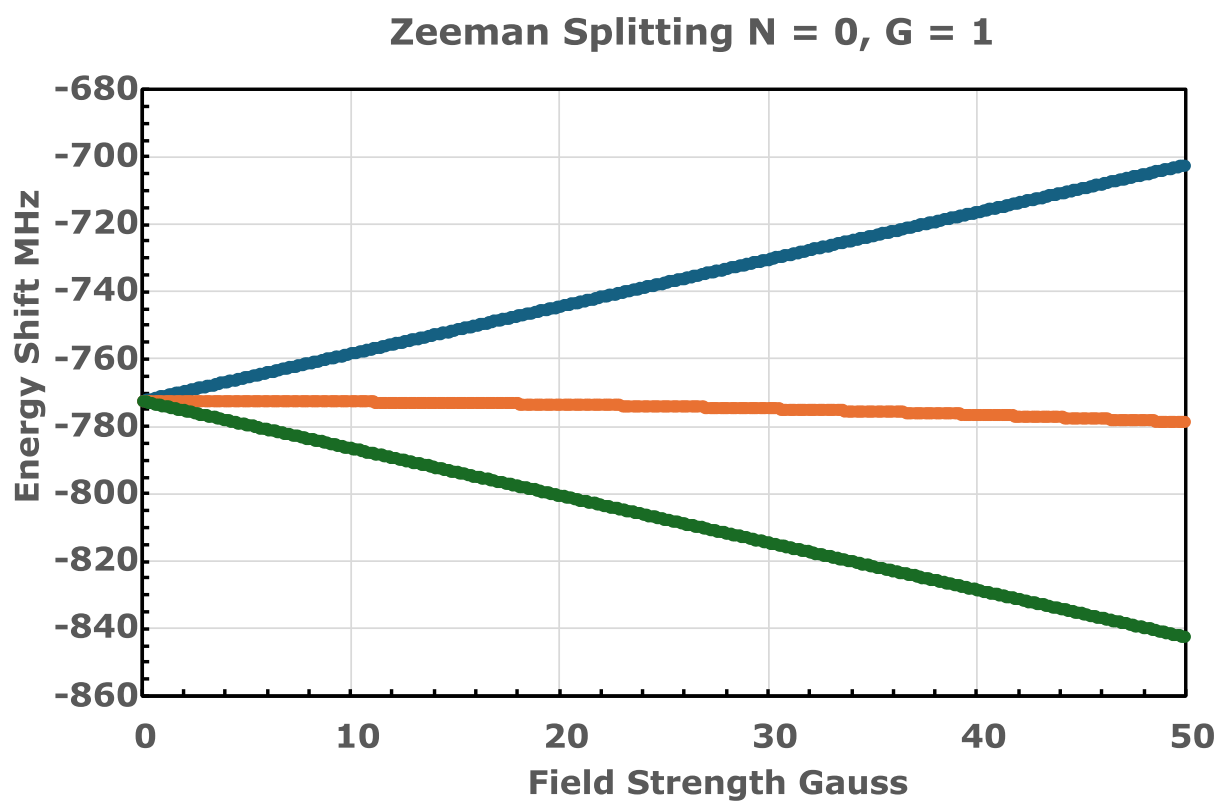
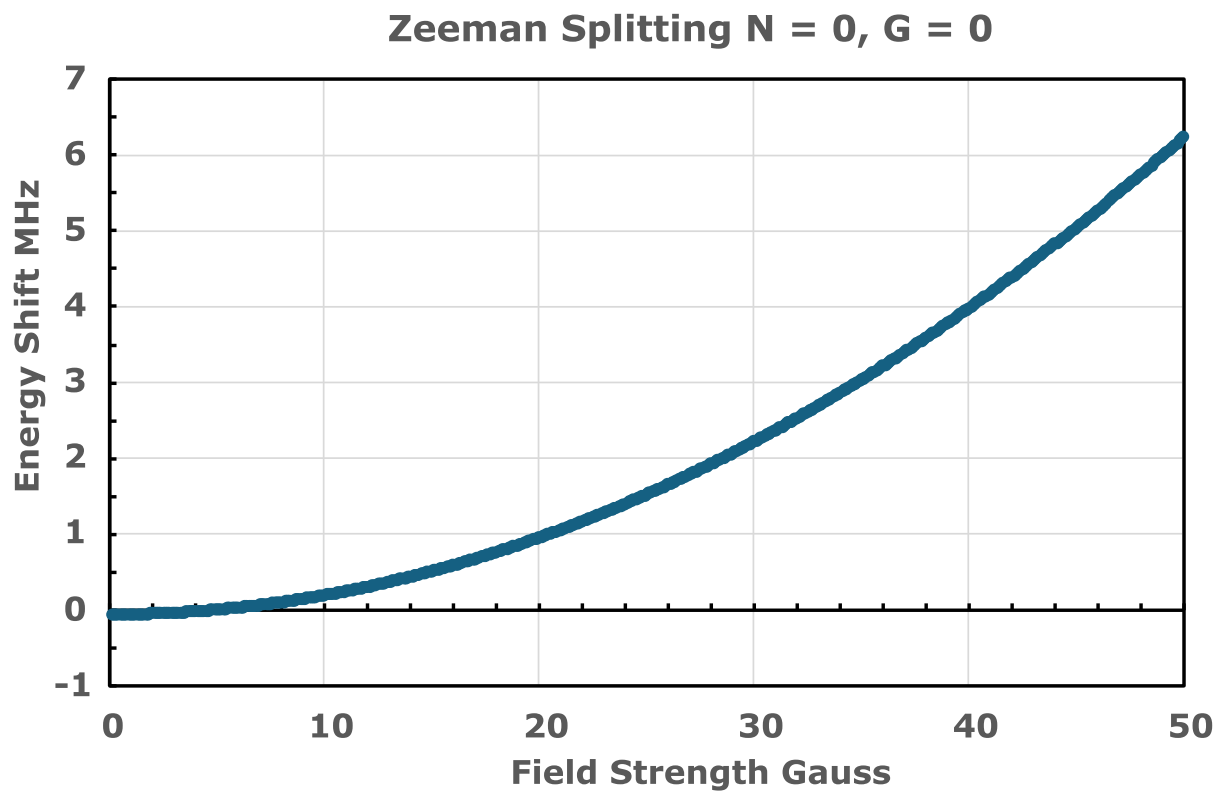


Figure 2.18: Zeeman splittings of the  $X^2\Sigma^+, N = 0^+$  states.

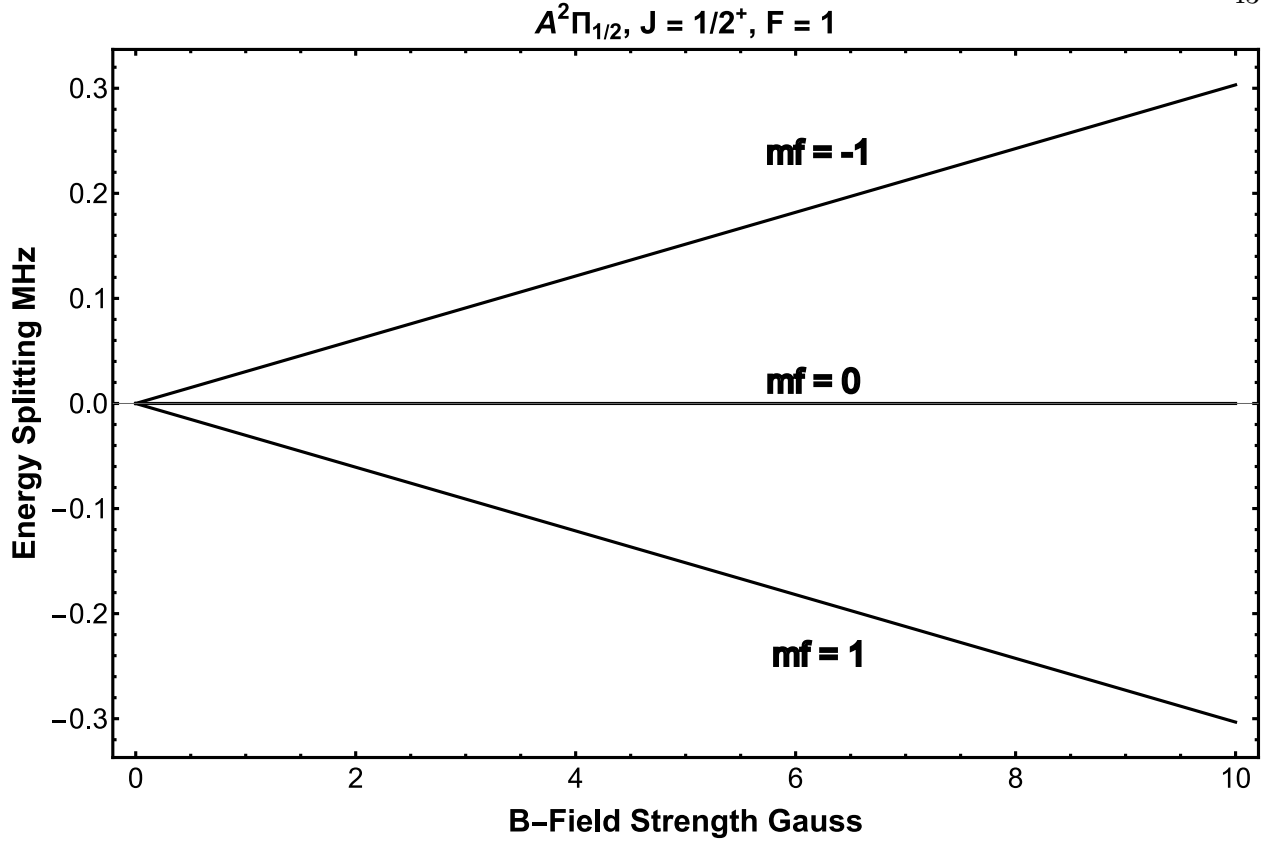


Figure 2.19: Zeeman splitting of the  $A^2\Pi_{1/2}, J = 1/2^+, F = 1$  state.

expect the g-factor to be essentially zero and the only other interactions are nuclear interactions and again are suppressed by the electron to proton mass ratio  $\frac{m_e}{m_p}$ .

However, in reality, the coupling is more complicated than the simple expression in Eq.2.20 as mixing with the nearby  $B^2\Sigma^+$  state introduces additional terms into the Zeeman interaction resulting in the intimidating Hamiltonian given in [9] eq. 9.71 (pg. 621). If we plug in the relevant quantum numbers  $\Omega = 1/2$ ,  $J = 1/2$ ,  $\Sigma = -1/2$ ,  $\Lambda = 1$ , and  $F = 1$  to that Hamiltonian we get a simple linear expression [72],

$$H_Z^{Zeeman} = \pm \frac{1}{3}(g'_l - g'_r)\mu_B B_Z M_F. \quad (2.21)$$

The constants  $g'_l$  and  $g'_r$  are related to the lambda doubling coefficients  $p$  and  $q$  that we discussed earlier in Eq.2.8 by the expressions  $g'_l = \frac{p}{2B}$  and  $g'_r = \frac{-q}{B}$  where B is the rotational

constant in the  $A^2\Pi_{1/2}$  state. The  $\pm$  in front of the expression denotes the parity state. Evaluating these relations gives us an effective small g-factor of -0.065 which is very small but non-zero and allows efficient DC magneto-optical trapping of YO molecules. The splitting is shown in Fig.2.19. Additionally, there exist two Hyperfine manifolds in  $A^2\Pi_{1/2}$   $F = 0$  and  $F = 1$ . Only the splitting of  $F = 1$  is shown in Fig.2.19  $F = 0$ ,  $m_f = 0$  has no linear splitting at low field. These two states  $F = 0$ ,  $F = 1$  are unresolved within the linewidth of the transition.

## Chapter 3

### Laser-cooling of YO Molecules

There are two forces associated with the interaction of light with the molecules. The one that will be at the forefront of this section is the scattering force and later the dipole force. We will delve into the specifics of laser-cooling molecules and discuss Doppler and sub-Doppler cooling.

#### 3.1 Type-I vs. Type-II Transitions

If you have been trying to study or learn about the laser-cooling of molecules, you have undoubtedly encountered discussions of type-I vs. type-II transitions all over the place [68]. While these discussions may seem technical, they provide a deep physical understanding of the resultant laser-cooling of molecules. It was not until very recently that full understanding of the sub-Doppler dynamics of Type-II transitions have been understood mostly through the work of Mike Tarbutt even though they were predicted in the mid to late 90s. The reason for this is that most atomic MOTs work on Type-I transitions and they worked well so interest in different MOTs and sub-Doppler cooling mechanisms was just left on the shelf for 20 years. Only through the advent of laser-cooling molecules has the community found renewed interest in the subjects of laser-cooling and MOTs arising partly to address the complexity of molecular structure.

So what is the difference between a type-I and type-II transition? By definition a type-I is a transition that drives transitions with total angular momentum  $J \rightarrow J + 1$ , conversely, a type-II transition is one that drives  $J, J + 1 \rightarrow J$ . Note that the quantum number does not need to be  $J$  it can also be  $F$  or  $L$  or any other quanta for your given system as long as the difference in the

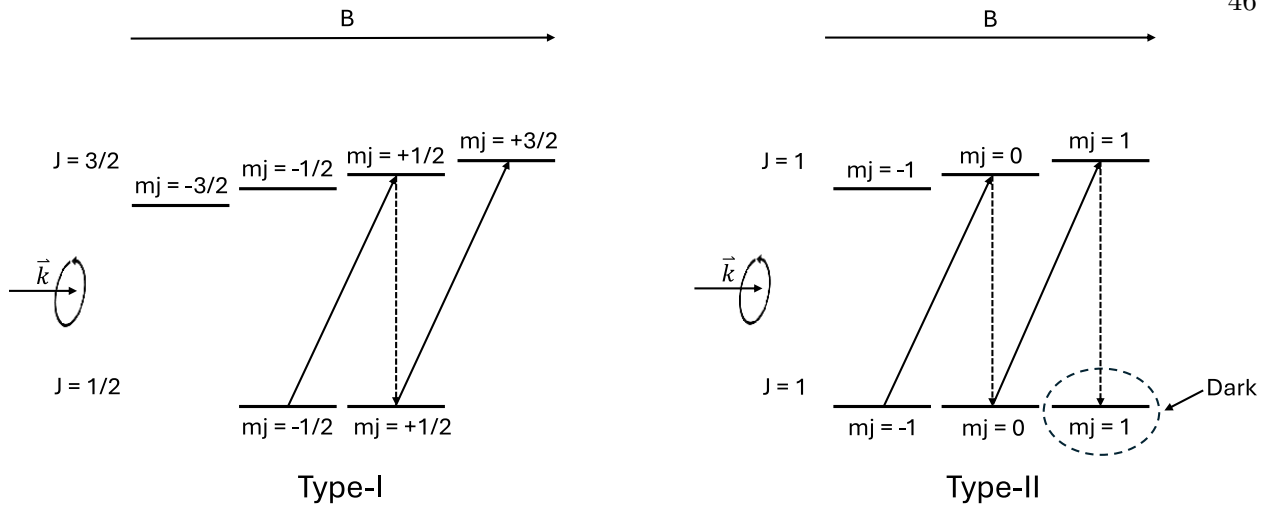


Figure 3.1: Type-I vs type-II transitions are shown. For any given polarization there is a single state or linear combination of states that is dark to the light field in type-II transitions.

angular momentum follows the above rules.

To provide more insight into these two different transitions two examples are shown in Fig.3.1. The first case is possibly the most simple case you could imagine in an atomic system that has a ground magnetic structure. In this case, it would correspond maybe to elements in the first column of the periodic table with no nuclear spin driving a transition with angular momenta of  $J = 1/2 \rightarrow J = 3/2$  corresponding to a type-I transition. Here we have applied a magnetic field to define a quantization axis and are going to drive  $\sigma^+$  transitions. We assume the ground state is not magnetically sensitive for clarity. In reality, there would be a differential Zeeman shift between the ground state and excited state, but it is not important for this analysis.

We see that applying the light optical pumps the population to the opposite stretched state driving the  $J = 1/2, m_j = 1/2 \rightarrow J = 3/2, m_j = 3/2$  transition. If you adjust the magnetic field strength you can tune the transition energy to maybe compensate for the Doppler shift which is the basis for Zeeman slower used in cold atomic experiments. You can also apply a gradient field to get a position-dependent force for magneto-optical trapping.

Now let us check the type-II case where driving a transition  $J = 1 \rightarrow J = 1$  is shown. In this case, we have an immediate problem in that if we apply the light we will optically pump ourselves

into the  $J = 1, m_J = 1$  state. This state is dark to the incoming polarization. However, it is not just this special case where you have a dark state. For any polarization combination, there is a state or linear combination of states that are dark to the light field (no transition dipole moment). This is a major problem in that if we want to do Doppler cooling or any MOTs we can scatter at most a few photons. Additionally, this fact prevents the use of any traditional Zeeman slower as a Zeeman slower works by shifting the transition frequency to stay on zero-field resonance to compensate for the Doppler shift on an atomic or molecular beam. You may be clever and try to flip the polarization suddenly to get out of the dark state however, you would optically pump into a stretched state with the wrong detuning.

So why don't we just avoid using Type-II transitions? You may recall in the previous chapter when discussing the angular momentum branching ratios we declared we were going to be clever and drive  $X^2\Sigma^+, N = 1^- \rightarrow A^2\Pi_{1/2}, J = 1/2^+$  transition to limit rotational branching. Recall that any rotational ground state can be recast into a linear combination of states in the Hunds case (a) basis with total angular momenta  $J = N \pm 1/2$ . As such, we will always be driving type-II transitions [68]. This is the trade-off, either have rotational branching or type-II transitions. We will opt for having type-II transitions and we will see that we exploit the dark states to great effect for both sub-Doppler cooling in free space and in conservative traps, and for magneto-optical trapping.

## 3.2 Doppler Cooling Theory and Slowing

### 3.2.1 Doppler Cooling Theory

To perform laser slowing we want a velocity-dependent force using light that we can apply to a molecular beam. The force from stimulated absorption and then spontaneous emission at low intensity (rabi frequency lower than the linewidth) is,

$$\vec{F} = \hbar\vec{k}\Gamma_{scat} = \hbar\vec{k}\Gamma\rho_{ee}. \quad (3.1)$$

Where  $\vec{k}$  is the wavevector,  $\Gamma_{scat}$  is the scattering rate,  $\Gamma$  is the linewidth of the excited state transition and  $\rho_{ee}$  is the excited state population. The definition of the excited state population is well known for a multilevel system with my favorite references being [67],[49], and [80]. In particular [80] contains a very succinct set of rate equations for the massive multilevel systems in molecules where  $\rho_{ee}$  is defined as,

$$\rho_{ee} = \frac{n_e}{(n_e + n_g) + 2 \sum_{j=1}^{n_g} \left(1 + \frac{4\Delta_j^2}{\Gamma^2}\right) \frac{I_{s,j}}{I_j}}. \quad (3.2)$$

Where  $n_e$  and  $n_g$  are the numbers of excited and ground internal spin states,  $j$  denotes a transition with a detuning  $\Delta_j$  and a saturation intensity  $I_{s,j} = \frac{\pi h c \Gamma}{3 \lambda_j^3}$ . So how is this expression velocity dependent? It comes in the detuning which we can write as  $\Delta_j = \delta_j - \vec{k} \cdot \vec{v} - (g_e M_e - g_j M_j) \mu_B B / \hbar$ . Here  $\delta_j$  is the laser detuning the second term is the Doppler shift which is velocity dependent and the last term would be the differential Zeeman shift from the excited state to the ground state where B (magnetic field) could be position dependent if a gradient field was applied for a MOT.

So our goal is to adjust the detuning of the laser  $\delta_j$  to be equal to  $\vec{k} \cdot \vec{v}$  to ensure the scattering force is maximized to get the best slowing. Since we cannot use a traditional Zeeman slower as was discussed in the previous section we will use chirped laser-cooling where we will continuously chirp the laser frequency corresponding to a decelerating molecular beam to keep the detuning on resonance (detuning within the linewidth). This corresponds to a linear frequency chirp of all the laser frequencies from red-detuned to near zero-velocity resonance. The first demonstration of chirp laser-cooling was performed by early experiments by Bill Phillips, with chirped laser-cooling to zero velocity and velocity reversal done by John Hall and Zhu in [29].

Additionally, if you apply Eq.3.2 in all six directions and you expand the force at small velocities you get a damping force  $F_{mollase} \approx -\alpha \vec{v}$  where  $\alpha$  is a damping coefficient that depends on the detunings and intensities of the relative laser beams. This configuration of laser beams interacting with the atomic or molecular ensemble is known as optical molasses. So what does an

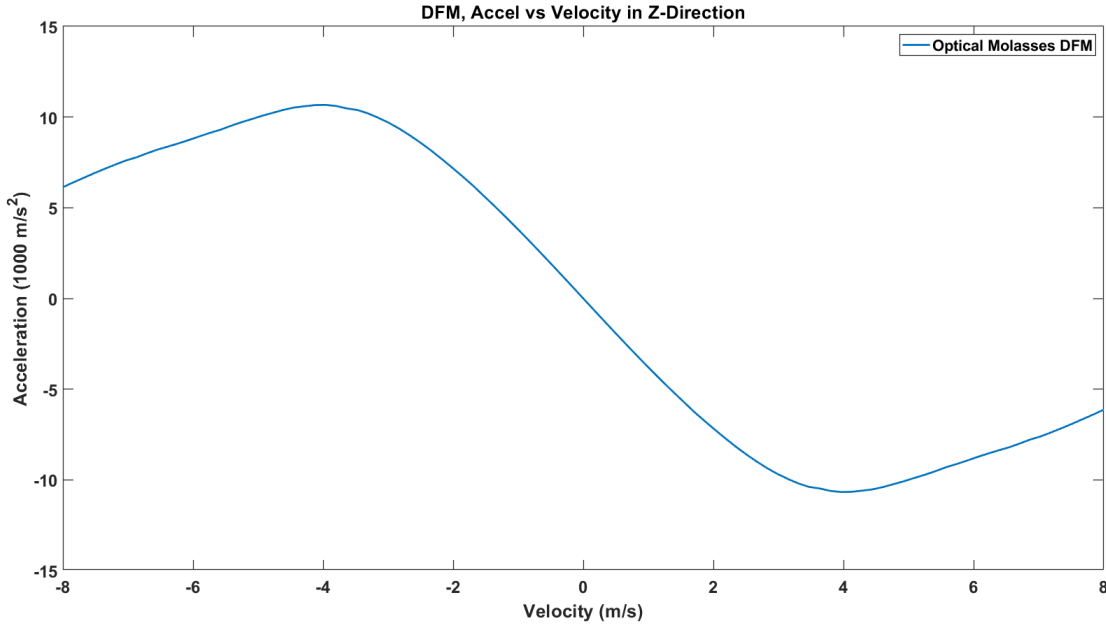


Figure 3.2: Full rate simulation of damping force for the Dual-Frequency MOT for YO molecules.

actual acceleration vs. velocity look like? In general, it looks like the difference of two Lorentzian curves which gives a dispersive curve. As an example using Eq.3.2 including all branching ratios, all spin states, all laser detunings, corresponding intensities, all correct polarizations, and hyperfine manifolds a simulation of our first MOT the Dual-Frequency MOT is shown Fig.3.2 where we can see a clear dispersive curve creating a retarding force over a range of  $\pm 3.5$  m/s.

There is an interesting limit known as the Doppler limit which corresponds to the minimum temperature achievable in a standard red detuned laser-cooling. The limit for a two-level system is  $T_D = \frac{\hbar\Gamma}{2k_b}$  and is the result of the fluctuation-dissipation theorem in three dimensions defined as,

$$k_b T = \frac{D_p}{3\alpha} = \frac{\hbar^2 k^2 \Gamma_{scat}}{3\alpha}. \quad (3.3)$$

Here  $D_p$  is the momentum diffusion constant and is the result of the random fluctuations in photon scatters resulting in heating [49]. For reference, I have placed the Doppler temperatures for a few transitions in YO. I have also placed a limit known as the recoil limit to the table as well which represents the minimum temperature achievable by standard Doppler laser-cooling defined as

**Doppler-Temperatures and Recoil-Temperatures of YO Molecules**

	<b>Doppler-Temperature</b>	<b>Recoil-Temperature</b>
$X^2\Sigma^+ \rightarrow A^2\Pi_{1/2}$	<b>115 <math>\mu\text{K}</math></b>	<b>484 nK</b>
$X^2\Sigma^+ \rightarrow A'^2\Delta_{3/2}$	<b>168 nK</b>	<b>384 nK</b>

$T_R = \frac{\hbar^2 k^2}{mk_b}$ . This limit can be beaten using coherent mechanisms such as velocity-selective coherent population trapping (VSCPT).

We can see an enticing prospect as the minimum temperature achievable on the narrowline transition  $X^2\Sigma^+ \rightarrow A'^2\Delta_{3/2}$  is photon recoil limited, and indeed these narrow transitions have become powerful tools in alkaline earth elements for quantum state manipulation and cooling. We will also see however in the following sections that the Doppler limit is also handily defeated due to interesting coherence in the ground state sub-manifolds present in optical molasses.

However, turning our attention back to chirped laser-cooling of a molecular beam it would be nice if there were a simplified version of Eq.3.2. If we make a couple of assumptions (which are generally true when performing the experiment) that the total intensity  $I_{tot}$  is equally divided among the transitions and the detunings  $\Delta$  are all the same we get a set of simplified equations [80],

$$\Gamma_{scat} = \frac{\Gamma_{eff}}{2} \frac{s_{eff}}{1 + s_{eff} + \left(\frac{4\Delta^2}{\Gamma^2}\right)}, \quad (3.4)$$

$$\Gamma_{eff} = \frac{2n_e}{n_g + n_e} \Gamma, \quad (3.5)$$

$$s_{eff} = \frac{2(n_e + n_g)}{n_g^2} \frac{I_{tot}}{I_s}. \quad (3.6)$$

First, we see that the form of Eq.3.4 is similar to that of a two-level system which gives great intuitive understanding. The other two equations define an effective linewidth and saturation intensity  $\Gamma_{eff}$ ,  $s_{eff}$  which are extremely useful quantities for the quick back-of-the-envelope calculations in the lab.

### 3.2.2 Chirped Laser Slowing

Now with a basic understanding of the level structure, vibrational branching, rotational branching, and laser-cooling, let's laser cool some molecules! First, we need a full picture of the level diagram with the corresponding lasers and microwaves that combine all the vibrational and rotational branching we discussed in the previous chapter.

This diagram is given in Fig.3.3 and is a slightly busy diagram but it is easy to go through step by step. First, we want to laser cool on  $v = 0, X^2\Sigma^+, N = 1^- \rightarrow v = 0, A^2\Pi_{1/2}, J = 1/2^+, F = 0, 1$  as stated multiple times and is shown as one of the orange arrows in the diagram. Recall that we have detrimental branching up to  $v = 2$  in the ground state from the Frank-Condon factors. To address this we will first repump the  $v = 2$  ground state manifold by applying a laser on  $v = 2, X^2\Sigma^+, N = 1^- \rightarrow v = 1, A^2\Pi_{1/2}, J = 1/2^+, F = 0, 1$ . This will optically pump all the population into  $v = 1$ . To repump all the  $v = 1$  population (recall is the largest branching) we apply a laser driving  $v = 1, X^2\Sigma^+, N = 1^- \rightarrow v = 0, A^2\Pi_{1/2}, J = 1/2^+, F = 0, 1$  bringing all the population back onto the main cycling transition. That covers all the vibrational branching.

For the rotational branching due to the  $A^2\Delta_{3/2}, J = 3/2^\pm$  state we apply two orange lasers on the  $v = 0$  manifold to repump the  $N = 2$  and  $N = 3$  population. Specifically we drive both  $v = 0, X^2\Sigma^+, N = 2^+ \rightarrow v = 0, A^2\Pi_{1/2}, J = 3/2^-, F = 2$  and  $v = 0, X^2\Sigma^-, N = 3^- \rightarrow v = 0, A^2\Pi_{1/2}, J = 5/2^+, F = 3$ . For all the other rotational manifolds we apply microwaves mixing  $v = 0, N = 0 \rightarrow N = 1$  states and  $v = 1, N = 0 \rightarrow N = 1 \rightarrow N = 2$  and  $v = 2, N = 0 \rightarrow N = 1 \rightarrow N = 2$ . The details of the microwaves are given in Fig.2.15. Currently, we do not repump any population that builds up in  $v = 1, 2, N = 3$  which limits the current MOT lifetimes. One caveat I will say here is that during laser slowing we only apply microwaves on  $v = 0, N = 0 \rightarrow N = 1$  and begin sweeping the microwaves during the MOTs.

Next, we need to address each of the hyperfine manifolds in  $v = 0, 1, 2, X^2\Sigma^+$ . Recall that in YO there is a large Fermi-contact interaction that splits the  $G = 0$  and  $G = 1$  singlet and triplet states by around 770 MHz as shown in Fig.3.3. To drive all the population we put the lasers on the

### Complete Laser-cooling Diagram for YO

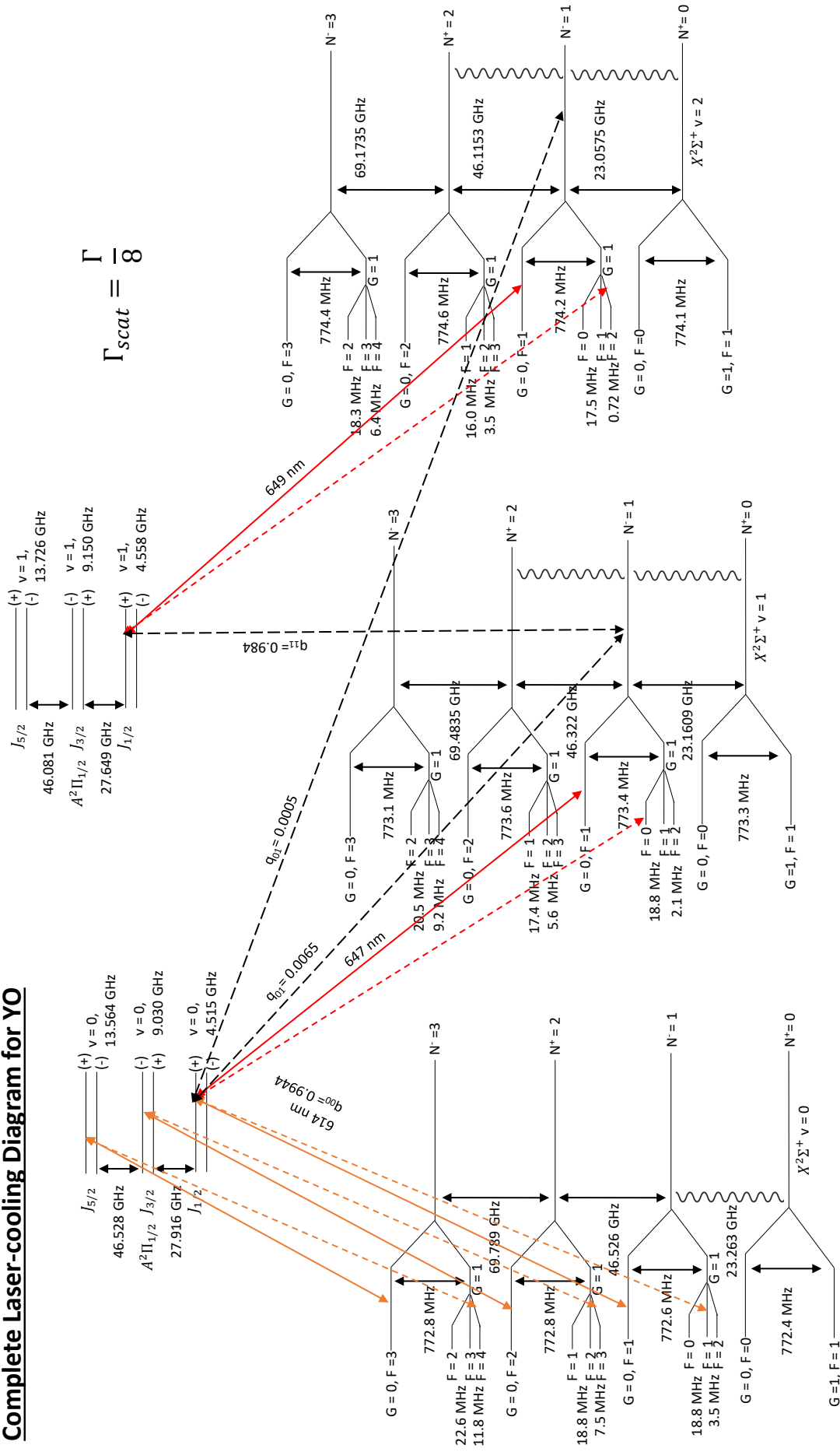


Figure 3.3: Full laser-cooling diagram of YO including all vibrational and rotational repumps and microwave remixing.

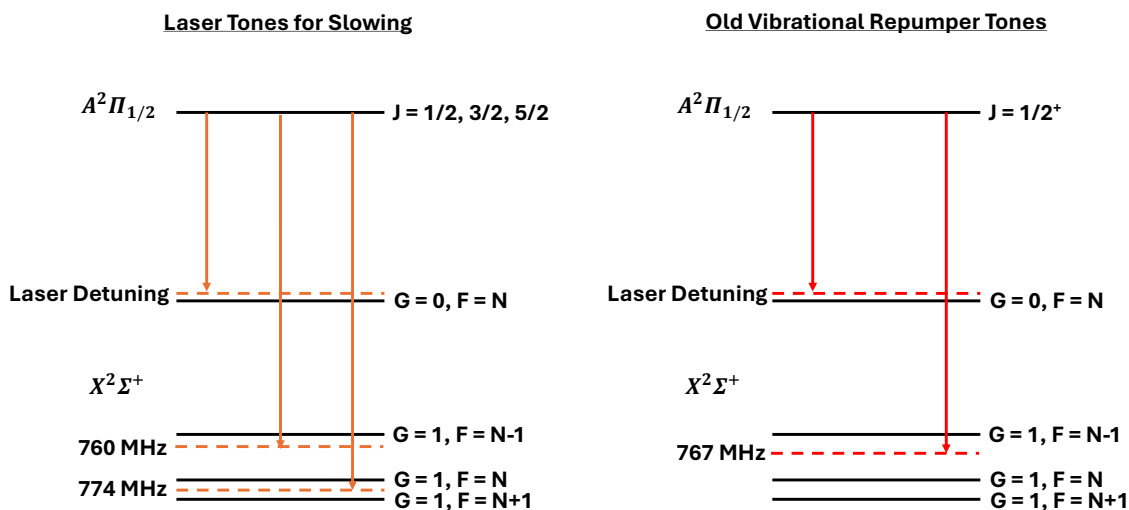


Figure 3.4: Laser tones used for slowing are shown in the left diagram. The laser is placed on the  $G = 0$  manifold and two tones generated by high-frequency AOMs address the  $G = 1$  manifolds with tones at 760 and 774 MHz. The right diagram shows the old vibrational repump tones which were inefficient and did not repump all the population effectively.

$G = 0$  manifolds and we generate two tones at 760 and 774 MHz by dual driving high frequency Brimrose AOMs and focusing the lasers through them to address the  $G = 1$  manifolds. Through combinations of polarizing and non-polarizing beam splitters and dichroic mirrors, we combine all 15 laser tones and send them through a single viewport toward the buffer-gas cell where the beam of YO molecules is generated. Additionally, all the lasers propagate through a telescope and a long focal lens to expand the beam at the viewport and to gently focus the beam to the buffer gas cell aperture. This creates nonlinear scattering rates as the molecules are decelerated. This is done however to ensure that the wavevectors of the lasers never have a component outwards transverse to the molecules to prevent extra pluming of the beam.

To visualize this, the relevant detunings and a mock level structure are shown in the left diagram in Fig.3.4. The right diagram is the scheme that used to be used for the vibrational

repumping when I joined the experiment. This scheme was ineffective at repumping the vibrational population in the  $G = 1$  manifolds. Now all lasers in the experiment use the scheme in the left diagram and this change boosted the slowed molecule number drastically which will be shown shortly and was a major boost for later work on collisions. One key aspect is the repumping of the dark states caused by being on type-II transitions as was discussed in the previous section. To repump all the manifolds all the slowing beams go through a Conoptics Pockel cell which chops the polarization between  $\sigma^\pm$  polarizations at a rate of 1.5 MHz, which is much higher than the scattering rate. This also has the effect of putting sidebands on all the laser tones at  $\pm 1.5$  MHz. Since there is a strong degree of coherence in the laser tones on the  $G = 1$  manifold, a forest of tones appears due to the beating of the different tones.

The molecules are generated by ablation of a  $Y_2O_3$  ceramic target held at 3.5 K in a cryogenic buffer gas cell. The ablation is generated by an Inlite 532 nm q-switched laser with a peak energy of around 9 mJ and pulse width of around 6 ns. The ablation of the target generates YO and every ion and radical of YO you can imagine. Helium flows into the cell at 4 K at a rate of  $\approx 0.25$  sccm. Collisions of the YO molecules with the helium buffer gas quench the internal states into the lowest vibrational state and lowest four rotational manifolds  $N = 0-3$ . The molecules have a dwell time of around 2 ms before leaving through a few mm aperture in the front of the cell. This creates a collimated molecular beam of YO with a nominal forward velocity of 120 m/s.

The optimal time sequence for slowing is as follows. The lasers are chirped 163 MHz from red to blue detuned over 14.7 ms. This slows the molecules from 120 to 20 m/s. This corresponds to a deceleration rate of  $6800 \text{ m/s}^2$  which is lower than what you would predict using Eq.3.4 and 3.1. This suggests there is a significant improvement that could be had in the slowing. The distance the molecules are slowed over is 1.16 m. Two in-vac shutters open and close with timing optimized for the decelerating molecular beam. These are critical to prevent helium from accelerating the beam and reducing the effect of the helium flow on the vacuum lifetime in the main experimental chamber.

The last slowing from 20 m/s to around 3 m/s which is the capture velocity of the MOT as

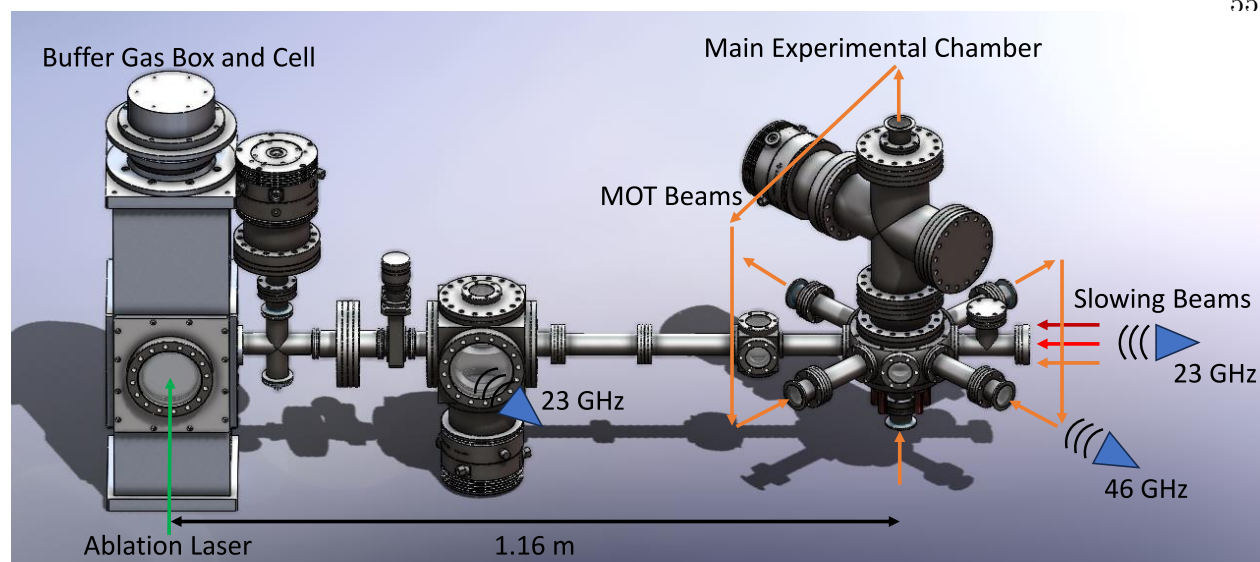


Figure 3.5: CAD model of the experimental apparatus with labels of beam propagations and microwave horns. The MOT beams enter through the bottom of the chamber and are retroreflected with a  $\lambda/4$  waveplate after the final pass.

we can see from Fig.3.2, is performed by leaving the main cycling laser detuned 32.6 MHz and off resonantly scattering to the final velocity to avoid pushing the molecules backward. However, all the repump lasers are chirped to zero velocity resonance over 9 ms. This extra chirp time used to be very sensitive in its length, but after adding more tones to the repump lasers it is not too sensitive anymore, and can be adjusted to around  $\pm 3$  ms without any detrimental effect. This means the entire slowing sequence takes 23.7 ms. The main slowing laser is then shuttered leaving the repump lasers propagating down the slowing axis and the molecules are loaded into the MOT.

To get a picture of what the apparatus looks like and what the beam geometries look like, a CAD model of the experiment labeling the relevant beams and microwave locations is shown in Fig.3.5. Typical PMT traces of the slowing and MOT loading are shown in Fig.3.6. We can see a peak of slowed molecules occurring at 23 ms and the molecules then slowly drift into the MOT beams while being careful not to blow them backward with resonant light. The MOT beams then capture the molecules noted by the peak in fluorescence around 45 ms.

Note the dramatic difference in the number of slowed molecules with the extra repump tones

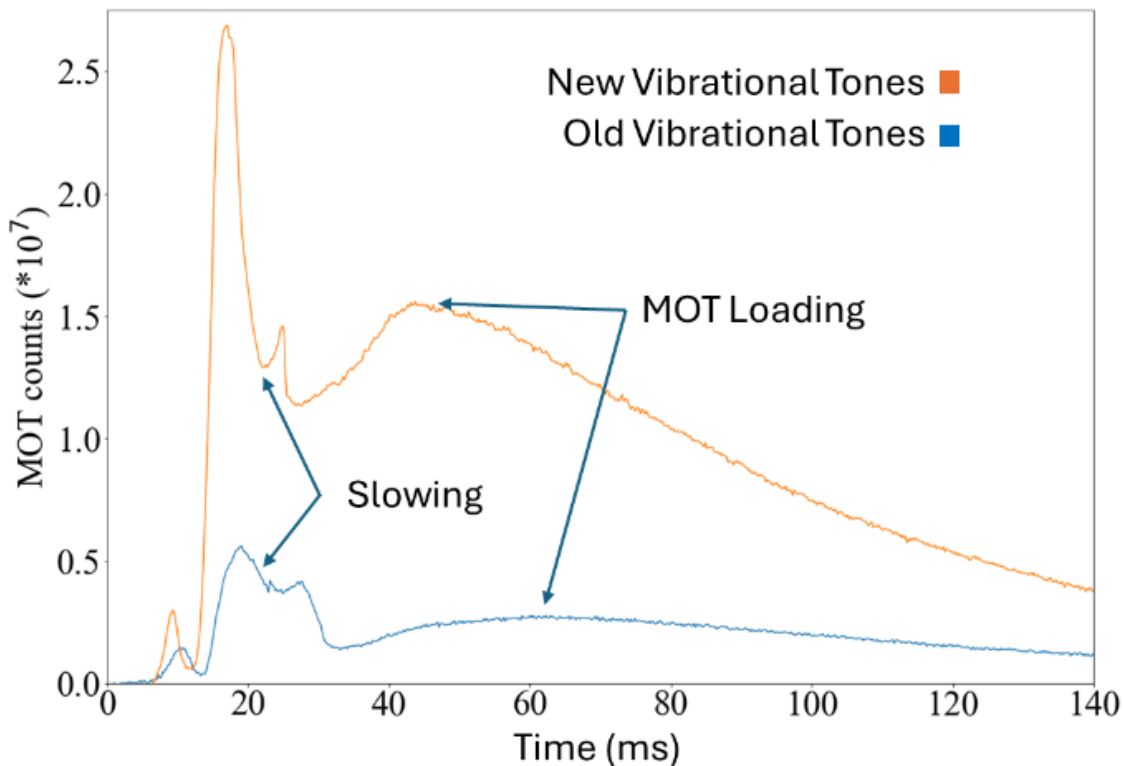


Figure 3.6: Shown are typical slowing and MOT loading traces on the experiment decelerating molecules with a peak forward velocity of 120 m/s. The two traces correspond to different tones on the repump lasers as depicted in Fig.3.6.

on the vibrational repumps. This corresponded to a factor of 5 increase in the molecular number almost immediately. This is probably the largest improvement during my PHD on the actual slowing of the molecules. As I had stated before, I believe there is much more improvement that could probably be made in the chirp rates, powers, detunings, etc. along with decoupling the  $v = 1$  laser from the main cooling cycle by repumping through the  $B^2\Sigma^+$  state. These changes will need to be made if there is to be a serious effort for evaporative cooling of YO molecules to degeneracy. The little spike on both traces at around 24 ms is when the main cooling laser addressing  $v = 0, X^2\Sigma^+, N = 1^- \rightarrow v = 0, A^2\Pi_{1/2}, J = 1/2^+, F = 0, 1$  for chirped slowing is shuttered. The rest of the fluorescence captured afterward is from the MOT beams.

### 3.3 Sub-Doppler Cooling

In this section, we are going to discuss interesting physical phenomena present in optical molasses that provide a larger velocity-dependent damping force  $\alpha$  than that provided by the Doppler force. In turn, this will provide temperatures lower than the Doppler temperature discussed earlier Eq.3.3. The simple physical reasoning is that a coherence between different ground-state magnetic sub-levels is created with a coherence time longer than the excited state lifetime. This can be understood through the energy-time uncertainty relation where the standard Doppler limit can only be beaten if there is a longer time between each spontaneous emission event. Such sub-Doppler cooling is generally called ground-state cooling and was seen very early on in laser-cooling of atomic species first by Bill Phillips et al. [42], and was theoretically described by Jean Dalibard and Cohen-Tannoudji [21]. Before we can discuss these mechanisms, however, we need to discuss another force associated with the interaction of atoms and molecules with light, the dipole force.

#### 3.3.1 The Dipole Force

In the previous section, we discussed the scattering force and its use to effectively remove entropy from an atom or molecule by absorption of a photon and subsequent spontaneous emission. Since this phenomenon removes energy from the system this force is non-conservative. Indeed we even noted that this force is proportional to the velocity of the cold ensemble of atoms or molecules in an optical molasses not meeting the definition of a conservative force.

However, there is another force associated with the interaction of light with a resonant system (like atoms or molecules) and it is called the dipole force. This force is conservative meaning that  $\vec{F}_{dip} = -\vec{\nabla}V_{dip}$ . The dipole potential  $V_{dip}$  is defined as [67] (pg. 42),

$$V_{dip} = -\frac{1}{2\epsilon_0 c} \text{Re}[\alpha(\omega)] I(r, z). \quad (3.7)$$

First  $I(r, z)$  is the intensity of the interacting light field since we generally want strong coherent interactions the intensity will be formed by a laser beam with a Gaussian beam profile

defined as,

$$I(r, z) = \frac{2P}{\pi\omega^2(z)} e^{-2\frac{r^2}{\omega^2(z)}}. \quad (3.8)$$

Here  $P$  is the power in the laser beam,  $r$  is the radial coordinate,  $z$  is the axial coordinate (propagation direction of the beam), and  $\omega$  is the beam waist of the beam. You can imagine if we have an intense laser beam focus on the molecules you may be able to generate a conservative trapping force as long as  $Re[\alpha(\omega)]$  is positive. This is the exact physical mechanism behind optical conservative traps called "dipole traps", or depending on the polarization of the beams and the number of beams an "optical lattice".

Continuing with the definition of the dipole potential in Eq.3.7 the term  $\alpha(\omega)$  is called the polarizability (please do not be confused by  $\omega$ , for intensity it is the beam waist, but generally in all other cases it is an angular frequency of the light field  $\omega$  or transition in the molecule or atom  $\omega_0$ ) which is defined as  $\vec{\mu} = \alpha(\omega)\vec{E}$ . In the most simple terms, the polarizability gives a "measure" of the ability of the physical system of interest to acquire a dipole moment  $\mu$  which we discussed in length in Chapter 1, and is generally dependent on the frequency of the driving light field  $\omega$ . Here  $\vec{E}$  is the electric field vector of the light field. Writing the dipole moment in this form is convenient as the interaction of light is a second-order perturbation in the interaction potential Eq.3.7. However with the polarizability, the interaction with the light field "looks like" it is to first order. This makes it easy to understand and determine the matrix elements of the interaction. For more information on this, I suggest reading [67] (section 7.7).

Before we discuss the form of  $\alpha(\omega)$  there is an interesting relation between the scattering force and dipole force where the scattering rate can be written as [67] (pg.43),

$$\vec{F}_{scat} = \frac{1}{2\hbar\epsilon_0 c} \frac{\omega^2}{\omega_0^2} Im[\alpha(\omega)] I(r, z). \quad (3.9)$$

We found a very interesting relation here where the dipole force is related to the "dispersive" part of  $\alpha(\omega)$  and the scattering force is related to the "absorbative" part of  $\alpha(\omega)$ . This is the result

of an interesting mathematical relation called the Kramers–Kronig relation which I will not go into more detail.

So what does  $\alpha(\omega)$  look like? Its form can be derived from a simple Lorentz model of an atom or molecule interacting with an oscillating electric field with the best description I have read being [67] (Chapter 1). Making some simplifications and assuming that the detuning of the light field is greater than the linewidth of the transition  $|\omega - \omega_0| = \Delta \gg \Gamma$ , the dipole potential, and the polarizability can be written as [67] (pg. 42),

$$V_{dip} = \sum_j \frac{\hbar\Gamma_j^2}{8} \left( \frac{1}{\omega - \omega_{j0}} + \frac{1}{\omega + \omega_{j0}} \right) \frac{I(r, z)}{I_{sat,j}}. \quad (3.10)$$

The sum is overall excited transitions that have a transition dipole moment to the ground state of interest. First note that this expression provides a negative energy shift for detunings  $\Delta < 0$  and that the excited state shift is opposite in sign. The second term in the parenthesis is called the counter-rotating term and is generally so small it can be neglected for the work in this thesis. This dipole potential is also known as the ac-Stark shift from the interacting light field. We can further simplify this expression using the results for a two-system interacting with an oscillating light field using the relation  $\frac{I}{I_{sat}} = \frac{2\Omega^2}{\Gamma^2}$ . Here  $\Omega$  is the Rabi-frequency defined as,

$$\Omega = \frac{\langle g | \vec{\mu} \cdot \vec{E} | e \rangle}{\hbar} \quad (3.11)$$

and quantifies the energy scale of the coupling to the electromagnetic field, and we have seen the return of one of our favorite quantities the transition dipole moment. Making the substitution we get the the ac-Stark shift (dipole potential),

$$V_{ac} = \sum_j \frac{\hbar\Omega_{i \rightarrow j}^2}{4\Delta_{i \rightarrow j}}. \quad (3.12)$$

Here we are summing over the excited states  $j$  connecting to the ground state  $i$ . Note that the ac-Stark shift is proportional to the square of the Rabi-frequency meaning it is dependent on the intensity of the light field and the square of the transition dipole moment. Now with this

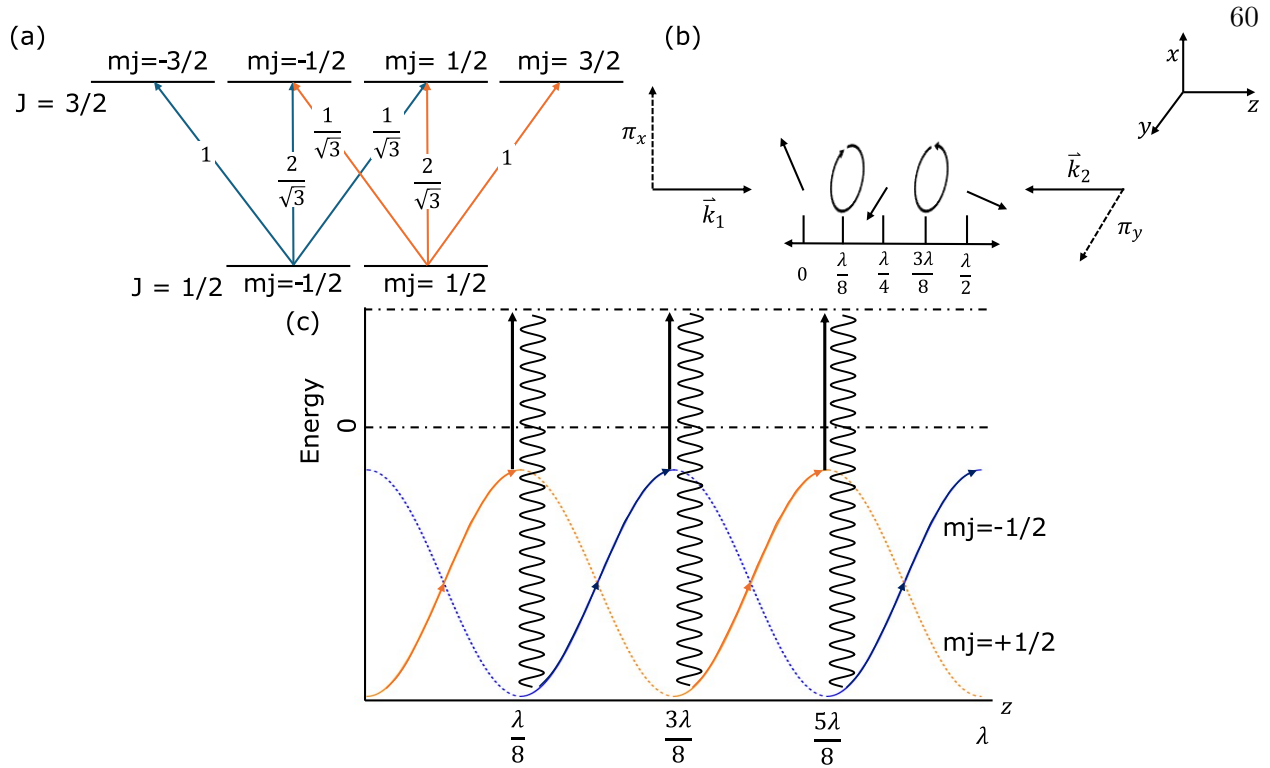


Figure 3.7: (a) Clebsch-Gordan coefficients for a  $J = 1/2 \rightarrow J = 3/2$  transition. We note that the stretched transitions that drive outwards are the strongest with a CG coefficient of 1. (b) Two counter-propagating waves with perpendicular linear polarization (known as lin-perp-lin) create a polarization gradient whose polarization changes to a pure polarization every one-eighth of a wavelength and changes between linear polarization to circular polarization with a determined handedness and constant electric field amplitude of  $\sqrt{2}E_0$ . (c) If the laser light is red-detuned molecules move through the polarization gradient and the different magnetic sublevels experience ac-Stark shifts both shifted red of the bare state energy. Effectively the molecules will be moving up potential hills converting their kinetic energy into internal potential energy in the magnetic-sublevels. The molecules will then be optically pumped into the opposite magnetic sub-level by excitation and spontaneous emission of a photon. This photon carries away the excess energy from the ac-Stark shift reducing the thermal energy of the molecules. If the optical pumping time is  $\tau_p \approx \frac{\lambda}{4v}$  on average the molecules will always be climbing potential hills and the damping force will be maximal.

formulation, we can describe not only sub-Doppler cooling but also conservative trapping which we will discuss later in this thesis at length.

### 3.3.2 Polarization Gradient Cooling

Now that we have discussed the dipole force we can now discuss the simplest form of sub-Doppler cooling in an optical molasses known as polarization gradient cooling. The simplest ex-

ample is that of a molecule or atom with a ground state angular momenta of  $J = 1/2$  being driven by an oscillating electric field to an excited state with angular momenta  $J = 3/2$ . The relative Clebsch-Gordan coefficients are shown in Fig.3.7 (a) where we see that transitions that drive between the most outward magnetic sublevels ( $m_j = 1/2 \rightarrow m_j = 3/2$  or  $m_j = -1/2 \rightarrow m_j = -3/2$ ) are the strongest with a Clebsch-Gordan coefficient of 1. The field is generated by two counter-propagating beams along  $z$  with linear polarizations that are perpendicular to each other. This creates a field profile of [21],

$$\vec{E}(z) = \sqrt{2}E_0 \left( \cos(kz) \frac{\hat{e}_x + \hat{e}_y}{\sqrt{2}} - i \sin(kz) \frac{\hat{e}_y - \hat{e}_x}{\sqrt{2}} \right) \quad (3.13)$$

where at all points along the  $z$  direction we have a constant amplitude of  $\sqrt{2}E_0$ . What is more interesting however is that as we translate along the  $z$  direction we can see that polarization is changing, and every one-eighth of a wavelength we transition from pure linear polarization to circular polarization with a particular handedness. This is shown diagrammatically in Fig.3.7 (b). We assume the quantization axis is set by the light field.

We have now arrived at a fascinating consequence of this geometry. For example, imagine we are at a position of  $\lambda/8$  as shown in Fig.3.7 (b) on the  $z$ -axis. Here the light is pure left-handed circular polarization. If we turn our attention back to Fig.3.7 (a) we see that the light field will drive  $\sigma^-$  transitions. Specifically it will drive  $m_j = -1/2 \rightarrow m_j = -3/2$  and  $m_j = 1/2 \rightarrow m_j = -1/2$ . We now arrive at the most important point in this discussion. We note that these two transitions have different Clebsch-Gordan coefficients (their square being the angular momentum branching ratios) of 1 and  $1/\sqrt{3}$ . We now go back to Eq.3.12 where the ac-Stark shift is dependent on the square of the Rabi-frequency and the Rabi-frequency is dependent on the transition dipole moment which includes the angular momentum branching ratios. As such, for a fixed detuning and intensity, the two different magnetic sublevels will have different ac-Stark shifts proportional to the square of the respective Clebsch-Gordan coefficients. If we let the ac-Stark shift be equal to  $\chi'$  then the shifts are going to be between the sub-levels are going to be  $V_{ac}, m_j = 1/2 = \chi'/3$  and  $V_{ac}, m_j = -1/2 = \chi'$ .

If for example, we were at a position of linear polarization on the z-axis such as  $\lambda/2$  then the light field will drive the transitions  $m_j = -1/2 \rightarrow m_j = -1/2$  and  $m_j = 1/2 \rightarrow m_j = 1/2$  and the ac stark shift of the states will be the same as the branching ratios are the same. So, as we move through the polarization gradient the magnetic sub-levels will experience differential stark shifts depending on the position along the z-axis. If the driving field is red detuned both the stark shifts will be negative with different strengths relative to the bare state energy. This can be seen at the bottom of Fig.3.7 (c).

Now let us imagine that we have a thermal ensemble of atoms or molecules. They will move through the polarization gradient and will have a position-dependent potential energy caused by the ac-Stark shift of the magnetic sub-levels. For example, let our ensemble start at  $\lambda = 0$  in the  $m_j = 1/2$  sublevel and move along the  $+z$  direction. As the ensemble moves, the potential energy of the sub-level increases, and correspondingly the kinetic energy of the ensemble decreases as it moves up the hill shown by the arrows in Fig.3.7 (c). With the maximum differential stark shift experienced first at  $\lambda/8$ . We know, however, that besides the dipole force, there is a scattering force where beyond the stimulated emission of photons a spontaneously emitted photon can occur. If for example, this were to occur at  $\lambda/8$  (which does occur with the highest probability as we are closer to bare state energy) the light field would drive the transition  $J = 1/2, m_j = 1/2 \rightarrow J = 3/2, m_j = -1/2$ . We know however from Chapter 2, that spontaneous emission would allow decay to either magnetic sub-level in  $J = 1/2$ , and it turns out the transition dipole moment is stronger for the decay from  $J = 3/2, m_j = -1/2 \rightarrow J = 1/2, m_j = -1/2$  than  $J = 3/2, m_j = -1/2 \rightarrow J = 1/2, m_j = 1/2$  as the branching ratios are  $2/3$  and  $1/3$  respectively! As such, the ensemble will be optically pumped into the opposite magnetic sub-level which coincidentally, is experiencing a maximal ac-Stark shift.

In this situation, the spontaneously emitted photon shown by the squiggly line in Fig.3.7 (c) must carry away additional energy proportional to  $\hbar\chi'$ . This cycle will then repeat itself and the ensemble will continuously climb up potential hills and will be reset by optical pumping losing energy continuously. This is much like the greek myth of Sisyphus and this type of cooling is

colloquially known as "Sisyphus Cooling". What has been essentially created is a ground state "lifetime" where a magnetic sub-level will be populated by a period that we call the optical pumping time  $\tau_p$  with the lifetime being defined as  $\Gamma' = \frac{1}{\tau_p}$  much akin to a spontaneous emission rate. This optical pumping time is effectively a coherence time associated with the population between magnetic sublevels. The maximum damping force occurs if the Doppler shift  $kv$  is proportional to the ground state lifetime. It turns out that if you calculate the damping coefficient for this effect you find  $\alpha \approx -\hbar k^2 \frac{\Delta}{\Gamma}$  which is larger than that of a standard optical molasses by the term  $\frac{\Delta}{\Gamma}$  which is large as we had assumed when discussing the ac-Stark shift that  $|\Delta| \gg \Gamma$  [21]. Additionally, we find that this damping rate is independent of intensity which is not the case if the damping coefficient is only dependent on the Doppler effect.

### 3.3.3 $\Lambda$ -Enhanced Gray Molasses Cooling

The mechanism that we will use to sub-Doppler cool YO molecules is similar to that used in polarization gradient cooling as it will rely on a Sisyphus mechanism, but it is fundamentally different. The difference depends upon the type of hills that the molecules will climb up to remove kinetic energy. This physical mechanism is called Gray-Molasses-Cooling (GMC) and was first identified by Ted Hansch et al. [79]. The advantage of this cooling is that it works on Type-II transitions which we discussed we work on exclusively when laser-cooling molecules and is hyper-efficient. Sub-Doppler cooling of YO molecules was the first work I was a part of in my PHD thesis.

The basic physical mechanism is as follows, if the molecules are subjected to a polarization gradient like in Fig.3.7 (b) at all points in the gradient there will be a position-dependent dark state as again, for any polarization in a type-II transition there is a state or linear combination of states that is dark to the light field. When we say "dark" we mean that state(s) are no longer interacting with the field. However, the bright states (not dark) will experience a position-dependent Stark shift from intensity gradients and polarization gradients. At the intensity maxima of the intensity gradients, the molecules will be optically pumped into the dark state. Note immediately that the

lin-perp-lin polarization gradient has no intensity gradients in 1D as such there is no GMC cooling in this case [25]. To have cooling in 1D you would need to have the polarization impinge at each other at an angle other than 0 or 90 degrees.

So let us recap the physical picture, if the molecules are in a bright state they will experience a spatially varying ac-Stark shift and will be optically pumped into a dark state at the intensity maxima. This already seems very similar to the case of Sisyphus cooling as we discussed in Fig.3.7. However, we are missing one aspect. If the molecules are in the dark state, how do they transition to the bright state? The argument is subtle. It turns out that these bright states and dark states are orthogonal to each other in that they create a linearly independent eigenbasis. These basis states are normally called  $|C\rangle$  and  $|NC\rangle$  which represent the bright and dark states and are named coupled and non-coupled referring to the coupling to the light field. An energy gap exists between these states due to an AC stark shift of the bright state. These states are not eigenstates of the kinetic energy operator. As such, there is coupling between the states proportional to the velocity of the molecules  $\langle NC | \frac{p^2}{2m} | C \rangle \propto v$ . This means the higher the velocity which is proportional to the temperature of the molecules the higher the transition rate. This is closely related to the phenomena called VSCPT or "Velocity Selective Coherent Population Trapping" [4]. The coupling is called "non-adiabatic" as it goes to zero as the velocity goes to zero and is strongest as the intensity minima experienced by the bright state as the energy difference between  $|C\rangle$  and  $|NC\rangle$  is minimized. Note this is only true for blue-detuned light. As such GMC cooling relies on the detuning of the light field to be blue on the relevant transition for cooling. If the light field is red-detuned you will have heating.

We now have a full picture of our Sisyphus cooling mechanism. If the molecules start in the dark state they can make a non-adiabatic transition to the bright state at the intensity minima of the light field. As the molecules move in the bright state their kinetic energy turns into internal potential energy due to the increasing ac-Stark shift moving through the polarization/intensity gradients. At the intensity maxima of the gradient, the molecules will be optically pumped through spontaneous emission to the dark state losing energy proportional to the ac-Stark shift  $\chi'$ . This

process repeats itself completing the cycle for Sisyphus cooling.

So where does the  $\Lambda$ -Enhanced part come into this cooling? Well, we can use two light fields to couple two different ground manifolds to a particular excited state in a  $\lambda$  type scheme. Here the light fields both have an intensity  $I$ , a common detuning  $\Delta$  called the "one-photon detuning", and a differential detuning  $\delta$  called the "two-photon detuning". In this scheme, you can create a coherent dark state when  $\delta = 0$  as the coherent population transfer to the excited state from the two different ground states destructively interfere with each other creating a robust dark state. This is closely related to the phenomenon of "Electromagnetic Induced Transparency" EIT for short and again VSCPT. My favorite reference on this subject is [67], (Chapter 6). The entirety of the  $\Lambda$ -Enhanced GMC is shown diagrammatically in Fig.3.8.

### 3.3.4 Sub-Doppler Cooling of YO Molecules

In this section, I will summarize our results on  $\Lambda$ -Enhanced GMC of YO molecules with the published work found here [27]. Similar work has been demonstrated in other laser-cooled molecules as well [42] [77],[41] and [16]. However, at the time of writing this thesis, YO remains by far the coldest bulk molecular sample in both free space and in conservative traps. This is mostly due to its favorable ground state structure as the ac-Stark shift cross-coupling between the different G manifolds is negligible due to their large splitting of  $\approx 760$  MHz.

So to perform  $\Lambda$ -Enhanced GMC there are only three parameters that need to be optimized. First is the intensity which in the following discussion will always be equally split between the two transitions we will be driving in a  $\lambda$  scheme. The other two parameters are the one-photon detuning and two-photon detuning  $\Delta$  and  $\delta$ . The transitions we will be driving are  $v = 0, X^2\Sigma^+, N = 1^-, G = 0, F = 1 \rightarrow v = 0, A^2\Pi_{1/2}, J = 1/2^+, F = 0, 1$  and  $v = 0, X^2\Sigma^+, N = 1^-, G = 1, F = 2 \rightarrow v = 0, A^2\Pi_{1/2}, J = 1/2^+, F = 1$ . Note, the beam addressing the  $G = 1$  manifold addresses all three hyperfine manifolds however we define the detuning to be from  $F = 2$ . Additionally, we will leave the optical repumpers on  $v = 1$  and  $v = 2$  at all times for the subsequent data, and the microwaves mixing  $v = 0, X^2\Sigma^+, N = 0^+ \rightarrow v = 0, X^2\Sigma^+, N = 1^-$  will be off as they cause destabilization of

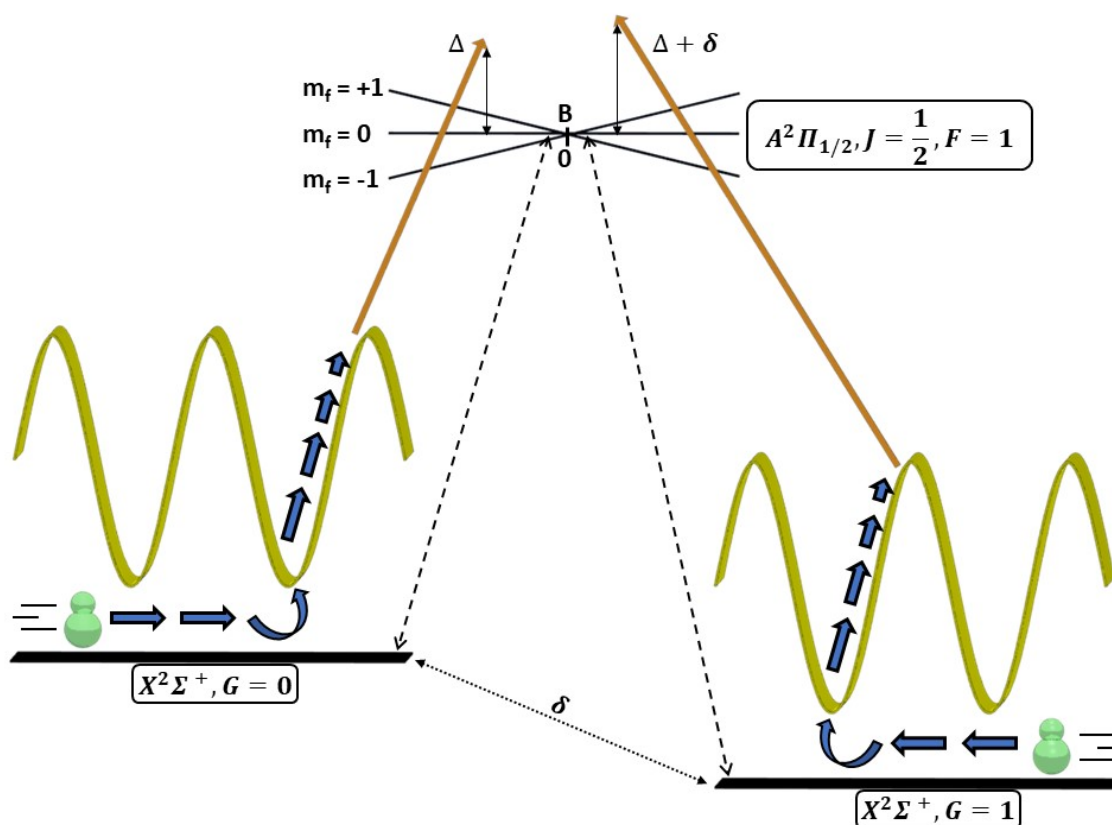


Figure 3.8: In each ground state manifold Sisyphean-like cooling takes place between a dark and bright state due to non-adiabatic coupling due to the motion of the molecules with subsequent relaxation back to the dark state as described in the text. Coupling two ground state manifolds with two different light fields in a  $\lambda$ -type configuration creates a robust dark state when  $\delta = 0$ . Application of a gradient B-field allows for a blue-detuned MOT which will be described in detail in the following chapter.

the dark states due to the transition being dressed and causing subsequent higher temperatures. The configuration of the beams and their propagation into the chamber is discussed in the next chapter.

Diagrams of the relevant couplings and detunings are shown in Fig.3.8 and Fig.3.10 (a). The relevant parameter of interest in this work is of course the temperature of the molecular ensemble. The temperature is measured by TOF (Time-of-Flight) measurements where ballistic expansion of the size of the molecular ensemble is measured after release from the GMC or in other cases the MOT or conservative trap. A linear slope can be fitted to expansion size vs time defined as,

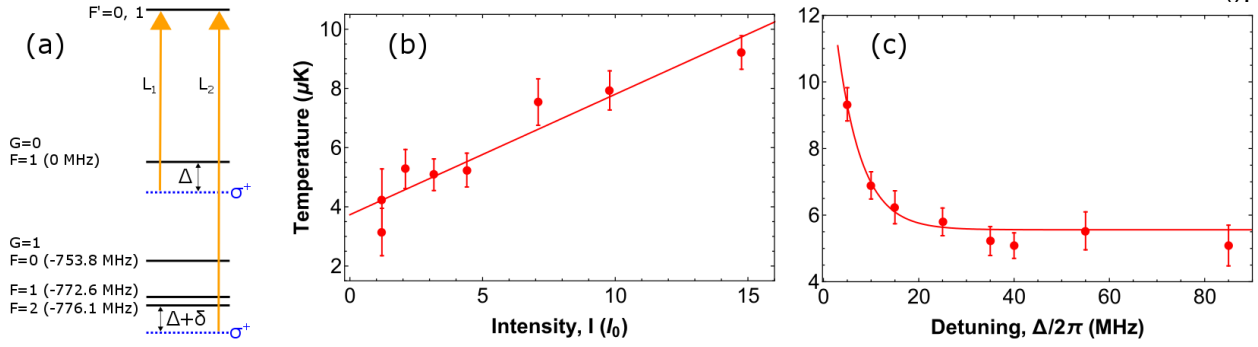


Figure 3.9: (a) Definition of the  $\Delta$  and  $\delta$  for  $\Lambda$ -Enhanced GMC of YO molecules along with an energy diagram of the ground state manifolds. (b) Dependence of temperature vs intensity  $I$  in units of  $I_0$  (single beam saturation intensity for a two-level system) a linear dependence on intensity is seen as expected from theory. Here  $\Delta = 8.3\Gamma$  and  $\delta = 0$ . (c) Dependence of temperature vs  $\Delta$  we see a  $\approx 1/\Delta$  dependence as expected by theory. Here  $I = 3.2I_0$  and  $\delta = 0$ .

$$\sigma^2(t) - \sigma_0^2 = \frac{k_b T t^2}{m}, \quad (3.14)$$

to determine the temperature where  $m$  is the mass of the molecules and  $\sigma^2(t)$  is the size of the ensemble after expansion for a time  $t$ . When we image the molecules we normally apply a short resonant beam of light on the molecules with the DFM beams  $< 500 \mu\text{s}$ , we measure two sizes one in the axial direction which we always define as along gravity and the radial direction in the plane of the crossing MOT beams in the x-y directions. As such, the temperature we quote is always the weighted average of these two directions as  $T_{avg} = T_{radial}^{2/3} T_{axial}^{1/3}$ .

First, we can scan out the intensity and one-Photon detuning vs temperature. We apply the GMC cooling for 10 ms after the DFM MOT and then measure the temperature. The results are shown in Fig.3.10 (b), (c). For plot (b)  $\Delta = 8.3\Gamma$  and  $\delta = 0$  and the intensity is scanned in the six-beam molasses. The units of intensity are given in terms of the two-level saturation intensity  $I_0$  for a single beam defined as  $I_0 = 2.7 \text{ mW/cm}^2$ , and is equally distributed between the two components. We achieve temperatures in this work as low as  $4 \mu\text{K}$ , the coldest laser-cooled ensemble at that time only beaten by our recent results. Here we find a linear dependence on intensity which is what is expected by theory as we recall that the damping coefficient for sub-doppler Sisyphus mechanisms

is independent of intensity at above  $1 I_0$  [21], [25]. However, the scattering rate scales linearly with  $I$  as we recall in Eq.3.2. Therefore using the Einstein relation Eq.3.3 we expect the temperature  $T$  to scale as  $T \propto I$ .

Next for the one-Photon detuning vs temperature in plot (c) we fix  $I = 3.2I_0$  and  $\delta = 0$ . Here we find a dependence of  $1/\Delta$  this is again what is expected from theory. We know the energy removed per Sisyphus cycle is proportional to the ac-Stark shift which goes as  $V_{dip} \propto 1/\Delta$  from Eq.3.12 which is also proportional to the damping coefficient  $\alpha$ . However, the scattering rate goes like  $R_{scat} \propto 1/\Delta^2$  from again Eq.3.2. As such, their ratio from Eq.3.3 predicts the temperature to go as  $T \propto 1/\Delta$ . Due to this we always detune our GMC by around 8 linewidths generally as this dependence on  $\Delta$  becomes fractionally small and is insensitive to  $\Delta$  fluctuations and we get the lowest temperatures.

Next, we can scan out the two-photon detuning  $\delta$  which is a much more interesting parameter compared to the intensity and  $\Delta$ . The results are shown in Fig.3.10 (a) and (b) where (b) is an enlarged scan at around  $\delta = 0$ . In plot (a) far from resonance we maintain strong cooling with temperatures below  $10 \mu\text{K}$  purely from the polarization dark states in each individual ground state manifold. If we study plot (b) at two-photon resonance we see cold temperatures around  $4 \mu\text{K}$  which is what we expect as at  $\delta = 0$  a true dark state formed [67] (Chapter 6). Suppression of the excited state population is created however on the order of  $\pm \frac{\Omega^2}{\Gamma}$  from the resonance detuning. From the given experimental parameters this is on the order of 10s kHz and we do see the temperature remains low on this scale away from  $\delta = 0$ . However, for detunings at  $\pm 100$  kHz we see pronounced heating which is quite striking. Our best reasoning for this is that you have two effects that create dark states. One is from the polarization gradients present in the system which provides the GMC cooling in all the ground state manifolds. The second is from coupling the manifolds in a lambda scheme creating a coherent dark state at  $\delta = 0$ . If we move away from resonance the two-photon Rabi-frequency becomes non-zero and begins to shuffle the population between the ground state manifolds. This has the effect of shortening the ground state coherence lifetime as discussed with polarization gradient cooling leading to a lower damping rate and higher temperatures. When the

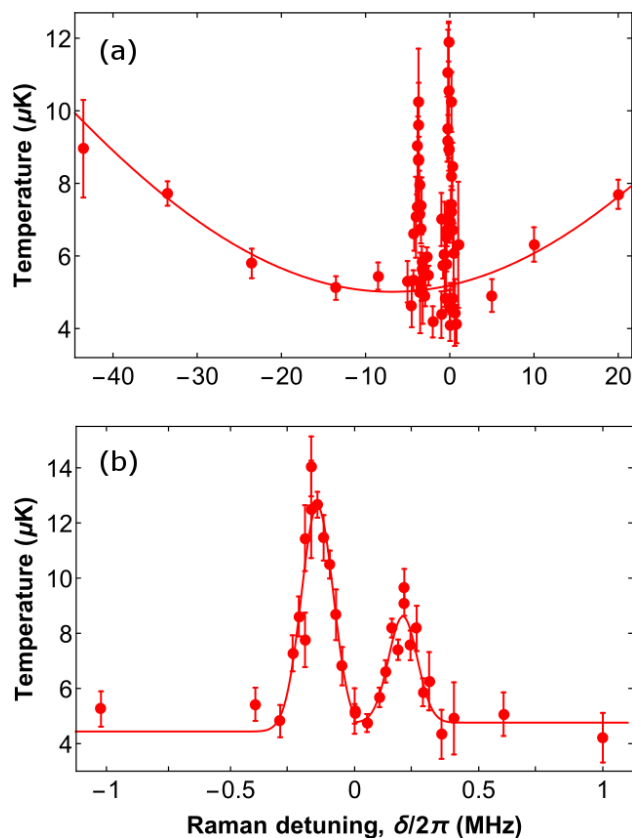


Figure 3.10: (a) and (b) show the dependence of the temperature vs  $\delta$ . (b) is an enlarged scan near  $\delta = 0$  which is two-photon resonance. We can see pronounced heating occurs when  $\delta$  is set just off-resonance due to destabilization of the polarization dark states in each ground state manifold. In these scans  $I = 3.2I_0$  and  $\Delta = 12.5\Gamma$ .

two-photon detuning becomes large however the population piles up into a predominately single ground state manifold  $G = 0$  or  $G = 1$  and the GMC cooling in the manifold becomes robust again leading to colder temperatures.

One thing to note, however, is at two-photon resonance, you would expect a lower temperature even to below a single photon recoil from VSCPT than that just provided by GMC. We did not see it at that time. However, now I am happy to say that after re-zeroing stray fields to better accuracy and redoing all the laser locks in the lab we do reach colder temperatures at  $\delta = 0$  where we achieve robustly 1.5  $\mu\text{K}$  every day in free space cooling which is only 3 photon recoils in temperature. This is shown in Fig.3.11.

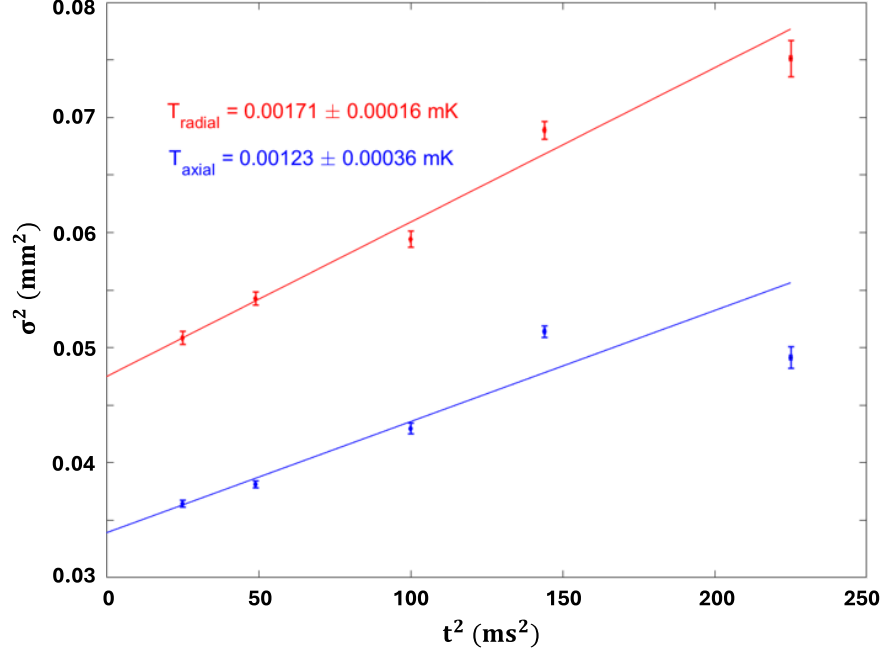


Figure 3.11: Example of daily temperature of  $\Lambda$ -Enhanced GMC of YO as of writing this thesis. The temperature shown is  $T_{avg} = 1.5(2) \mu K$  which is about 3 photon recoils. This represents the coldest sample of a bulk gas of laser-cooled molecules.

Before finishing the discussion on  $\Lambda$ -Enhanced GMC of YO molecules I would like to discuss one more interesting experiment we performed. The experiment applied a static uniform B-field along the z-axis and measured the resulting temperature while fixing the intensity and detunings at  $I = 3.2I_0$ ,  $\Delta = 8.3\Gamma$  and  $\delta = 0$  the results are shown in Fig.3.12. We have some fascinating results. First at zero field, the lowest temperatures are achieved which makes sense as the ground state manifolds are least perturbed. Next, I would like to remind you that since YO has unique ground state coupling due to the fermi contact interaction the  $G = 0$  manifold is magnetic field insensitive below 10 Gauss, and the  $G = 1$  is magnetic field sensitive as shown in Fig.2.17. Turning back to the figure as the B-field is increased to around 0.5 Gauss the ground state manifolds in  $G = 1$  are being remixed by Larmor precession while the  $G = 0$  manifold is stable and coherent. Since the manifolds are coupled in the  $\lambda$ -type configuration the dark states become destabilized and there is a stark increase in temperature. At around 1-4 Gauss we see that the temperature drops and becomes flat

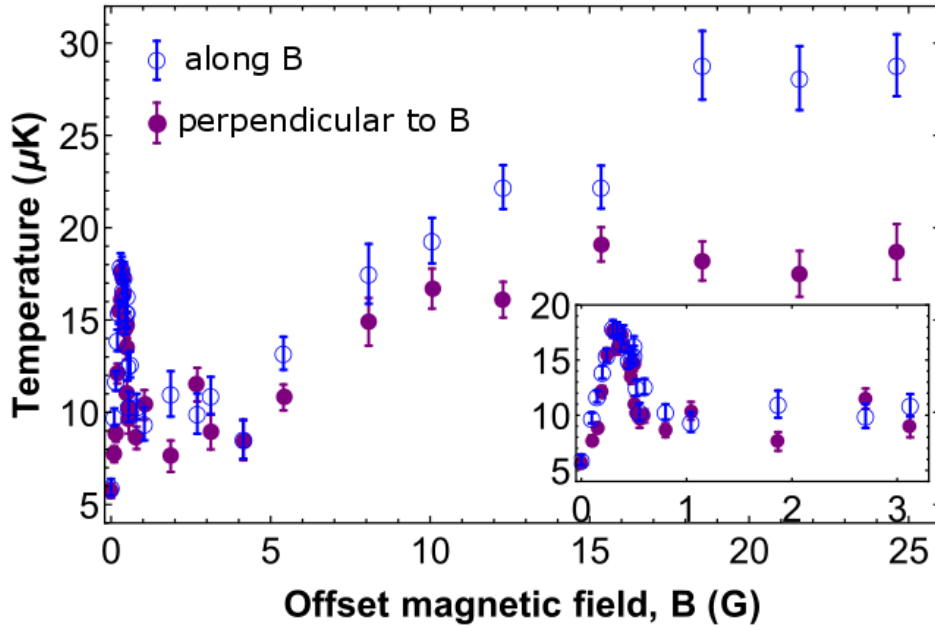


Figure 3.12: Shown is the effect of an applied magnetic field along the z-axis on the  $\Lambda$ -Enhanced GMC in YO molecules. The relevant parameters were held fixed at  $I = 3.2I_0$ ,  $\Delta = 8.3\Gamma$  and  $\delta = 0$ . We see at even large fields of 25 Gauss the average temperature remains at around  $25 \mu\text{K}$  unmatched by any other atomic or molecular species.

again and this is due to all the dark states in  $G = 1$  (no dark states) being remixed and optically pumped into  $G = 0$  which provides strong GMC cooling as it is not perturbed by the magnetic field. In the next region the GMC cooling becomes less effective in  $G = 0$  as at around 10 Gauss there will be an appreciable Larmor frequency mixing the population. However, something striking happens at 15 gauss where the temperature plateaus in both directions. This is because a different Sisyphus mechanism takes over called "MASE" which is the Magnetically-Assisted-Sisyphus-Effect [28].

This is quite remarkable as at 25 Gauss YO molecules remain at temperatures around  $25 \mu\text{K}$ . To give some perspective at fields of around 1 Gauss a typical polarization gradient cooling in an atomic ensemble would be completely ruined. Generally, however, GMC is magnetically insensitive [25] and this is even more so in YO molecules due to its ground-state coupling. This is quite advantageous as we will see for the blue-detuned MOT as the sub-Doppler cooling will not

be perturbed by the applied gradient field.

## Chapter 4

### Magneto-Optical Trapping of YO Molecules

#### 4.1 Theory of Molecular MOTs

MOTs have probably been the most difficult part of the laser-cooling of molecules saga, and it took much effort from many groups before MOTs were achieved. I would say however during my PHD "regular" MOTs have been mostly figured out and a recipe for success has been written. The theory of magneto-optical trapping (MOT) is not unlike that of the analysis we had already performed when discussing optical molasses at the beginning of chapter 3. Indeed when discussing the scattering force in Eq.3.2 I had mentioned that beyond providing a detuning for the Doppler shift which provides a force linearly dependent on the velocity at small velocities, you can add in a detuning term that is dependent on the differential Zeeman shift from the ground to the excited state. Suppose the field applied is a gradient field with a null at zero, such as that provided by two magnetic coils in the anti-Helmholtz configuration, you can give a position-dependent scattering force where the detuning in total would look like  $\Delta_j = \delta_j - \vec{k} \cdot \vec{v} - (g_e M_e - g_j M_j) \mu_B \vec{A}_r \cdot \vec{r} / \hbar$ . Here  $A_r$  is the gradient field and  $r$  is the position from the trap center. The reason we wish to do this is simple, we want a position-dependent force to confine the molecules to a certain region and compress them in size. The damping force is not position-dependent as such the ensemble of atoms or molecules "trapped" in the molasses will simply diffuse out over time. MOTs achieve trapping and cooling with great success and are generally the beginning point of all ultracold atom and molecule experiments after slowing.

We can expand the force on the molecules at small displacements as,

$$\vec{F}_{MOT} \approx -\alpha\vec{v} - \kappa\vec{r} \quad (4.1)$$

where again  $\alpha$  is the damping coefficient and the new term  $\kappa$  is the spring constant and determines the strength of the position-dependent force. We can note that this force looks very familiar as it is just a damped harmonic oscillator, and that is why we write the force in this form. This is advantageous as the position of the molecules has a quadratic degree of freedom and this allows us to use the equipartition theorem  $\kappa\sigma_i^2 = m\omega_i^2\sigma_i^2 = k_B T_i$ , where  $T_i$  is the temperature,  $\omega_i$  is the trap frequency,  $m$  is the mass of YO and  $i = x, y, z$  to relate the temperature and trap frequencies at equilibrium. A time of flight measurement as we recall in Eq.3.14 measures both the temperature and the size at  $t = 0$  (you can of course also use the in-situ size) and a single time of flight measurement can determine  $\kappa$ . Additionally, using the temperature and Eq.3.3 along with a scattering rate measurement you can determine  $\alpha$ . If you know  $\alpha$  and  $\kappa$  then you have a good understanding of the MOT dynamics of your system from Eq.4.1.

So why are molecular MOTs difficult to implement? It has to go back to the fact that we are using Type-II transitions to close the rotational ladder, and the problem is the same as that we discussed when slowing. If we apply a gradient field and red-detuned beams with counter-propagating circularly polarized beams as is typical in MOTs we will immediately optically pump into the opposite stretched state. This is shown in Fig.4.1. The first solution to this problem which is still widely used today is the so-called "RF-MOT". Where both the polarization is chopped similar to the solution we have for slowing, and the B-field gradient is swapped in sign synchronously at a rate comparable to or faster than the optical pumping time. This was first demonstrated in our experiment in 2D on a molecular beam [36]. Subsequently, this technique was applied to 3D for most molecular species [77], [53], [3] and [20]. This technique works great and captures a large number of molecules at temperatures compared to that of atomic MOTs. However, a more elegant solution exists that provides colder temperatures and in YO, more molecules.

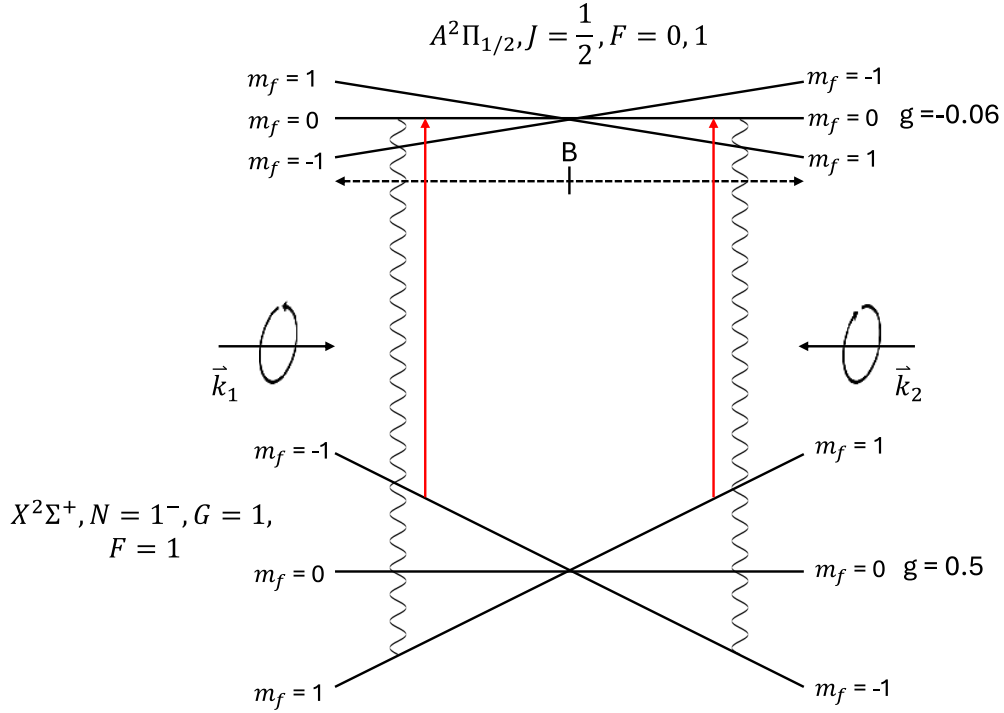


Figure 4.1: Shown is a type-II MOT configuration. With the application of a gradient B-field and red-detuned beams, the molecules will be optically pumped into the opposite stretched state with a few photon scatters.

## 4.2 Dual-Frequency MOT of YO

That solution is to use a "Dual-frequency MOT" where we apply simultaneous red and blue-detuned laser frequencies on both of the stretched states in Fig.4.1. This was first proposed by Mike Tarbutt's group [73]. Now adding blue-detuned components may raise some alarms as we know that anytime a photon is scattered it will cause Doppler heating. This is true, however, stepping back we can see that in a type-II optical molasses, we have a Doppler mechanism and a Sisyphus mechanism from GMC. These mechanisms have opposite signs, so for any detuning, we will have competing cooling and heating mechanisms which was present in the case when we discussed the results of sub-Doppler cooling in the previous chapter. For reference, a table is shown in Table.4.1 displaying these mechanisms. Note, however, that the cooling and heating written in the table are only true for molecules that have a velocity around or below a critical  $v_c \approx 1$  m/s [25] which is true

Type-II Cooling Mechanisms		
$v_c \approx 1$ m/s	Doppler	Sub-Doppler
Red-detuned	Cooling	Heating
Blue-detuned	Heating	Cooling

Table 4.1: Cooling mechanisms vs detuning in type two systems. At all detunings, there is one heating and cooling mechanism. The relative heating and cooling is true for molecules with velocities less than a critical velocity  $v_c \approx 1$  m/s [25].

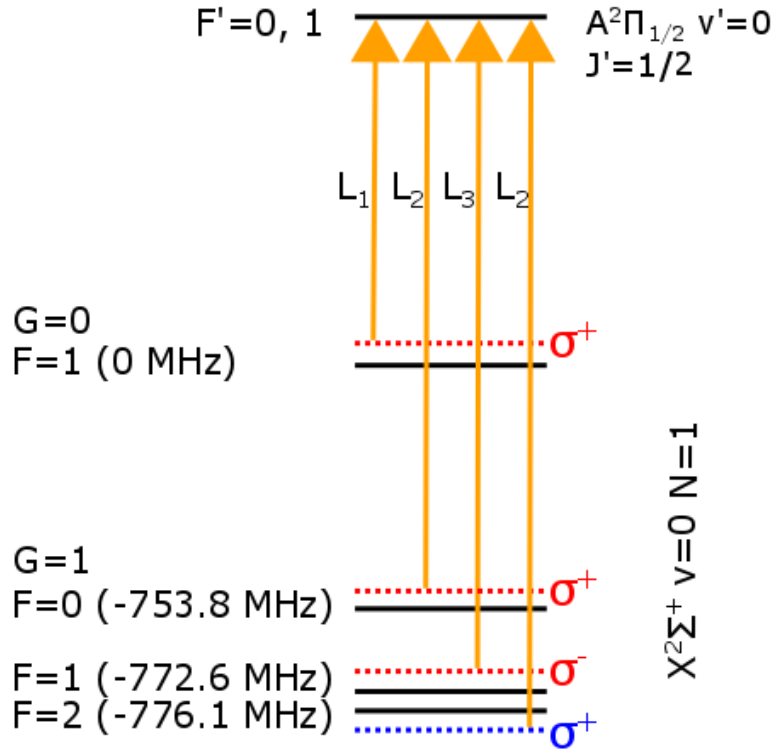


Figure 4.2: Shown are the optimal polarizations and detunings of the DFM in YO. The detunings for L1, L2 and L3 are (-5.8 MHz), (-9 MHz, +2.6 MHz) and (-5.8 MHz) respectively.

for our Dual-Frequency MOT (DFM).

This creates an interesting physical system which is a balance of competing cooling and heating mechanisms. Predominantly we want mostly Doppler cooling as an optical molasses relying on Doppler cooling has a higher capture velocity than that of a sub-Doppler mechanism [21], and we want to capture as many molecules as possible after slowing. The rough capture velocity of the DFM is shown in the previous plot Fig.3.2 with a capture velocity of 3.5 m/s. However, if the

blue-detuned components are set correctly we can achieve lower temperatures and longer lifetimes in the MOT as the scattering rate will be lower.

To perform the DFM we need to set the correct polarizations for each manifold in the ground state. The correct polarizations are detailed in [72] and if you want to understand molecular MOTs you should read this paper. In short, for a given excited state g-factor sign, gradient field sign, upper and lower angular momentum quantum numbers, and detuning a particular polarization needs to be set on each ground state manifold. The correct polarizations and detunings for YO are shown in Fig.4.2. Our work on the DFM is briefly discussed and published in [27]. The number of beams in the DFM is three and are labeled L1, L2, and L3. Beam L1 is set by the detuning of the laser. Beams L2 is generated by dual driving a high-frequency Brimrose AOM. Beam L3 is also generated with a high-frequency Brimrose AOM and is made separately as this beam has opposite polarization to the other beams. The AOM part numbers are either TEF-767 or GPM-800 corresponding to either tellurium or gallium phosphate (I prefer gallium as it has a higher damage threshold at 614 nm). The detunings for L1, L2, and L3 are (-5.8 MHz), (-9 MHz, +2.6 MHz), and (-5.8 MHz) respectively. The optimal intensity of the beams is set to  $I = 1.4I_0$ , where  $I_0 = 2.7$  mW/cm<sup>2</sup>, and is equally distributed to the four components.

The beams are combined on a PBS and sent through a PM-633 optical fiber for mode cleaning. The beams are then launched through an adjustable lens and hit a half and quarter wave-plate pair to create circular polarization. The beams then enter the chamber as shown in Fig.3.5, and are retroreflected with a quarter wave-plate on the last pass. To be more precise, there is a set of quarter wave-plates on every arm on the MOT beams before and after leaving the chamber. This is to ensure the beams are not polarized during reflection off the mirrors and to minimize any birefringence during propagation. Optimized molecular MOTs and GMC are highly sensitive to the polarization being set as pure as possible. Additionally, since the beams are recycled through the vacuum chamber, when they propagate all the way through and back the loss of power is  $\approx 20\%$ . To compensate for this the beams are gently focused using the adjustable lens after the fiber to balance the intensity. The GMC and the MOTs are again very sensitive to this focus and it needs

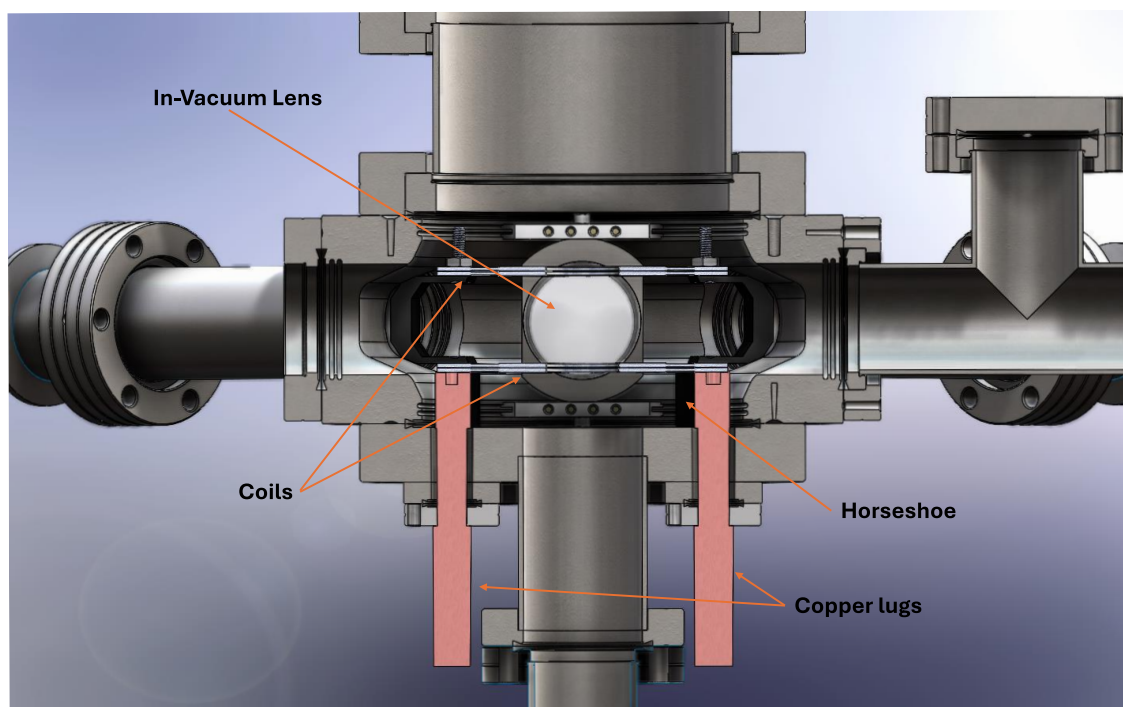


Figure 4.3: Shown are the in-vac coils for the gradient field as described in the text. Additionally, the in-vac objective lens is shown which allows for efficient collection of the molecule fluorescence for imaging.

to be set correctly. This can be done by optimizing the temperature in the GMC and the shape of the MOTs. We also send in  $v_1$  and  $v_2$  optical repumper light through the MOT beams through the use of dichroic mirrors to provide additional repumping for the MOTs. We leave the  $v_1, v_2$  N2, and N3 slowing beams on and they propagate down the slowing axis for both more vibrational repumping and rotational repumping. The microwave fields are left sweeping as discussed earlier in Fig.2.15.

The gradient field is created with two vacuum coils in the anti-Helmholtz configuration. Each coil has two stacked aluminum nitride PCBs due to their favorable thermal properties with circular copper traces. The separation of the coils is 2.97 cm and are heatsinked to a copper horseshoe with copper lugs that extend out of the vacuum. These can be actively water-cooled for heat dissipation of the coils. However, throughout my entire PHD, this has not been required for the applied fields I have used. A CAD model of the coils in the vacuum chamber is shown in Fig.4.3. The coils

are connected in parallel. This was originally done to limit the electric field created between the coils when a current is applied. However, due to a machining error, the coil null field was offset from the paraxial condition of the optical beams. As such, compensation resistors were added on one leg to push the null field down to the center of the MOT/GMC beams. We know from our earlier discussion on the  $A'^2\Delta_{3/2}, J = 3/2^\pm$  state that very small fields can mix the parity doublet as seen in Fig.2.14. Now since the coil resistances are unbalanced applying fields larger than 15 G/cm significantly mixes this state caused by the electric field between the coils. This limits our overall maximum field gradient to be around 14 G/cm or significant loss is seen through  $v = 1, 2, X^2\Sigma^+, N = 3^-$ . This is an extremely trivial problem that needs to be fixed or repumping out of  $v = 1, 2, N = 3^-$  needs to be applied. If it was fixed we could create MOTs on YO with densities that would be incomparable to other molecular species. I should say however, that the maximum field gradient that I have had the coils is above 100 G/cm during testing which is more than enough for a magnetic trap of YO in the absolute ground state which will be discussed in the last chapter in more detail.

Getting to the results of the DFM a typical image of the DFM is shown on the left-hand side of the Fig.4.4. The image is taken by collecting 13 ms of MOT fluorescence with an Andor IXON 888 EMCCD. From this, we can determine the number of molecules in the MOT. As discussed earlier using equipartition and using TOF to determine the temperature, we can determine the spring constant and the PSD. We get values of around 200,000 molecules at a temperature of 1.8 mK a spring constant of  $\kappa_z = 1.4 \times 10^{-20}$  N/m and a PSD  $\approx 10^{-13}$  for a good MOT. If we perform a scattering rate measurement as shown on the right side of the figure by turning off the v1 optical repumper, we can determine the scattering rate and the damping rate  $\alpha/m$  using the Frank-Condon factors and Eq.3.3. We achieve the values of  $R_{scat} = 369$  ( $\times 10^3$   $s^{-1}$ ) and  $\alpha/m = 34.7$   $s^{-1}$ . The spring constant and damping rate are lower than what you typically expect in an atomic MOT, but due to the nature of all the ground state manifolds vs the excited state manifolds (recall Eq.3.2) we expect the scattering rate to be lower creating a lower scattering force. I want to say that this MOT was essentially optimized in-situ to something that provided the largest molecule

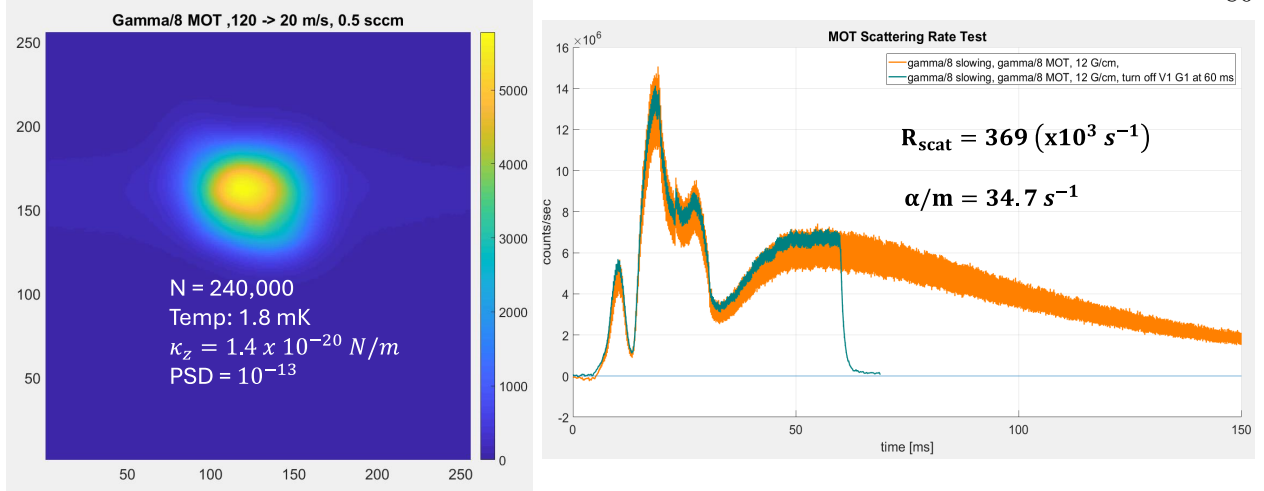


Figure 4.4: Shown is an image of the DFM on the left and a time trace of the slowing, loading and DFM on the right (before microwave sweeping was implemented). From the image on the left, we can discern the molecule number and from TOF we can get the temperature, spring constant, and the Phase Space Density (PSD). From the right trace turning off the v1 optical repump beam, we can discern the scattering rate using the Frank-Condon factors, and the corresponding damping rate  $\alpha/m$  using Eq.3.3.

number and temperatures around 2 mK. Therefore, many optimizations can be done, and this is even suggested by full-rate equation models. Since the parameter space is quite large this could be a good candidate for reinforcement learning in the future and should be done to optimize this MOT in the future. Again, with optimizations with the slowing and this MOT, I would not be surprised if a factor of 10 gain in the molecule could be achieved. This could be done by moving the coils out of the vacuum chamber to allow larger MOT beams and repumping the v1 population through the transition  $v = 1, X^2\Sigma^+, N = 1^- \rightarrow v = 0, B^2\Sigma^+, N = 0^+$ . Again something of this nature will need to be done for future evaporation studies.

### 4.3 Blue-Detuned MOT

We have come to an interesting possibility for a unique MOT. What if we could completely rely on GMC cooling while in the presence of a gradient field? Even though this would create MOTs with smaller spring constants than that of a DFM or RF-MOT we could drastically reduce the size

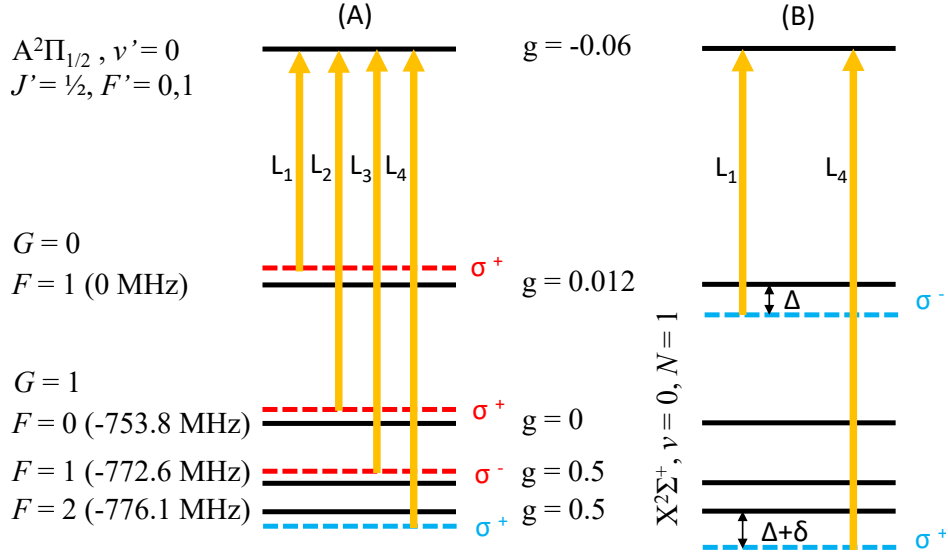


Figure 4.5: (A) DFM configuration including polarizations and detunings addressing each manifold. (B) BDM configuration is created by shuttering  $X^2\Sigma^+, N = 1^-, [G = 0, F = 1], [G = 1, F = 0, 1]$  and turning on a new beam on  $X^2\Sigma^+, N = 1^-, G = 0, F = 1$  with opposite polarization and detuning.

of the MOT due to the equipartition theorem from the significantly lower temperatures that could be achieved. This is important as it allows better mode matching to the molecular ensemble with optical trapping beams which will be discussed in the next chapter. This type of MOT is called a Blue-Detuned MOT (BDM) and was proposed [25] and demonstrated in Rb atoms [38] primarily for use in laser-cooled molecules.

The first molecular species to demonstrate this MOT was in this experiment in YO with the published work here [11]. This work was part of the middle to latter part of my PHD where I led the development in the lab, and represented the first sub-Doppler molecular MOT. I believe the entire field of laser-cooled molecules was converging to a similar route to further enhance the densities that could be made in optical traps. As such, after our first demonstration in molecules BDMs were created in all the other laser-cooled species [39],[45], and [34].

The basic physical mechanism has already been shown and discussed in Fig.3.8. Again, from our results in Fig.3.12 we expect any present magnetic field to have a small effect on the GMC cooling. However, we have arrived at an interesting juxtaposition. For efficient sub-Doppler cooling,

particularly GMC we want the lowest possible excited state population  $\rho_{ee}$  to create coherent dark states as we discussed in the previous chapter. However, the spring force in a MOT relies on the scattering force, not the dipole force and we need an appreciable excited state population to exist at all times to have a spring constant. These two competing mechanisms create a knife edge of optimized parameters which we will discuss below to create this MOT in YO molecules.

First, the technical implementation of the BDM is shown in Fig.4.5. The DFM configuration that we discussed in the previous section is shown on the left in (A). The relative energy level splitting is also shown with the approximated g-factors at fields up to around  $\approx 10$  G. To create the BDM the components on  $X^2\Sigma^+, N = 1^-, [G = 0, F = 1], [G = 1, F = 0, 1]$  are turned off by physical shutters and AOMs. Another laser tone addressing  $X^2\Sigma^+, N = 1^-, G = 0, F = 1$  is then turned on with opposite polarization and blue-detuning with another AOM. This gives two detunings exactly similar to the setup we use with GMC except with the opposite polarization on  $X^2\Sigma^+, N = 1^-, G = 0, F = 1$ . This setup is shown in (B).

Like GMC there are only three parameters that can be scanned intensity  $I$ , the one-photon detuning  $\Delta$ , and the two-photon detuning  $\delta$ . To characterize the MOT following Eq.4.1 we want to determine the spring constant  $\kappa$  and damping coefficient  $\alpha$ . Following the methodology in Fig.4.4, if we measure the temperature and the scattering rate at each point for each parameter scanned we can determine both  $\kappa$  and  $\alpha$  and the subsequent MOT dynamics.

First, we scan the intensity shown in Fig.4.6. Here we fix the magnetic field gradient to 4 G/cm,  $\Delta = 0.44 \Gamma$  and  $\delta/2\pi = -264$  kHz. The axial direction is set by the gradient field which is stronger by a factor of 2 compared to the radial in the anti-Helmholtz configuration. First looking at panel (a) we achieve temperatures of around  $\approx 30 \mu\text{K}$  which is below the Doppler temperature by over a factor of 3. Below 1  $I_{sat}$  we see the temperature rise as the cooling and trapping force goes to zero as we would expect. At 1  $I_{sat}$  and above we see the temperature reach a minimum value and increase linearly vs intensity. This is exactly what we would expect from earlier discussions when discussing GMC. We can see this actually from panel (c) where the damping coefficient peaks at around 1-2  $I_{sat}$  then plateaus which is predicted for sub-Doppler cooling mechanisms [25],[21].

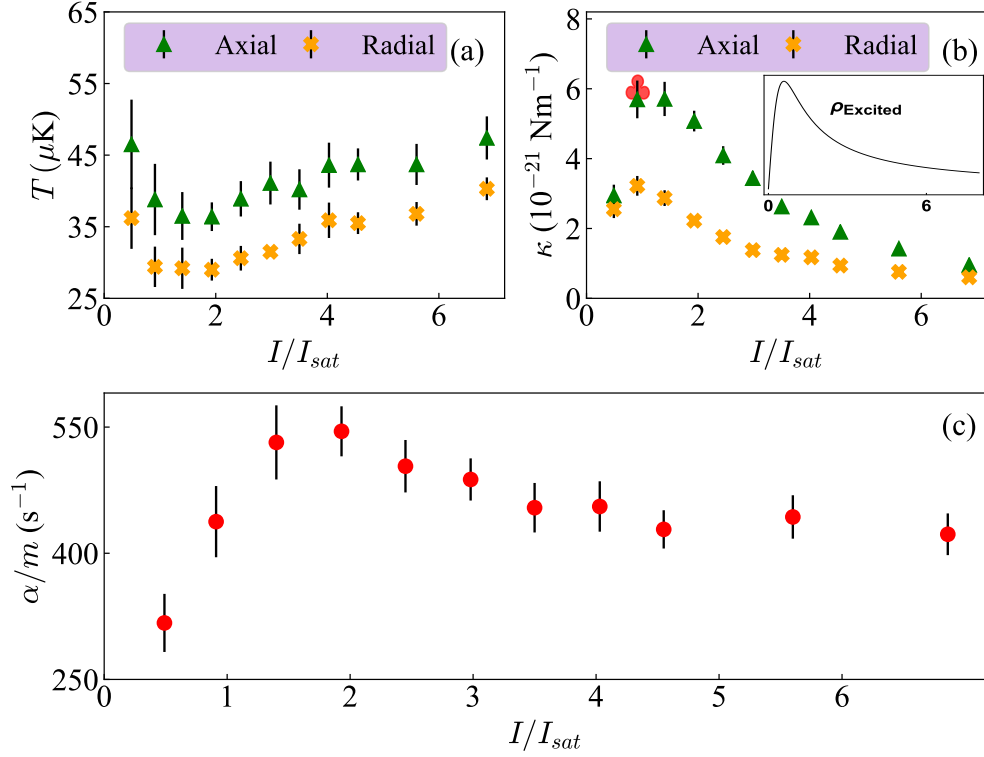


Figure 4.6: Shown is the Variation of the (a) temperature ( $T$ ), (b) spring constant ( $\kappa$ ), and (c) damping rate ( $\alpha/m$ ) with intensity ( $I$ ) of each beam which are set with equal intensity, with a magnetic field gradient of 4 G/cm,  $\Delta = 0.44 \Gamma$  and  $\delta/2\pi = -264$  kHz.

If we again use Eq.3.3, we predict a linear increase in  $T$  as the scattering rate increases linearly with intensity and  $\alpha$  is fixed. The spring constant is more interesting as we see a strong peak around  $1 I_{sat}$  then a slow decrease as the intensity increases. The red clover represents a full rate simulation of the spring constant in the z-direction using Eq.3.2. We find very good agreement with the measured results. The error on the rate equation is not shown as it is quite large do to the excited state hyperfine splitting in  $A^2\Pi_{1/2}, J = 1/2^+, F = 0, 1$  being unresolved within the linewidth. The inset is the result of a three-level system using the optical-Bloch-equations and plots  $\rho_{ee}$ . We find good qualitative agreement with the data. The falling off at higher intensity can be understood as the two photon-Rabi frequency becoming large enough that the excited state population starts to become adiabatically eliminated since  $\delta \neq 0$ , with the population spending the majority of the time shuffling between the  $G=0$  and  $G=1$  manifolds through coherent stimulated

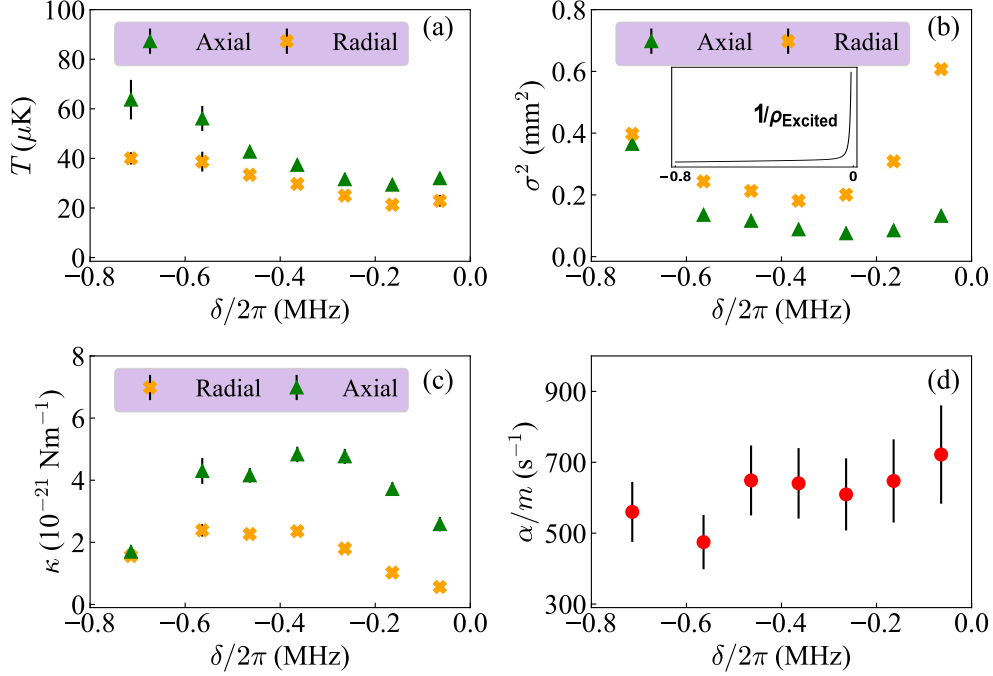


Figure 4.7: Shown is the variation of (a) temperature ( $T$ ), (b) quadrature size ( $\sigma^2$ ), (c) spring constant ( $\kappa$ ), and (d) damping rate ( $\alpha/m$ ) in the blue MOT with differential detuning ( $\delta$ ), with  $\Delta = 0.44 \Gamma$  and  $I = 1.93 I_{\text{sat}}$  and maximum magnetic field gradient of 4 G/cm.

emission.

Next, we discuss the results from scanning out  $\delta$  which is a very interesting parameter as we can effectively turn off and on a strong coherence by changing it in the  $\Lambda$ -enhanced GMC scheme. Here we fix  $\Delta = 0.44 \Gamma$  and  $I = 1.93 I_{\text{sat}}$  with a maximum magnetic field gradient of 4 G/cm. First looking at panels Fig.4.7 (a) and (d) we see that the temperature decreases and the damping rate increases weakly linearly as  $\delta \rightarrow 0$  as we expect as we make a coherent dark state. Where the lowest temperatures and highest damping rate are achieved at  $\delta \approx 0$ . However, looking at panels (b) and (c) which show the size of the BDM and the spring constant we see dramatic behavior. At  $\delta = 0$ , we see the spring constant goes to zero and size approaches that of the DFM as the excited state population  $\rho_{ee}$  goes to zero. However, if we detune  $\delta \approx -300$  kHz we see a large increase in the spring constant and a compression of the size. This is a beautiful consequence of the physical system by tuning one laser tone by several hundred kHz we can transition from pure GMC to a BDM while

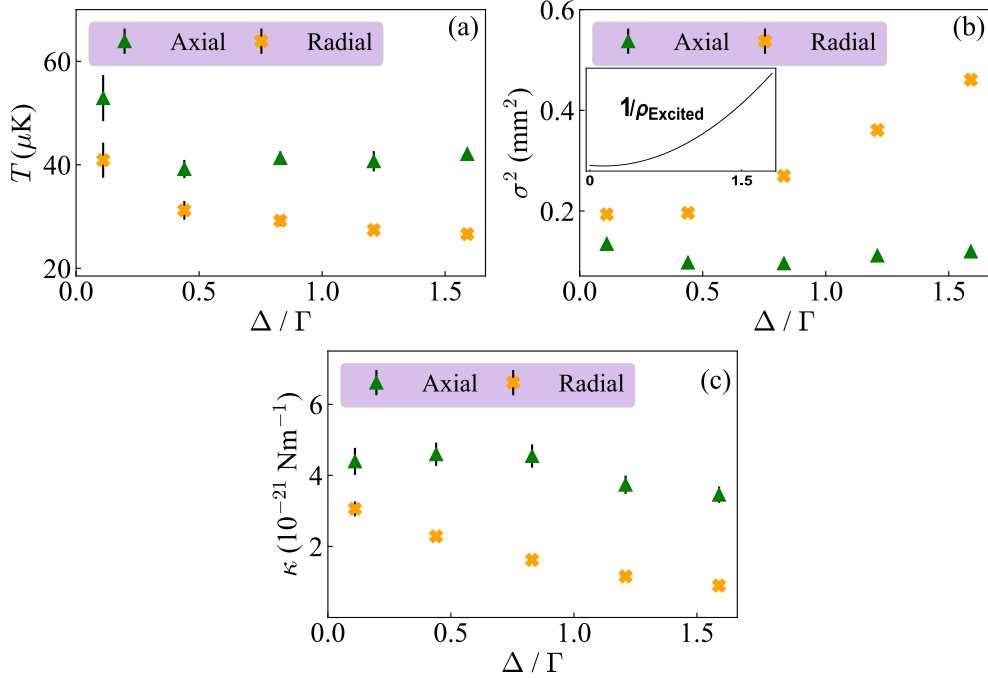


Figure 4.8: Shown is the variation of (a) temperature ( $T$ ), (b) quadrature size ( $\sigma^2$ ), and (c) spring constant ( $\kappa$ ) on one-photon detuning ( $\Delta$ ), with a magnetic field gradient of 4 G/cm,  $\delta/2\pi = -264$  kHz and  $I = 1.93 I_{\text{sat}}$ .

fixing all other parameters. As you would expect that there is a deep physical connection between the strong sub-Doppler GMC and the magneto-optical trapping mechanism. This system allows you to tune the relative magnitude of the dipole force and the scattering force against each other to get completely different light-matter interactions by tuning a single laser over a sharp resonance ( $\delta \ll \Gamma$ ). This is the only system I know of that allows for such tight control and separation of the relative trapping and cooling mechanisms. The inset on the size panel is the result of a three-level optical-Bloch-equation solution. We see we get could qualitative agreement with the model with the data at near  $\delta = 0$ . Away from two-photon resonance we that models begin to disagree, but this is due to the triplet of hyperfine manifolds in  $G = 1$  not being accounted for.

Last we discuss the results from scanning out the one photon detuning  $\Delta$ . To be frank this parameter is not incredibly interesting, but it still needs to be optimized. We see from panel Fig.4.8 (a) that over a large range of detuning from  $(0.5 - 1) \Gamma$  the temperature is flat and the

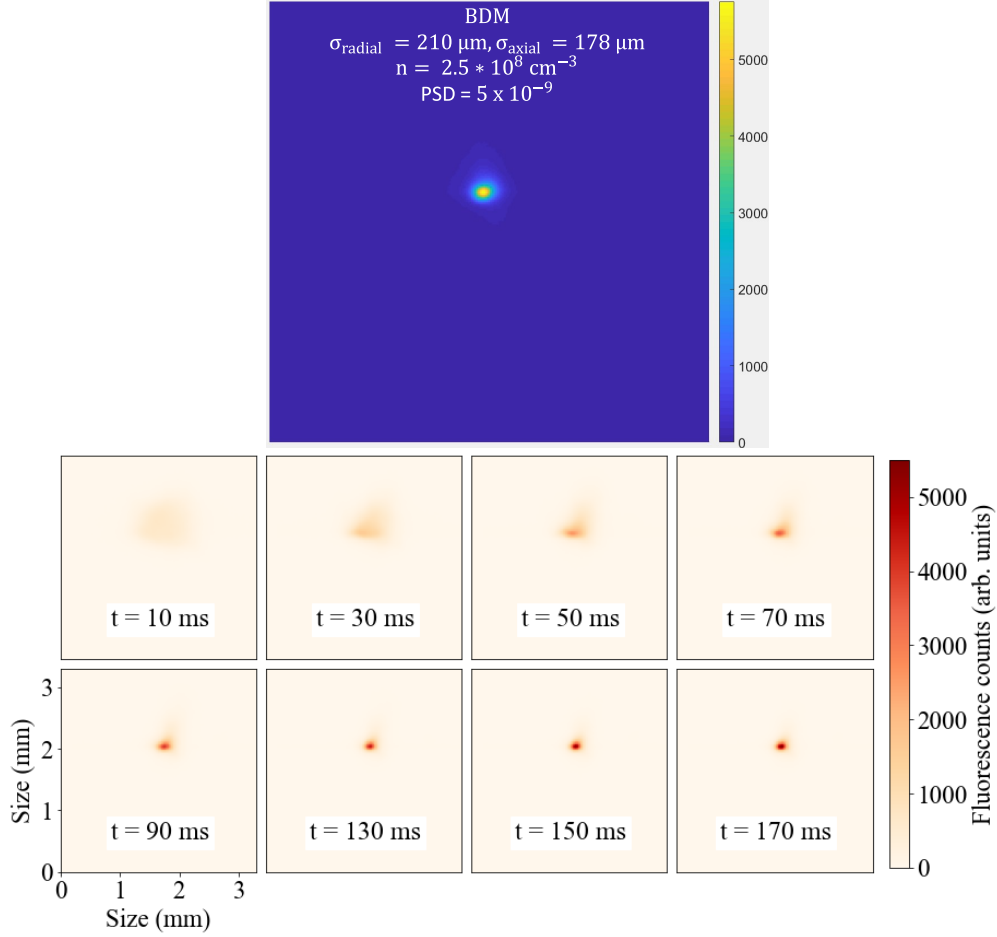


Figure 4.9: Top: In-situ image of the BDM. After 200 ms we achieve a size of  $\approx 200 \mu\text{m}$  in the axial and radial directions with a corresponding Phase-Space-Density of  $5 \times 10^{-9}$  the highest of any molecular MOT. Bottom: Compression of the molecular cloud vs. time.

spring constant is approximately flat in panel (c). We see however that as  $\Delta$  increases the size and spring constant increase and decrease. This is exactly what you would expect as the excited state population decreases like  $\rho_{ee} \approx \Delta^{-2}$  as you can see from Eq.3.2. The inset is again a solution to the Bloch-equations and we find good qualitative agreement with the measured results. For  $\Delta$  it is convenient that the detuning is not very sensitive on the order of several MHz as if the laser lock drifts (which it should not!) it has minimal impact experimentally.

The results of optimization are summarized in Fig.4.9. Here we achieve a BDM with a in-situ size of  $\approx 200 \mu\text{m}$  in the axial and radial directions and a record PSD of  $5 \times 10^{-9}$ . The optimal

BDM sequence used in these images is to ramp the field gradient from 2-14 G/cm over 200 ms. This provides the highest density and the longest lifetime of the MOT. You can see that the compression time of the MOT is quite long around 200 ms due to the small spring constants achieved at these low fields. A new proposal however using a conveyor belt type mechanism has been proposed and demonstrated that should enhance the spring constant in the BDM and is applicable to YO [34]. I would like to state that the advent of the BDMs has changed the field drastically, and is directly responsible for the collision results that will be discussed in chapter 6..

## Chapter 5

### Conservative Trapping of YO Molecules

The work on conservative trapping of YO molecules was performed after sub-Doppler cooling and also after the BDM for collisional studies described in Chapter 6. After the work on sub-Doppler cooling the most senior people in the lab wanted to see if they could make a conservative trap on based the narrow-line transition as we had already had a TA in the lab to create modest amounts of power. However, this did not work out well due to the broad ASE pedestal from the TA causing unfavorable photon scattering. As such, while that was being tried I made optical setups based on high-intensity coherent 1064 nm light which worked immediately as the light is much further detuned and has a much narrower spectrum. The works with conservative trapping can be found here [81] and [12].

We have already discussed the theory of optical trapping in Chapter 3 while discussing the dipole potential. In particular, we stated that if we have transitions with good polarizability and we make the potential spatially varying either by focusing a laser beam or interfering counter-propagating beams with the same polarization, we could conservatively trap the molecules at the points of highest intensity by Eq.3.10. However, like every interaction with light we have discussed there are two forces, the scattering and dipole force. I want to note that magnetic trapping is also a viable route in YO as it is an open shell molecule and has  $1 \mu_B$  sitting in the ground state. However, unlike optical traps that trap all internal spin states, a magnetic trap only traps the low-field seeking states which means the molecules need to be state-prepared. This was not done on YO until the recent work on collisions [12].

In the case of conservative optical trapping, we want the dipole force to be dominant and the scattering force to be as small as possible. The reason is two-fold, first scattering photons will cause heating. Additionally, in molecules, the trapping light can connect the ground state rotational manifolds to many different states through both one-photon and two-photon transitions through excited states so minimizing scattering is paramount. To get the right balance between the forces we note that the scattering force and the dipole force scale like  $F_{scat} \propto \frac{I}{\Delta^2}$  and  $F_{dip} \propto \frac{I}{\Delta}$ . Therefore if we use far red-detuned light from the transitions with high polarizability and with appreciably high intensity we can create a dipole potential deep enough relative to the average kinetic energy of the molecular ensemble, with scattering rates well below  $1 \text{ s}^{-1}$ . This is the principle of FORT (Far Off Resonance Traps).

The total polarizability of YO is shown in Fig.5.1 including the 4 lowest electronic states  $A^2\Pi_{1/2}$ ,  $A^2\Pi_{3/2}$ ,  $B^2\Sigma^+$  and  $A'^2\Delta_{3/2}$  vs. detuning in wavelength (nm) using Eq.3.10. Here a laser beam with 30 W of power and a beam waist of  $100 \mu\text{m}$  is assumed. The black dashed lines represent the position of the transitions and the blue dashed line at 1064 nm. Here we plot the vertical axis in terms of the trap depth of the dipole potential (positive is trapping) in  $\mu\text{K}$ . Experimentally it gives an easy-to-understand trapping force relative to the thermal kinetic energy of the molecules. We see that predominantly most of the trapping comes from the  $A^2\Pi_{1/2}$  and  $A^2\Pi_{3/2}$  states as we would expect as they have the largest linewidths. With the given parameters and using 1064 nm light we would achieve a trap depth of  $62 \mu\text{K}$ . The rule of thumb is that the average temperature of the ensemble over the trap depth should range from 8-10 and is known as the  $\eta = \frac{k_b T}{V_{dip}}$  parameter.

Beyond the trap depth, the trap frequencies are important to quantify the optical trap's strength. For an ODT (focused dipole trap) and XODT (Crossed dipole trap), these frequencies are typically around  $\approx 100 \text{ Hz}$  or lower for typical ultracold or near ultracold experiments. In an optical lattice in 1D, the radial frequencies are also around  $\approx 100 \text{ Hz}$ , and the axial frequencies typically range from 10s to 100s of kHz. These large axial frequencies are great for holding your ensemble against gravity with weak trapping light and the large frequencies are good for resolved side-band cooling as typically found in alkaline earth atoms.

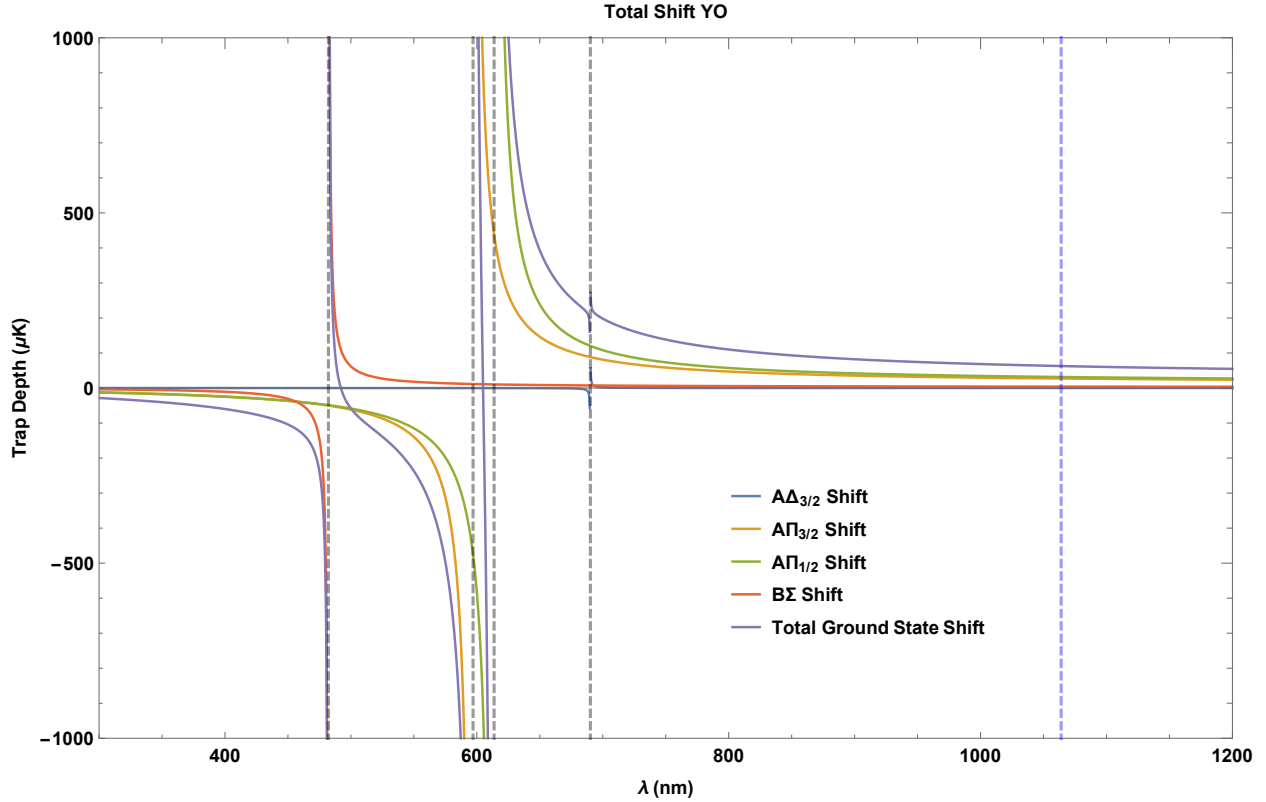


Figure 5.1: Total ac-Stark shift of the ground state in YO which includes  $A^2\Pi_{1/2}$ ,  $A^2\Pi_{3/2}$ ,  $B^2\Sigma^+$  and  $A'^2\Delta_{3/2}$  vs. detuning in wavelength (nm). The position of the transitions is shown with the dashed black lines and at 1064 nm with the blue dashed line. Here a 30 W laser beam is assumed with a beam waist of 100  $\mu\text{m}$ . A positive value on the vertical axis corresponds to trapping.

There are three ways to determine the trap frequencies. If the frequencies are low you can apply a push beam on the ensemble while in the trap and measure the position of the ensemble vs time with a CCD. You will see coherent damped oscillations with the oscillation frequency equal to the trap frequency in that direction. In this experiment, we do not apply such methods as the molecules are not quite in the ultracold regime  $< 1 \mu\text{K}$  which allows for weak traps. The other two methodologies are to induce either pointing heating or intensity heating. Pointing heating is easy as you shake the trap pointing with a piezo mirror and look at the loss of molecules from the trap. Parametric heating is also quite easy as you modulate the intensity of the trap and at twice the oscillation frequency of interest, you will see loss from the trap. Examples of both methodologies are shown in Fig.5.2. For more information on the physical intuition of these processes, I suggest

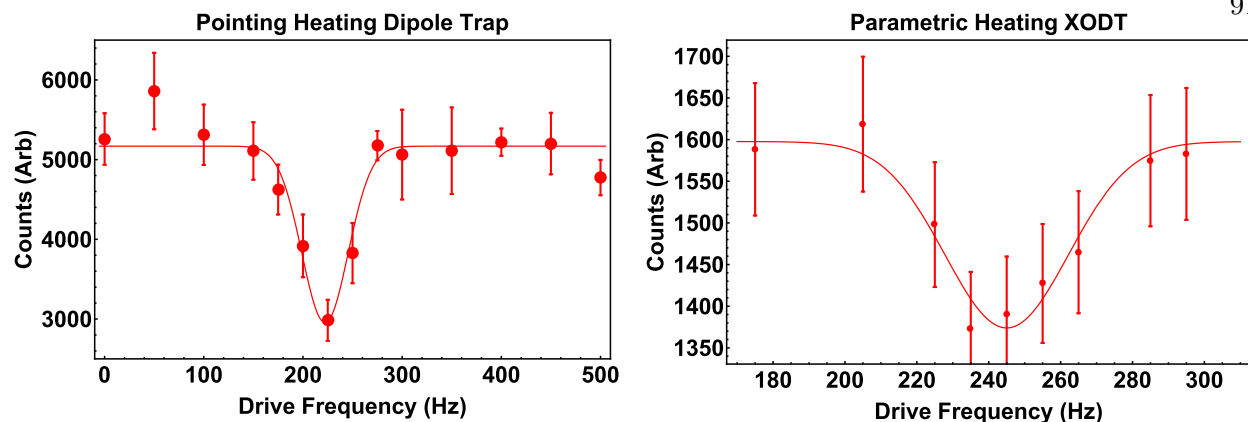


Figure 5.2: Examples of pointing heating and parametric heating to determine the trap frequencies of conservative optical traps of YO molecules. For pointing heating, the loss occurs at the trap frequency and can be achieved by shaking the trap pointing with a piezo mirror. For parametric heating, loss occurs at twice the trap frequency and is achieved by modulating the intensity of the trap light.

[60] as I will not discuss them here.

## 5.1 Technical Implementation of 1064 nm Systems

In this section, I will concentrate on the 1064 nm systems that make up the conservative trapping light in the experiment. The 1064 nm setup for both the optical lattice and XODT consists of a seed laser and two fiber amplifiers. The seed laser is a Coherent Mephisto NPRO ring laser. This laser is extremely "quiet" and provides a free-running linewidth of 3 kHz. Additionally, the laser has a noise-eater on it that provides an extremely low and flat Relative-Intensity-Noise (RIN) of -150 dBc/Hz from near DC to 2.5 MHz. This laser provides an extremely stable and low noise system that is then coherently amplified by two fiber lasers which I will detail.

The first fiber amplifier is a Nufern 50 W 1064 fiber amplifier, which I set up in the experiment. This amplifier has some polarization stability sensitivity and was a backup for Jun's labs just in case people were in dire straits. This laser is seeded with 15 mW of power from the Mephisto. The output laser polarization likes to drift, and is very sensitive to any strain induced in the output fiber. Therefore, the output fiber is rigidly attached to the laser enclosure and the fiber should

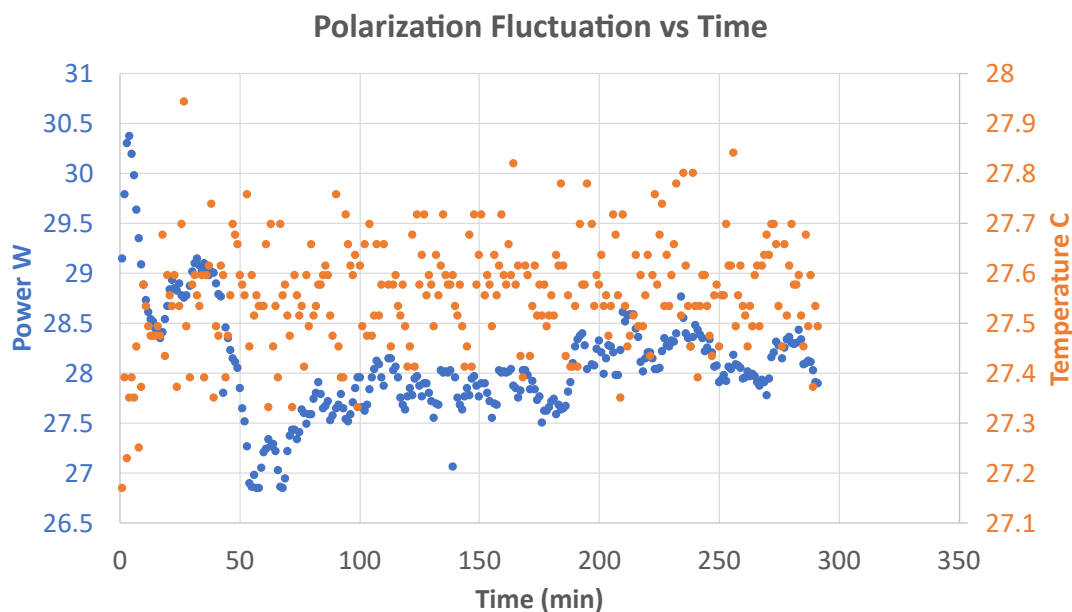


Figure 5.3: Polarization stability of the Nufern fiber amplifier is shown. You can see a transient in the output power as the amplifier is turned on. This was measured by monitoring the power transmitted through a PBS.

never be touched for any reason. To show the polarization stability a plot of the output power sent through a PBS is shown in Fig.5.3. You can see from the plot there is a transient shift in the power when the amplifier is first turned on and takes around 1 hour to settle. As such, you must let the amplifier settle every morning when you turn it on for at least an hour.

Beyond the polarization stability of the Nufern the laser is quite sensitive to back reflections into the laser amplifier through back coupling into the output fiber tip. As such, the output of the amplifier is sent through two optical isolators. The optical isolators are Thorlabs IO-5-1064-HP isolators where the input and output polarizers are removed and replaced with TFPN-1064-PW-1025 plate polarizers to reduce back reflections and the absorptive volume. Sometimes the output polarization of the amplifier changes particularly if the chiller is turned off for some time. As such, there is a quarter and half waveplate pair before the first polarizer to compensate for any drift. I will say the plate polarizers are a little tricky to align and are very sensitive to the angle as such it would be beneficial to probably put them on rotation mounts if you ever had to realign everything



## Preci 1064 nm Laser Optical Layout

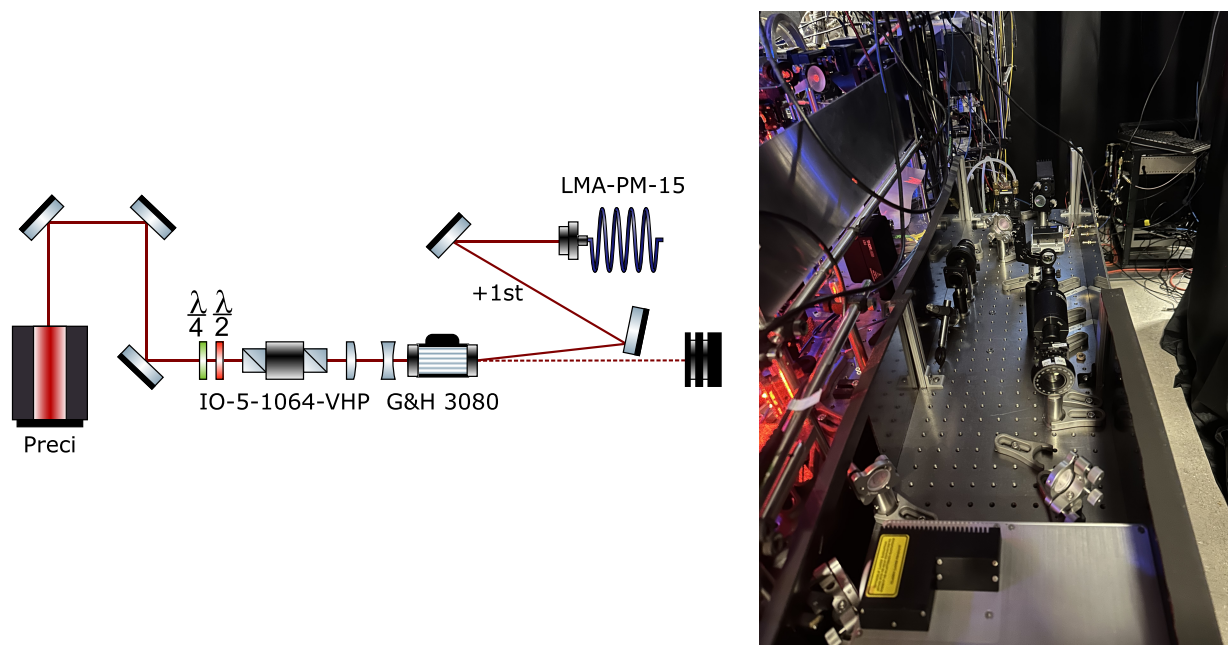


Figure 5.5: Shown is an optics diagram of the Preci fiber amplifier.

setup is very similar to the Nufern setup except that the AOM uses the +1st order diffracted beam through the AOM which is also intensity servoed. This creates a frequency shift of 160 MHz between the two beams to help ensure that there is no lattice formed in the XODT. The setup is shown in Fig.5.5. This fiber amplifier is much more stable than the Nufern amplifier as it does not exhibit polarization drift on its output and it is much less sensitive to back reflections. Additionally, we use just an off-the-shelf optical isolator rated for 100 W for a few mm beam without removing the polarizers and supplementing them with plate polarizers. Also, the NKT fiber is only 2.5 m long in this case which allows for powers  $\approx 25$  W to be coupled through the fiber before hitting the SBS limit which is significantly higher than the Nufern setup.

For both setups, all transmission optics are chosen to be UVFS as much as possible to limit thermal lensing which could be quite severe if BK7 was used by the time the beams get to the vacuum chamber. Additionally, UVFS is much purer and limits the possibility of defects in the

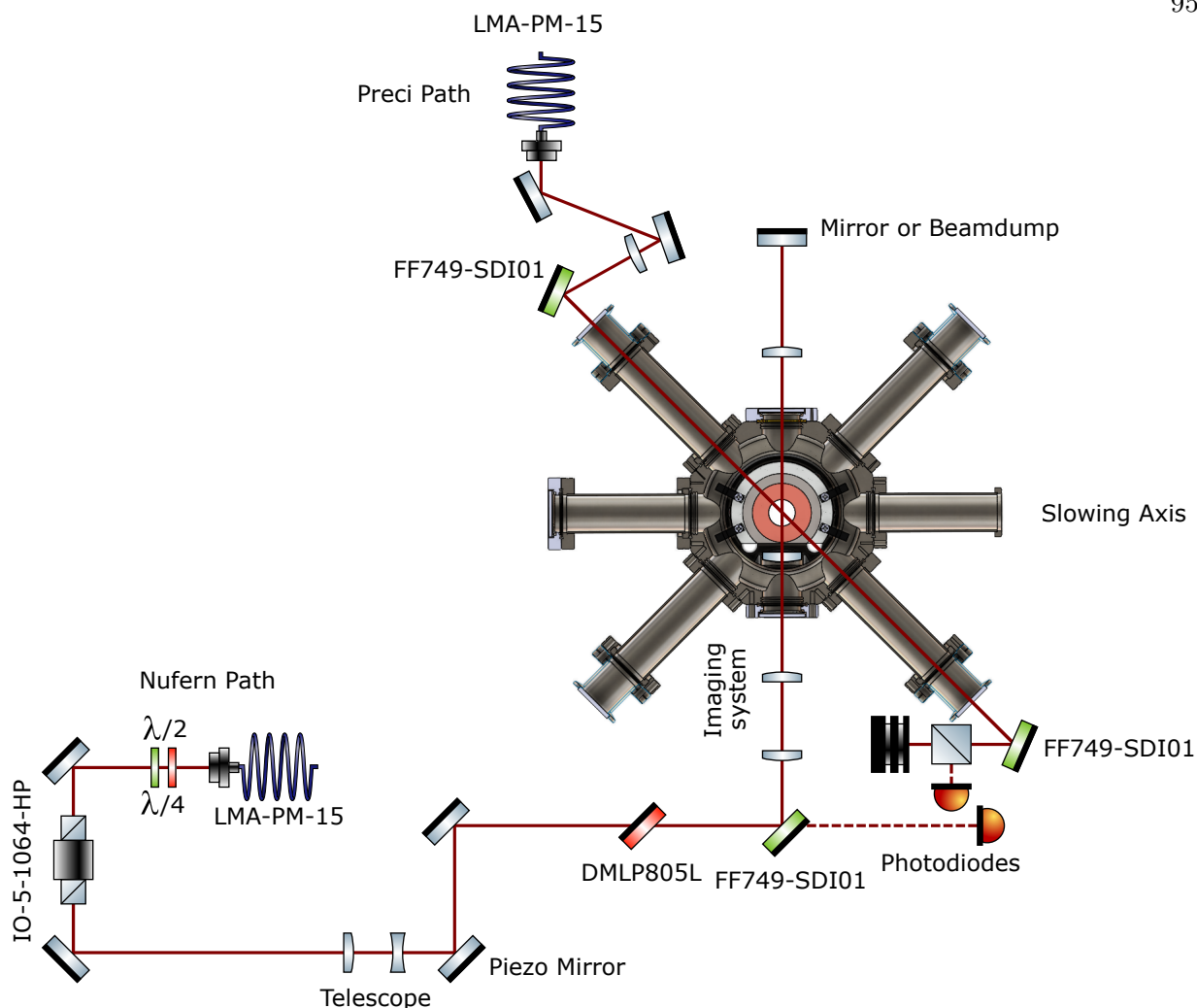


Figure 5.6: Shown is an optics diagram of the 1064 nm propagation into the experimental chamber for an XODT and optical lattice.

glass from being burnt. Also, in the images, you may notice that any flat-facing optics such as waveplates are slightly tilted. This is to prevent any reflections from back coupling back into the fiber amplifiers and is a good habit one should be conscious of when aligning high-power optics (make sure you know where reflected beams are dumping). Both fiber amplifiers are contained in blackened aluminum enclosures for safety and to create low dust environments. A single piece of dust at these powers can burn optics quite easily.

Next, I will detail the propagation of the 1064 nm beams into the vacuum chamber. The

optical paths are shown in Fig.5.6. First, the Preci path at the top is used only for the XODT. The beam is launched from the fiber and collimated to a beam waist of  $\approx 3$  mm and propagates through a 400 mm lens to focus the beam onto the BDM position with a beam waist of  $\approx 45$   $\mu\text{m}$ . The beam propagates through one of the MOT arms and combines with the MOT beams with a Semrock FF749-SDI01 dichroic mirror. The angle of the dichroic is quite awkward. The reason for this is the angle of dichroic was set to minimize the reflection of the MOT beams as GMC and particularly the BDM are quite sensitive to the power balance of the optical molasses beams. However, the introduction of the dichroic mirrors has been slightly detrimental to the BDM and has resulted in sizes around  $\approx 20$   $\mu\text{m}$  larger than during what was quoted in [11]. However, this is a tradeoff vs having an XODT or a smaller BDM. In the future when the MOT beams are made independent this effect can be almost completely mitigated. After the chamber the beam is picked off with another Semrock FF749-SDI01 dichroic mirror and the beam is dumped. Some of the light is picked off further onto a photodiode for the intensity servo of this beam. The power of this beam is typically around 19 W.

Next, the Nufern beam is also launched from the fiber similar to the Preci laser. However, this beam is used for the XODT and a 1D retroreflected horizontal optical lattice. As such, the beam is launched opposite from the chamber and propagates through an optical isolator. The reason for this is the optical isolator has large magnetic fields that perturb the GMC. Therefore the optical isolator is placed far from the chamber to reduce the effect of the magnetic field. The optical isolator is needed as the lattice is formed by retroreflecting the beam and we do not want the retroreflected beam to couple back through the fiber. The beam then propagates through two dichroic mirrors, specifically a Thorlabs DMLP805L and a custom-sized Semrock FF749-SDI01. Some light bleeds through the last dichroic and is used to intensity servo the Nufern beam. The beam propagates through part of the imaging system passing through three Edmund 67-283 lenses where one of the lenses is the in-vacuum lens. The last lens focuses the beam down to a waist of  $\approx 74$   $\mu\text{m}$  and has a typical power of around  $\approx 7$  W at this time. After the chamber, the beam is collimated with a 350 mm lens, and is either dumped for the XODT or retroreflected for the optical

lattice.

## 5.2 Loading and Cooling of YO Molecules in a 1D Optical lattice

In this section, I will discuss and summarize our results of sub-Doppler cooling and loading into a 1D optical lattice [81]. The loading into the lattice was a natural progression from our earlier work on  $\lambda$ -enhanced GMC cooling in free space [27]. Indeed, once you have a cold ensemble of molecules you want to be able to hold them conservatively for a long time for further studies such as collisions. However, the loading of the trap itself is an interesting physical problem on how to optimize the number of molecules in the trap and if it is possible to provide cooling with  $\lambda$ -enhanced GMC in the presence of the trap light.

The reason you want to apply cooling while loading the trap is that the trap is conservative meaning phase-space density is conserved. As such, the spatial extent of the loaded molecules will be translated into momentum and the overall temperature of the molecules will be higher. If however, you can remove energy from the system with tuned spontaneously emitted photons (cooling), the trajectory of the molecules in phase space will not be a circle, but a spiral inwards until the molecules thermalize with the optical molasses beams. This can create extremely high densities in the traps with successful cooling and with relatively modest trap depths.

The reason we used an optical lattice is quite simple. The optical trapping beam is created by propagating the beam through our imaging system. This makes it quite difficult to ensure the beam is level given our best efforts. As such, we saw short lifetimes in a focused dipole trap. If you calculate the experimental parameters you see that even a tilt of 1 degree is detrimental as the molecules are lost along the Rayleigh range of the dipole beam as shown in Fig.5.7. Therefore we retroreflect the dipole beam to create a 1D optical lattice. This creates a tight optical trap along the axial direction of the beam as the trap frequency along that direction is now proportional to the magnitude of the wavevector of the trapping light  $\omega_z \propto k$ . Additionally, the radial frequency is higher by a factor of 2 compared to a focused beams trap as the total intensity of the trap is  $I \propto E_{tot}^2 = E_1^2 + E_2^2 + 2E_1E_2 \cos \phi$  where  $\phi$  is the angle between the polarization of the incoming

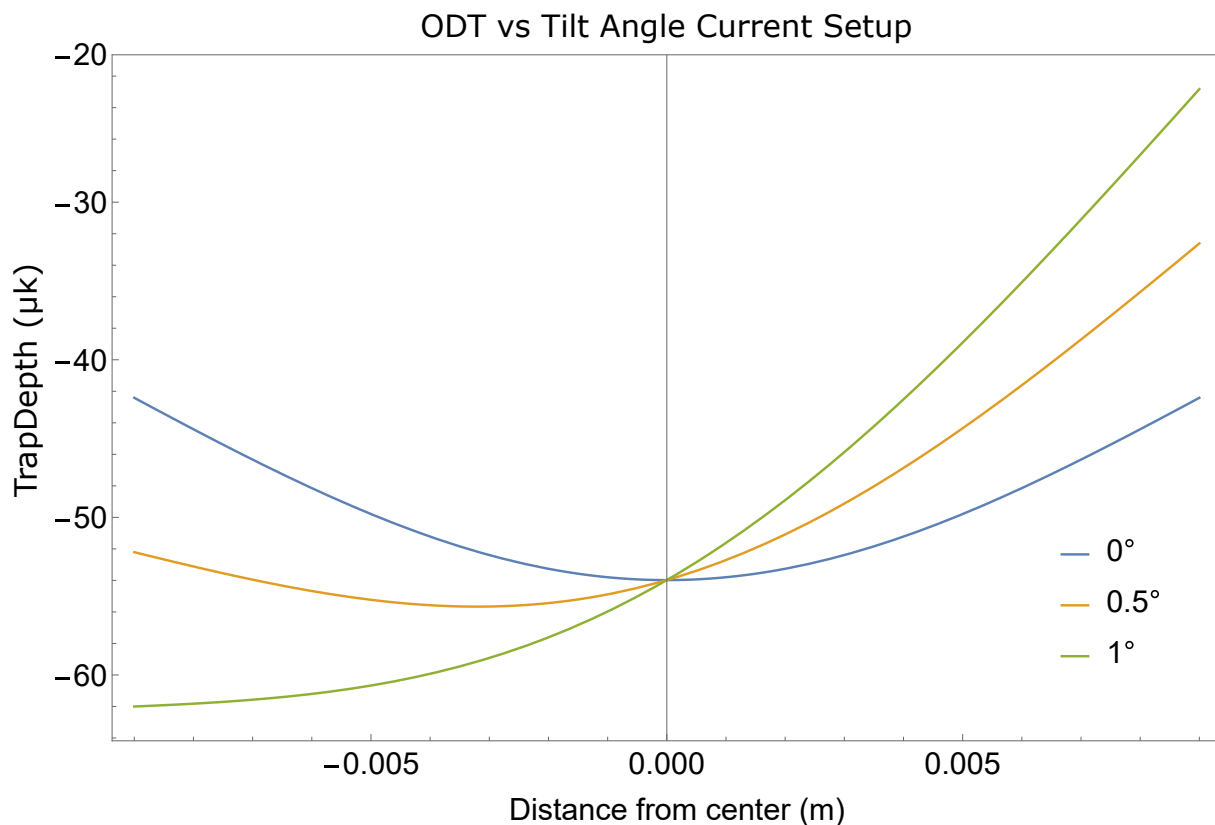


Figure 5.7: Trap depth of a focused ODT with progressively larger tilt angles with respect to gravity. The parameters are a 10 W beam with a waist of  $76.4 \mu\text{m}$  at 1064 nm. We see even an angle of 1 degree is detrimental to the trapping.

and retroreflected beam and is nominally set to 0. If the intensity of the retroreflected beam is the same as the incoming beam then  $E_1 = E_2$  and then the trap depth is 4 times larger than a single focused beam ODT.

However, there is a trade-off. Since the frequency along the axial in particular is quite large a lattice is much more susceptible to intensity noise present in the system and extra care needs to be made to ensure that the noise is low to prevent heating. For our work, this was the case, and the lifetime and heating rate of the molecules held in the lattice are shown in Fig.5.8. The lifetime is limited by the vacuum lifetime in the experimental chamber and at this time we had the lowest vacuum pressure and we found a lifetime of 850(70) ms. As a rule of thumb  $1 \times 10^{-9}$  torr equals to  $\approx 1$  second lifetime and  $1 \times 10^{-10}$  torr to  $\approx 10$  seconds. For the heating rate, we could not

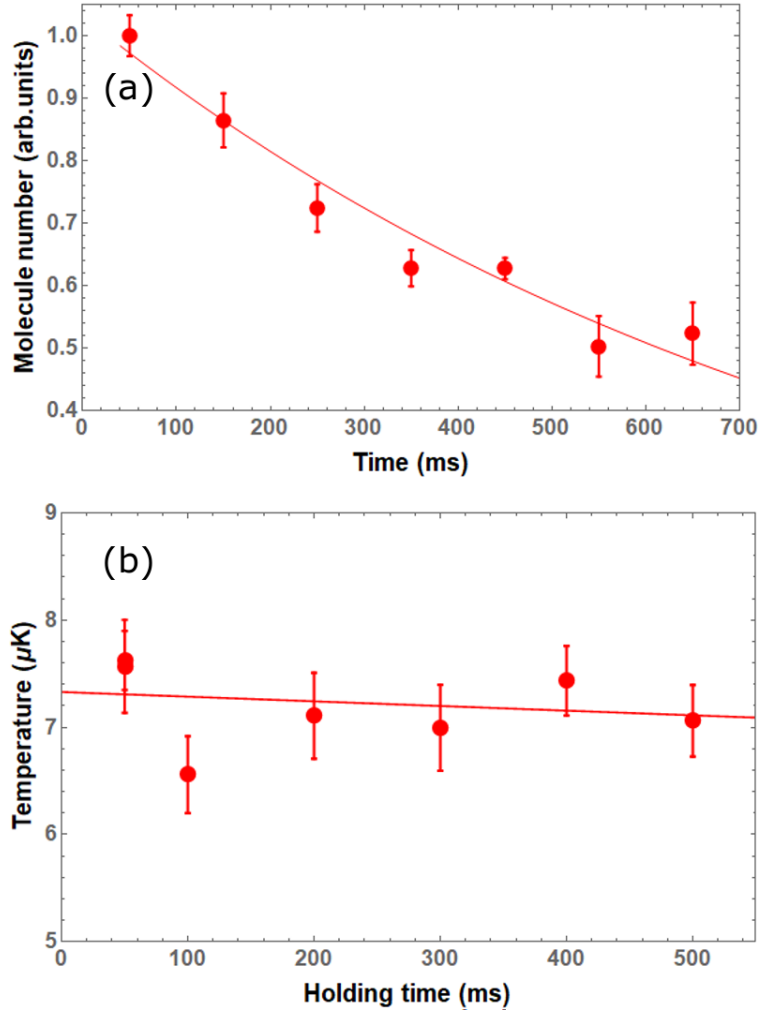


Figure 5.8: (a) Measurement of one-body lifetime in the optical 1D lattice. The solid line is an exponential fit with a  $1/e$  decay time of  $850(70)$  ms.(b) Measurement of the heating rate inside the lattice which includes both photon scattering and parametric heating from intensity noise. The solid line is a linear fit with a heating rate of  $-0.4(0.7)$   $\mu\text{K/s}$ .

measure an increase in the molecule temperature vs time relative to the experimental running time as shown in panel (b), with a heating rate of  $-0.4(0.7)$   $\mu\text{K/s}$ . I would like to note that this heating rate includes the heating from either photon scatters from the 1064 nm light or any parametric drive from the intensity noise.

We now discuss the loading of the molecules into the lattice in the presence of  $\lambda$ -enhanced GMC. The largest perturbing effect on the cooling will be the presence of differential stark shifts

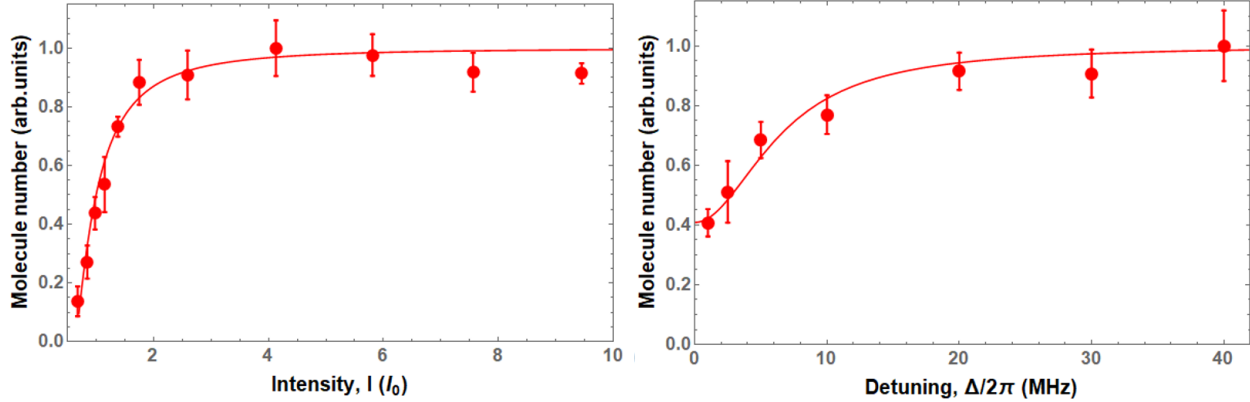


Figure 5.9: Number of molecules loaded into the lattice vs intensity and the one-photon detuning  $\Delta$ . Here the two-photon detuning is fixed to  $\delta = 2\pi \times 70$  rad/s. For the intensity scan  $\Delta = 8.3 \Gamma$ . For the one-photon detuning scan  $I = 5.5I_0$ . As both the  $I$  and  $\Delta$  increase they reach a threshold where the total loaded number of molecules plateaus. The solid lines are fitted to  $N = N_0 - k \times \rho_{ee}$ , where  $N_0$  is a constant,  $k$  is a scale factor, and  $\rho_{ee}$  is the excited state population from a three-level model solving the optical-Bloch-equations.

between the  $G = 0$  and  $G = 1$  manifolds due to the presence of trapping light. As such, the optimal parameters of GMC in free space that we discussed in Chapter 3 will need to be re-optimized. This is quite an interesting system as we have two competing lattices with lattice periods of 532 nm from the trapping light and 307 nm from the cooling light. As such, it is possible that the GMC could be abhorrently affected in the presence of the trapping light as the ground state coherence is destroyed. However, we will find that due to the favorable ground state structure of YO mainly the large spacing between the  $G = 0$  and  $G = 1$  manifolds we retain robust GMC cooling in an optical trap.

Just like the scans of  $\lambda$ -enhanced GMC in free space and in the BDM there are three parameters that can be scanned the Intensity  $I$ , the one-photon detuning  $\Delta$  and the two-photon detuning  $\delta$ . Here  $I$  is split evenly between the two beams addressing the  $v = 0, B^2\Sigma^+, N = 1, G = 0, 1$  manifolds as depicted in Fig.4.5 (B). To start, the lattice beams are ramped on and the GMC is applied overlapping with the lattice beams for 50 ms which was found to maximize the loaded number of molecules. We first turn our attention to scans of  $I$  and  $\Delta$  vs the loaded number in the

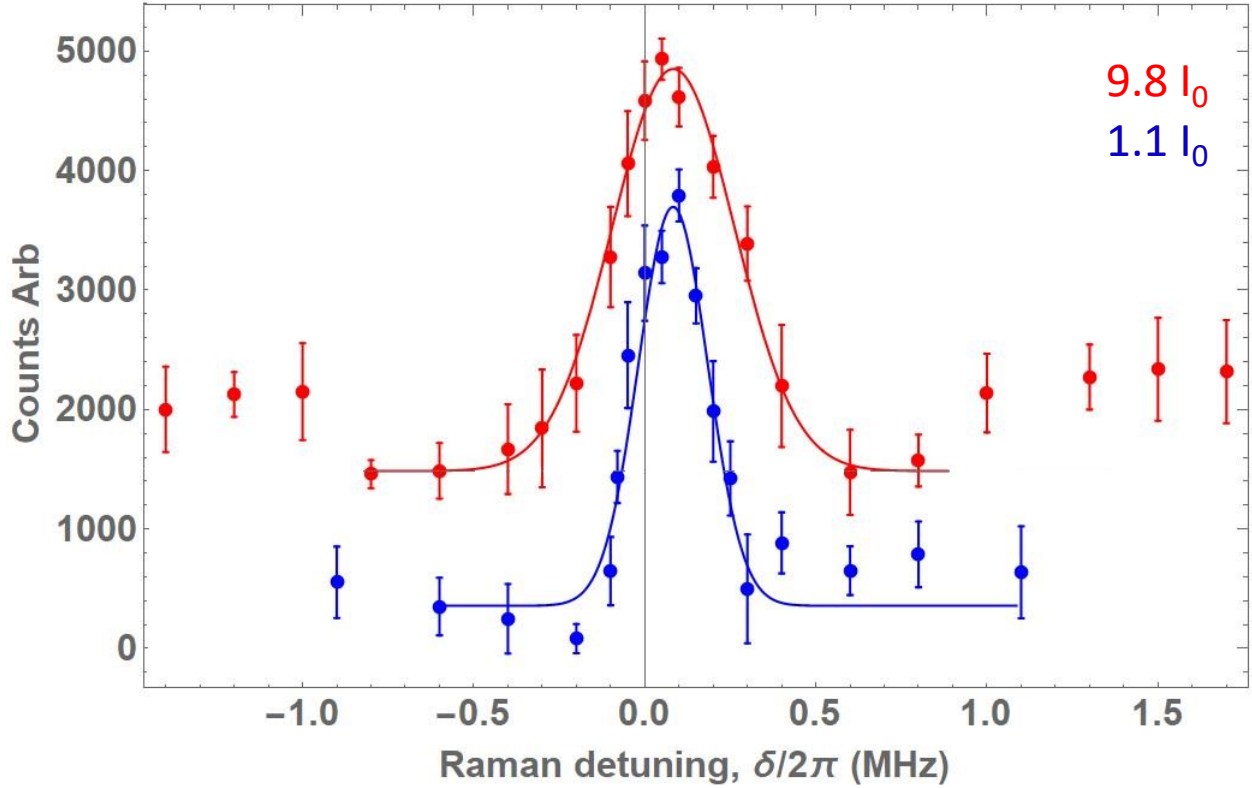


Figure 5.10: Number of molecules loaded into the lattice vs the the-photon detuning  $\delta$ . Here  $\Delta = 8.3 \Gamma$  and the scan is taken at two different intensities  $I = 9.8I_0$  and  $1.1I_0$ . A pronounced peak appears in the loaded number vs  $\delta$  as when the resonance condition is satisfied a robust dark state is formed. As the intensity increases the resonance becomes broader.

lattice. We fix  $\delta = 2\pi \times 70$  rad/s. We find that at an intensity of  $2I_0$  and  $\Delta = 4.2\Gamma$  the loaded number of molecules is maximized and plateaus as shown in Fig.5.9. The solid lines are fitted to  $N = N_0 - k \times \rho_{ee}$ , where  $N_0$  is a constant,  $k$  is a scale factor, and  $\rho_{ee}$  is the excited state population from a three-level model solving the optical-Bloch-equations. We find good agreement with such a simple model.

These results can be summarized as follows, for the intensity at  $2I_0$  the scattering rate is high enough such that the molecules do not sag vs gravity and have an optimal overlap with the trapping beams. This is similar to the results when applying GMC in free space as at around  $1I_0$  the molecules are hardly held against gravity (requires a few kHz scattering rate) and is the lowest intensity that can be used to hold the molecules in the molasses. As the intensity increases the

temperature does increase (only marginally) however, the temperature achieved is low enough such that  $\eta \approx 8$ . However, at high intensities around  $9I_0$  we see a tailing off of the number indicating that the temperature increase from momentum diffusion is becoming deleterious. For  $\Delta$  the picture is quite simple as  $\Delta$  increases the temperature decreases and the rate of change of  $\rho_{ee}$  becomes small at large detunings as such we see a plateau of the loaded molecule number.

Next, we can scan out the loaded number of molecules vs  $\delta$ . While holding  $I$  and  $\Delta$  fixed. The results are shown in Fig.5.10 with the one-photon detuning fixed to  $\Delta = 8.3 \Gamma$  and at two different intensities  $I = 9.8I_0$  and  $1.1I_0$ . Here we see a pronounced narrow peak appear for both scans as we would expect, as again when the two-photon resonance condition is satisfied  $\delta = 0$  a coherent and robust dark state is formed. Here we see that the optimal detuning compared to free space is shifted by  $\approx 100$  kHz blue indicating a differential stark shift between the  $G = 0$  and  $G = 1$  manifolds on that order. This is a powerful tool to measure the differential stark shift of the ground state manifolds. However, as we detune away from the resonance condition there is a dip and a slight recovery of the loaded number. This is again attributed to the heating that was seen as we detune away from resonance in free space. I will not repeat it here but the discussion is laid out clearly in Chapter 3 (section 3.4). We do note however that as the intensity increases the resonance gets broader. This is what is predicted as the width of the "EIT dip" is proportional  $\pm \frac{\Omega^2}{\Gamma}$  and in this range the excited state population will be suppressed. With optimized parameters of  $I = 1.4I_0$ ,  $\Delta/2\pi = 40$  MHz and  $\delta/2\pi = 70$  kHz, we load a maximum of  $\sim 1200$  molecules (limited only by mode matching of the beams to the cloud) into the optical lattice with a temperature of  $7.0(6) \mu\text{K}$ . This corresponds to a PSD of  $3.1 \times 10^{-6}$ , and at the time this was the largest PSD achieved for a "bulk" gas of laser-cooled molecules only beaten by our recent work collisions in a XODT.

We can perform another interesting experiment now that the molecules are loaded and conservatively trapped in the lattice. The experiment is to test what is the lowest possible temperature that can be achieved with  $\lambda$ -enhanced cooling. As stated previously, the lowest intensities are limited in free space as the molasses cannot "hold" the molecules against gravity. However, in the optical lattice, this is not a limit. If we apply a large  $\Delta$  detuning and an optimized two-photon de-

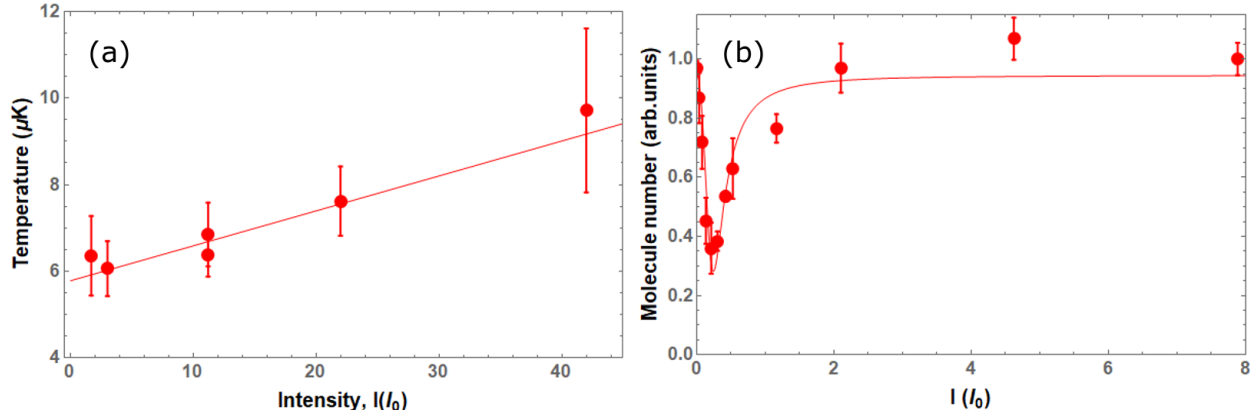


Figure 5.11: (a) Shown is the temperature versus intensity  $I$  with  $\Delta=8.3\Gamma$  and  $\delta=2\pi\times 70$  rad/s. The solid line is a linear fit. (b) Number of remaining molecules versus  $I$  with  $\Delta=8.3\Gamma$  and  $\delta=2\pi\times 70$  rad/s. The solid line is a fit to the function  $N = N_0 - k \times \rho_{ee}(I)$ , where  $k$  is a scale factor, and  $\rho_{ee}$  is the excited state population calculated with the optical-Bloch-equations.

tuning  $\delta$  and lower the intensity, the temperature should also decrease. As again, for a sub-Doppler mechanism the temperature scales linearly with intensity  $T_{avg} \propto I$ . You may think, however, that since we have two competing lattices on top of each other at all times the cooling will be compromised. While this may be true to some extent this much to my surprise was not the limiting factor.

The results of such an experiment are shown in Fig.5.11. Here after loading the molecules, we waited for 40 ms for the unloaded molecules to fall out of the view of the CCD. We then applied an additional 30 ms of GMC cooling while scanning out the intensity while holding  $\Delta=8.3\Gamma$  and  $\delta=2\pi\times 70$  rad/s. First in panel (a) as the intensity is lowered we find lower temperatures scaling linearly with  $I$  as we would expect. However, as the intensity is lowered below one  $I_0$  we see pronounced molecule loss. Additionally, at these lower intensities (which is not shown) we see heating of the molecules. The solid line is again a fit from using the optical-Bloch-equations fitting  $N = N_0 - k \times \rho_{ee}(I)$ , where  $k$  is a scale factor, and  $\rho_{ee}$  is the excited state population for the given above parameters. We find that whenever the excited state population is sufficiently occupied, there is heating and large molecule loss. This would suggest that there are two mechanisms at play.

First, the GMC cooling is becoming compromised as the excited state population is increased, and the final temperature scales linearly with  $\rho_{ee}$  from Eq.3.3. Second, since there is trapping light at 1064 nm present, transitions driving  $v = 0, A^2\Pi_{1/2}, J = 1/2^+ \rightarrow$  "Excited - states" are possible in particular it is reasonable that the 1064 nm light is driving a transition to the  $D^2\Sigma^+$  state, which has transitions near 1064 nm and the trapping light sits on a broad ASE pedestal 10s nm wide with high peak intensity. This can just pump the molecules into other vibrational/rotational states through a multi-photon process and thus are dark to our fluorescence beams on the  $v = 0, X^2\Sigma^+, N = 1^- \rightarrow v = 0, A^2\Pi_{1/2}, J = 1/2^+$  transition.

## Chapter 6

### Collisions of YO Molecules

Collisions of YO molecules at ultralow temperatures represent the culmination of the work during my PhD. Magneto-optical trapping, sub-Doppler cooling, and conservative trapping are all methodologies that allow the manipulation and preparation of the molecules at high phase-space densities. Jun may not remember, but when I joined the lab many years ago he suggested that by the end of my PhD, I could see collisions of YO molecules in a tightly focused optical trap. I am happy to report that through much work I was able to meet this expectation, and I led this work as well. The work on collisions is detailed here [12].

#### 6.1 Theory of Ultracold Collisions

In this section, I will describe the basic physics involved with ultracold scattering as a reference before discussing the experimental results. The basic theory is shown in Fig.6.1. Here the collision of two molecules can be decomposed in the center of mass frame of particles of reduced mass  $\mu = \frac{m_1 m_2}{m_1 + m_2}$  and energy  $E_{in} = \frac{\hbar^2 k^2}{2\mu}$  impinging with some flux  $\vec{j}_{in}$  onto a potential  $U_{int}$  along the z-direction. This is shown with the orange balls. The interaction with the potential is generally cast in the form of the flux  $\vec{j}_{in}$  in some cross-section  $d\sigma$  scattering into some solid angle  $d\Omega$  with outgoing flux  $\vec{j}_{out}$ . The reason for this is this is generally how you would measure some scattering process. Send in some particles and measure the number of molecules per unit time  $Nd\Omega$  scattered into a range angles  $d\Omega$  with some detector. The incoming differential cross-section  $d\sigma$  characterizes the "strength" of the scattering process and depends on the kinetic energy of the incoming flux

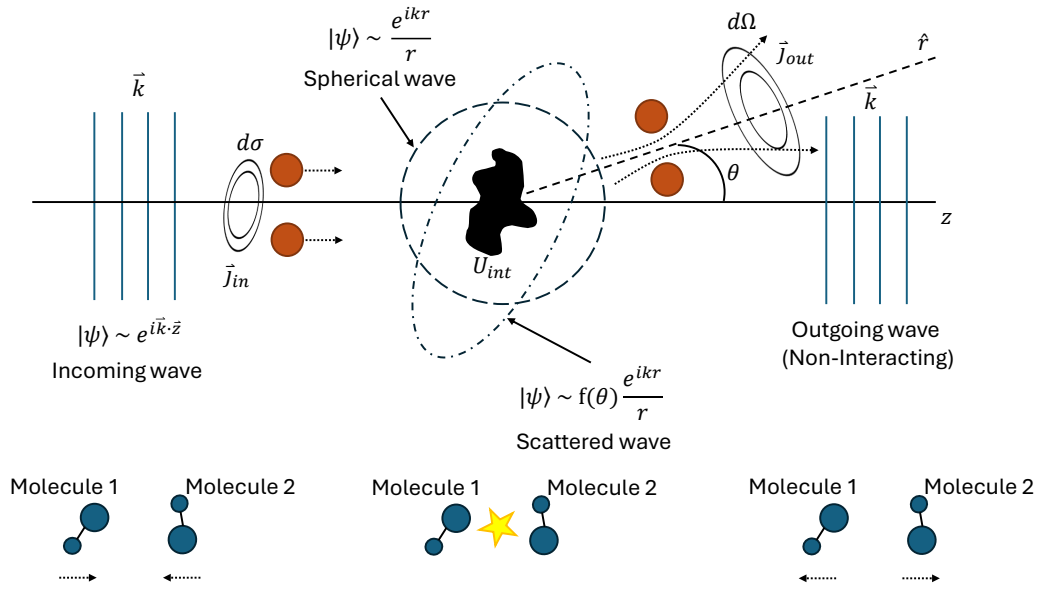


Figure 6.1: Shown is the basic intuition of low energy scattering. The collision of two molecules can be decomposed in the center of mass frame with particles of reduced mass  $\mu = \frac{m_1 m_2}{m_1 + m_2}$  and energy  $E_{in} = \frac{\hbar^2 k^2}{2\mu}$  impinging with some flux  $\vec{j}_{in}$  onto a potential  $U_{int}$  along the  $z$ -direction. This is shown diagrammatically with the orange balls. The incoming differential cross-section  $d\sigma$  characterizes the "strength" of the scattering process and depends on the kinetic energy of the incoming flux and the strength of  $U_{int}$ . If an asymptotic form of the wave function is assumed the differential cross section is then  $\frac{d\sigma}{d\Omega} = |f(\theta)|^2$ . Where  $f(\theta)$  is the scattering amplitude.

and the strength of  $U_{int}$ . Using number conservation we note that  $\frac{d\sigma}{d\Omega} = \frac{N}{j_{in}}$  where  $N$  is the number of particles. The goal is to determine the ratio of  $\frac{d\sigma}{d\Omega}$  and integrate this ratio to get the total scattering-cross section  $\sigma$ . Both of these quantities are shown diagrammatically in the figure.

To find  $\sigma$  we will assume an asymptotic form of the wave function,

$$|\psi(r, \theta)\rangle = \lim_{r \rightarrow \infty} \left( e^{i\vec{k} \cdot \vec{r}} + f(\theta) \frac{e^{ikr}}{r} \right), \quad (6.1)$$

this form is well motivated as at far distances from the potential Schrodinger's equation will give a plane wave solution, and assuming an isotropic potential (generally a good assumption), the scattered wave will look like a spherical wave with some amplitude dependent on  $\theta$  called the

scattering amplitude  $f(\theta)$  as shown in Fig.6.1.

If the potential is assumed to be isotropic and falls off faster than  $1/r$  the incoming plane wave can be expanded in terms of "partial waves" at large  $r$ . This means that the wave function can be represented by some radial wave function times a spherical harmonic. Applying constraints like the total probability density of the wave function is conserved before and after scattering and matching equations at large  $r$ , after many steps which are detailed in length here [57], you will find  $\frac{d\sigma}{d\Omega} = |f(\theta)|^2$  and that the total elastic cross-section is,

$$\sigma_{elastic}(k) = \frac{4\pi}{k^2} \sum_{l=0}^{\infty} (2l+1) \sin^2 \delta_l(k) = \frac{4\pi}{k^2} \sum_{l=0}^{\infty} (2l+1) \frac{1}{1 + \cot^2 \delta_l(k)}. \quad (6.2)$$

I want to concentrate on the form of this equation. First, the quantity  $\delta_l(k)$  is the short-range phase shift and is the phase shift of the incoming plane wave wavefunction due to the interaction potential. This is very convenient as all of the short-range interactions are quantified by  $\delta_l(k)$ . It can be thought that the sole job of the interaction potential is to adjust  $\delta_l(k)$  in the simplest picture. Next, the cross-section scales with  $\frac{1}{k^2}$  which is inversely proportional to the incoming energy of the plane wave. Therefore, slower molecules will have a larger cross-section. This can be interpreted as the molecules having a larger de-Broglie wavelength, and can more effectively "see" each other. The sum over  $l$  represents the  $l$ th partial wave involved with the collision. The waves are usually called s,p,d,f... corresponding to  $l = 0,1,2,3...$  as a call back to spectroscopic notation in atoms. Due to symmetry requirements of the overall wavefunction, distinguishable particles can interact through all partial waves and indistinguishable bosons and fermions can only interact through even or odd partial waves respectively.

The maximum possible cross section is defined as  $\sigma_{unitary} = \frac{4\pi}{k^2} (2l+1)$  where the phase shift is  $\delta_l(k) = \frac{\pi}{2}$  where  $l$  represents largest participating partial wave. This sets the possible upper bound on the cross-section. While the cross-section is convenient to understand the strength of the scattering process, it is often more convenient to put the process in terms of a rate often cast in units of  $cm^3s^{-1}$ . To do this we need to multiply the cross-section by the probability current of the

plane wave. For a plane wave of reduced mass  $\mu$  you find a probability current of,

$$j = \frac{\hbar}{2mi} \left( \psi^* \frac{\partial \psi}{\partial x} - \psi \frac{\partial \psi^*}{\partial x} \right) = \frac{\hbar k}{\mu}, \quad (6.3)$$

assuming the plane wave has an amplitude of one.

Beyond just elastic collisions, in molecules for all species at or near ultracold temperatures  $\approx 1 \mu\text{K}$ , a strong inelastic/collisional loss is observed which is either due to internal relaxation of rotational or hyperfine levels in the ground electronic state, or which is usually the case when the molecules are spin-polarized in the absolute ground state, the loss is caused by either chemical reactions or "sticky-collisions". Sticky collisions occur when the optical trapping light drives transitions to a dense continuum of states. This dense continuum is theorized to occur because the molecules form a transient complex bound state when they approach each other at short range. In this case, the inelastic cross-section is defined as,

$$\sigma_{inelastic}(k) = \frac{\pi}{k^2} \sum_{l=0}^{\infty} (2l+1) \sin^2(1 - |\eta_l(k)|^2) = \frac{\pi}{k^2} \sum_{l=0}^{\infty} (2l+1) \frac{1}{1 + \cot^2(1 - |\eta_l(k)|^2)}, \quad (6.4)$$

where  $\eta_l(k)$  is defined as  $\eta_l(k) = e^{2i\delta_l(k)}$ . We note a very fundamental result herein that the maximum inelastic cross-section can only ever be one-fourth of the elastic cross-section.

Another important quantity related to the scattering process is the scattering length. To get this quantity we assume a threshold model where the effective interaction potential is,

$$U_{int} = \frac{\hbar^2 l(l+1)}{2\mu r^2} - \frac{C_s}{r^s}, \quad (6.5)$$

where the first term is the centrifugal barrier height and the second term describes the interaction (van der Waals,  $s = 6$ ). The barrier peaks at a distance of [57],

$$r_b = \left( \frac{\mu s C_s}{\hbar^2 l(l+1)} \right)^{\frac{l}{s-2}}, \quad (6.6)$$

with a corresponding barrier height defined as,

$$V_b = \frac{\hbar^2 l(l+1)}{2\mu r_b^2} - \frac{C_s}{r_b^s}. \quad (6.7)$$

We also assume that the  $E_{in} \ll V_b$  which is defined as the threshold regime. When you make these assumptions and you match the forms of the wavefunctions at  $r_b$ , you find that the phase shift has a relation given as [57],

$$\tan \delta_l(k) = \lim_{k \rightarrow 0} -\mathcal{L} k^{2l+1}. \quad (6.8)$$

The parameter  $\mathcal{L}$  has the unit of length. This parameter  $\mathcal{L}$  is the scattering length for partial wave  $l$ . For example, the lowest-order scattering length would be that of s-wave defined as,

$$a_s = \lim_{k \rightarrow 0} -\frac{\tan \delta_{l=0}(k)}{k}. \quad (6.9)$$

This is an extremely convenient expression. If we take Eq.6.10 and plug it into the RHS of Eq.6.2 we find that for s-wave collisions the cross-section is,

$$\sigma_{l=0}(k) = \lim_{k \rightarrow 0} 4\pi a_s^2. \quad (6.10)$$

With this form, we have replaced the effective interaction with that of a simple hard sphere scattering model at low energy where  $a_s$  describes the collisional process. However, there are some caveats with this expression. The scaling with  $k$  in Eq.6.8 when  $s = 6$  is only true for s and p-waves. Higher-order partial waves have a different scaling. The details can be found in [57] (pg. 30).

There is an interesting consequence that occurs when  $\delta_{l=0}(k) = \frac{\pi}{2}$  in Eq.6.10. We see that  $a_s$  diverges and approaches infinity. This seems to suggest that there are particular values of  $E_{in}$  vs.  $U_{int}$  that cause resonant behavior. We can recall that very interesting behavior occurred around sharp resonances when we discussed  $\Lambda$ -enhanced GMC and the BDM. The same is true for collisions. If we probe this further by defining the incident energy that the resonance occurs as  $E_0$  you can Taylor expand  $\cot \delta_l(E)$  and you will find,

$$\cot \delta_l(E) \approx -\frac{2}{\Gamma}(E - E_0) + \dots \quad (6.11)$$

where  $\Gamma = \left( \frac{d\delta_l(E)}{dE} \right)_{E=E_0}$ . If you sub this again into the RHS of Eq.6.2 you will find,

$$\sigma_l(k) \approx \frac{4\pi}{k^2} (2l + 1) \frac{\Gamma^2/4}{(E - E_0)^2 + \Gamma^2/4}, \quad (6.12)$$

which is the famous Breit-Wigner formula for resonant enhancement.  $\Gamma$  is defined as the width of the resonance. The physical intuition here is that some quasi-stable bound state is formed with a lifetime of  $\tau = \hbar/\Gamma$ . Also, we note that when  $E = E_0$  we re-obtain the unitary limit. As such, many resonant collisions can and will approach the unitary limit. There is a naive assumption here that sitting at a resonance is beneficial because you can dramatically enhance the elastic cross-section which could enhance processes such as evaporative cooling. However, we note that the inelastic cross-section will only be a factor of 4 smaller than the elastic cross-section from Eq.6.4 which can cause strong inelastic/collisional loss.

Many resonant processes can occur in collisional processes. One example is a shape resonance. This happens if there is reflection off the short-range interaction potential  $U_{int}$ . If the reflected flux is large enough and the phase  $\delta_l(k)$  is correct, the reflected wave and incoming wave can constructively interfere causing the wave function to peak at short range. Note that for purely s-wave collisions shape resonances are impossible as there is no reflection off the short-range potential.

Another example is that of a Feshbach resonance. This occurs when two magnetic sublevels are brought to degeneracy through the application of a strong magnetic field ( $\approx 100$ s G). In this case unlike the shape resonance you can tune the resonance energy  $E_0$ . This is a powerful technique and is the basis for the formation of all ultracold bi-alkali molecules.

## 6.2 Collisions of YO Molecules

If there are no external static or oscillating electric fields that can strongly interact with the permanent dipole moment of hetero-nuclear molecules, the interaction between molecules is

described by the long-range van der Waals interaction potential  $U_{int}$ . The form of this equation is the same as Eq.6.5 with ( $s = 6$ ) given as,

$$U_{int}(r) = -\frac{C_6}{r^6} + \frac{\hbar^2 l(l+1)}{2\mu r^2} + \gamma_{sr}(r), \quad (6.13)$$

the additional term  $\gamma_{sr}(r)$  represents any very short range potentials that occur at distances  $r \ll r_b$ . From the shape of this potential, the collisional dynamics are strongly influenced by the height of centrifugal barrier heights for each partial wave determined by Eq.6.7. For the molecules to reach short range where inelastic/collisional loss can occur they need to have sufficient kinetic energy to overcome the barriers, or need to tunnel through the barriers where the tunneling probability can be estimated with the WKB approximation as  $T(E_{in}) = e^{-2 \int_{r_1}^{r_2} \sqrt{\frac{2\mu}{\hbar^2}(U_{int}(x) - E_{in})} dx}$ . Therefore by adjusting the average thermal kinetic energy of the molecules relative to the barrier heights  $V_b$ , or by comparing a spin mixture vs spin-polarized ensemble, we can determine the effect of individual partial waves on the collisional loss rates. This is shown diagrammatically in Fig.6.2.

The magnitude of the  $C_6$  coefficient is determined from two different contributions. The first is a second-order response through electronic states. These contributions are small and only contribute on the order of 10% to the  $C_6$  coefficient. The much larger contribution to the coefficient is from the rotational dipolar part, and is defined as  $C_6 = \frac{1}{(4\pi\epsilon_0)^2} \frac{d^4}{6B}$  where  $B$  is the rotational constant and  $d$  is the dipole moment in the ground state. An important related quantity is the characteristic van der Waals length  $\bar{a} = 0.47799(\frac{2\mu C_6}{\hbar^2})^{1/4}$ . This quantity sets the "effective size" of the potential where any molecules that approach each other at distances much shorter than this length can undergo collisional loss. For YO this value can be calculated and is  $411 a_0$ .

As mentioned briefly in the previous section, the hallmark sign of ultracold collisions of molecules is strong collisional loss. Intuitively you can imagine that the largest cause of loss would be chemical reactions when the molecules reach short-range, and indeed this has been the case for some molecules. For example in a remarkable experiment the reaction products and intermediate products of KRb molecules have been measured in the ultracold regime [46]. For YO the relevant

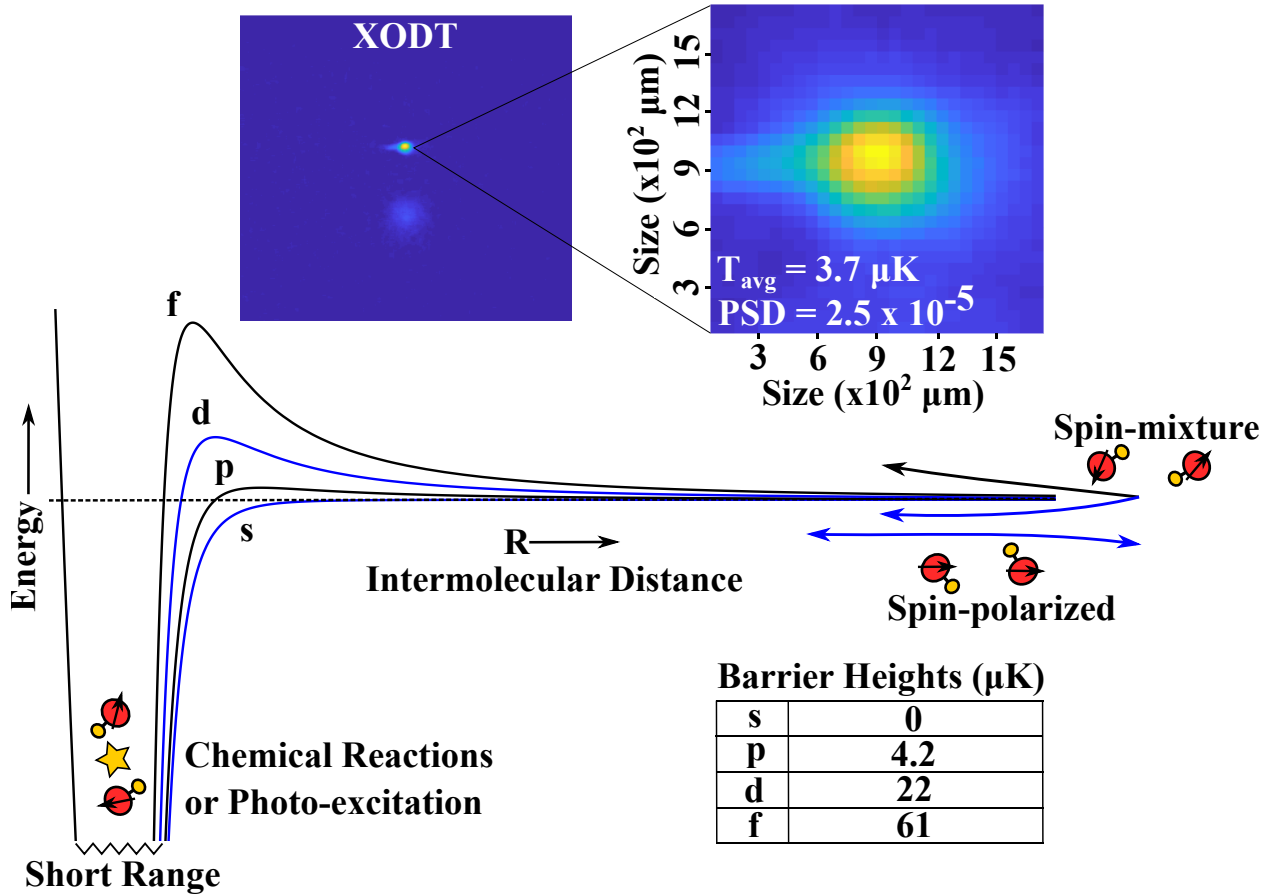


Figure 6.2: Shown is the basic physical intuition of the ultracold collisions of YO molecules. First at the TOP are Images of YO molecules loaded into a crossed optical dipole trap (XODT) where the experiment takes place. A record phase-space density for laser-cooled molecules of  $2.5 \times 10^{-5}$  is achieved inside the XODT. Bottom: Shown is the form of the interaction potential  $U_{\text{int}}(r)$ . At sufficiently low collision energies, distinguishable molecules enter through both even (s,d) and odd (p,f) partial-wave channels, where partial waves beyond s-wave feature a centrifugal barrier. The corresponding centrifugal barrier heights are shown in the table. Since YO is a boson, indistinguishable molecules collide only via even partial waves. Upon reaching short range, molecules undergo collisional loss.

chemical reactions are with the bond-swapping reaction,  $\text{YO} + \text{YO} \rightarrow \text{Y}_2 + \text{O}_2$  which is forbidden by the high binding energy of YO of 7.3 eV [1]. The other reaction channels are trimer formation channels of  $\text{YO} + \text{YO} \rightarrow \text{Y}_2\text{O} + \text{O}$  and  $\text{YO}_2 + \text{Y}$  and it is not known whether they occur, but the current best estimation is that they do not.

So if YO is non-reactive where does the loss come from? The current best guess for the

collisional loss of nonreactive molecules is that of "Sticky Collisions" [48, 47, 18, 19]. Many other molecular species other than YO that are non-reactive have seen strong collisional loss as well. The simple interpretation of these collisions is when the molecules come close together they make a transient quasi-bound molecular complex. This is a problem as the molecules are subjected to high-intensity 1064 nm light for trapping. This light can drive transitions to a large density of excited states. When this happens the molecules are lost to the trapping light.

Now we will discuss the experimental results. The experiment takes place in the XODT which is formed by the intersection of two independent 1064 nm beams at 45 degrees which provide strong conservative trapping of the molecules. The XODT beams are ramped on and held constant during the last 50 ms of our blue-detuned MOT. The quadrupole magnetic field for the MOT is then turned off and GMC is applied in the presence of the XODT beams. This cools the molecules in the XODT and aids in loading the trap during a 40 ms GMC overlap. We note that the final temperature of the molecules in the XODT from GMC is degraded due to the presence of the trapping beams. As a consequence, higher temperatures are found compared to free space cooling.

The first experiment is performed by preparing the YO molecules in a large spin mixture in the  $N = 1$  manifold and adjusting the average thermal energy of the molecules vs the barrier heights. Collisional studies of a large spin mixture in different internal states in the  $N = 1$  rotational manifold follow easily after GMC. In a steady state, the molecules are mixed over 12 spin states during the overlap with the XODT beams. The number of molecules left in the XODT as a function of time is measured by applying a pulse of light for 1.5 ms nearly resonant with the main laser-cooling transition  $v = 0, X^2\Sigma^+, N = 1^- \rightarrow v = 0, A^2\Pi_{1/2}, J = 1/2^+$ .

We study the collisional loss rate at three different temperatures which is shown in Fig.6.3. The first trace shown in blue is taken at a lower trap depth of 85  $\mu\text{K}$  with an average temperature of 3.7(5)  $\mu\text{K}$  which is below the p-wave barrier height. The second and third trace in green and red has a trap depth in the XODT of 150  $\mu\text{K}$ . The average temperature of the molecules is 8.3(1.1)  $\mu\text{K}$  and 14.5(1.7)  $\mu\text{K}$  which are both above the temperature of the p-wave barrier height of 4.2  $\mu\text{K}$ , but below the d-wave barrier height of 22  $\mu\text{K}$ . The average temperature is defined as  $T_{\text{avg}} = T_{\text{radial}}^{2/3} \times T_{\text{axial}}^{1/3}$ .

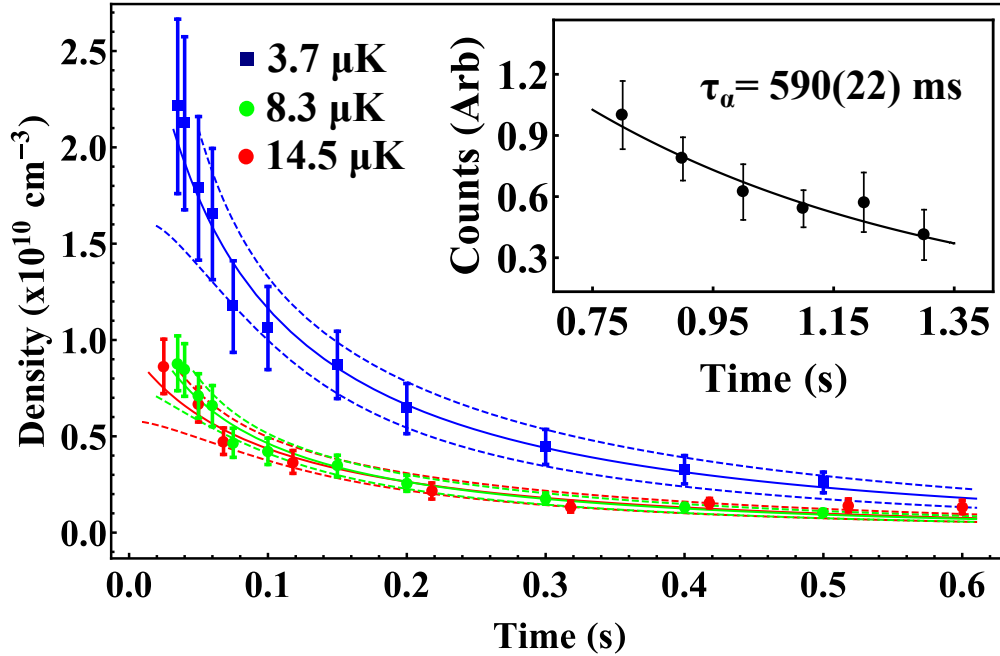


Figure 6.3: Shown is collisional loss in a large spin mixture of YO molecules in the  $N = 1$  rotational manifold spread over 12 magnetic sublevels. The loss was measured at three different average temperatures. The first trace at  $3.7(5) \mu\text{K}$  (blue-filled squares) has an average kinetic energy below the  $p$ -wave barrier height. The other two traces at  $8.3(1.1) \mu\text{K}$  (green-filled circles), and  $14.5(1.7) \mu\text{K}$  (red-filled circles) are above the  $p$ -wave centrifugal barrier height. The solid lines represent the fit of the data points to the density loss rate according to Eq. 6.14, and the dashed lines represent the 95% confidence interval bands from the fits. To quantify the fitting results we find  $\chi^2/\text{dof}$  of 0.2, 0.3, and 1.4 for the respective fits. The inset shows the one-body lifetime of  $590(22) \text{ ms}$ .

We obtain trap frequencies of  $\omega_{150\mu\text{K}} = 2\pi \times \{336,123,371\} \text{ Hz}$  and  $\omega_{85\mu\text{K}} = 2\pi \times \{253,94,263\} \text{ Hz}$ . These trap frequencies scale closely with  $\sqrt{I}$  where  $I$  is the total intensity of the XODT beams as expected. The number of trapped molecules is around  $\approx 5000$  in both cases with a capture efficiency from the BDM of 40% in the  $N = 1$  manifold. The one-body lifetime is shown as an inset for long hold times where we obtain a lifetime of  $590(22) \text{ ms}$ . A record phase-space density for laser-cooled molecules of  $2.5 \times 10^{-5}$  is achieved inside the XODT.

The solid lines represent fits to the density loss rate  $\dot{n}_{\text{mol}}$  defined as

$$\dot{n}_{\text{mol}} = -\alpha n_{\text{mol}} - (2k_2)n_{\text{mol}}^2, \quad (6.14)$$

where  $\alpha$  and  $k_2$  are the one-body and two-body loss rate coefficients. The density is determined

using the molecule number and  $V_{\text{eff}}$  which is the effective volume defined as  $V_{\text{eff}} = 8\sqrt{\pi^3}\sigma_x\sigma_y\sigma_z$  where  $\sigma_i$  is the rms width of the thermal distribution along each direction in the XODT with  $i = \{x, y, z\}$ . The rms widths are determined by the equipartition theorem  $m\omega_i^2\sigma_i^2 = k_{\text{B}}T_i$ , where  $k_{\text{B}}$  is Boltzmann's constant,  $T_i$  is the temperature, and  $m$  is the mass of YO. The temperature of the molecules is measured by time-of-flight expansion in the radial  $\{x, y\}$  direction and the axial  $\{z\}$  direction. We do not measure an increase in the temperature of the molecules with time within error. Therefore, it is justified to keep  $V_{\text{eff}}$  constant. The trapping frequencies  $\omega_i$  are determined by parametrically heating the molecules out of the XODT with an example shown previously in Fig.5.2. The experimental results are loss rates of  $k_2(3.7 \mu\text{K}) = 2.2(0.6) \times 10^{-10} \text{ cm}^3 \text{ s}^{-1}$ ,  $k_2(8.3 \mu\text{K}) = 5.6(1.8) \times 10^{-10} \text{ cm}^3 \text{ s}^{-1}$  and  $k_2(14.5 \mu\text{K}) = 4.9(1.4) \times 10^{-10} \text{ cm}^3 \text{ s}^{-1}$ .

Next, beyond just adjusting the average thermal energy of the molecular ensemble we can fix the temperature and compare the loss rates in a spin-mixture vs spin-polarized in the absolute ground state  $v = 0, X^2\Sigma^+, N = 0^+, G = 1F = 1$  and  $v = 0, X^2\Sigma^+, N = 0^+, G = 1F = 1, m_f = -1$ . This is advantageous as any collisional loss from rotational or hyperfine relaxation is absent, unlike the case in  $N = 1$ . Therefore we can directly measure the effect of sticky collisions on the loss rate. Additionally, we can directly compare the effect of all relevant partial waves vs just the even partial waves as shown in Fig.6.2. I would like to say that this was an enormous step forward in the quantum state control of the experiment. As for the first time, YO molecules can be prepared in a single quantum state.

When performing the state preparation great care must be taken to ensure the molecules are only occupying the desired quantum state without contaminating other undesired manifolds. To remove any unwanted population in  $N=0$ , during the last two milliseconds of GMC a laser pulse addressing the  $N = 0, G = 0,1, F = 0,1$  manifolds is applied driving the  $v = 0, X^2\Sigma^+, N = 0^+ \rightarrow v = 0, A^2\Pi_{1/2}, J = 3/2^-, F = 2$  transition. This optically pumps all molecules that may have built up in  $N = 0$  during the GMC cooling into  $N = 2$ . Next, the transfer of the molecules into the absolute ground state begins by optically pumping into a single quantum state  $N = 1, G = 1, F = 0$  by applying two laser tones blue detuned from the  $N = 1, G = 0, F = 1$ , and  $N = 1, G = 1, F = 2$ .

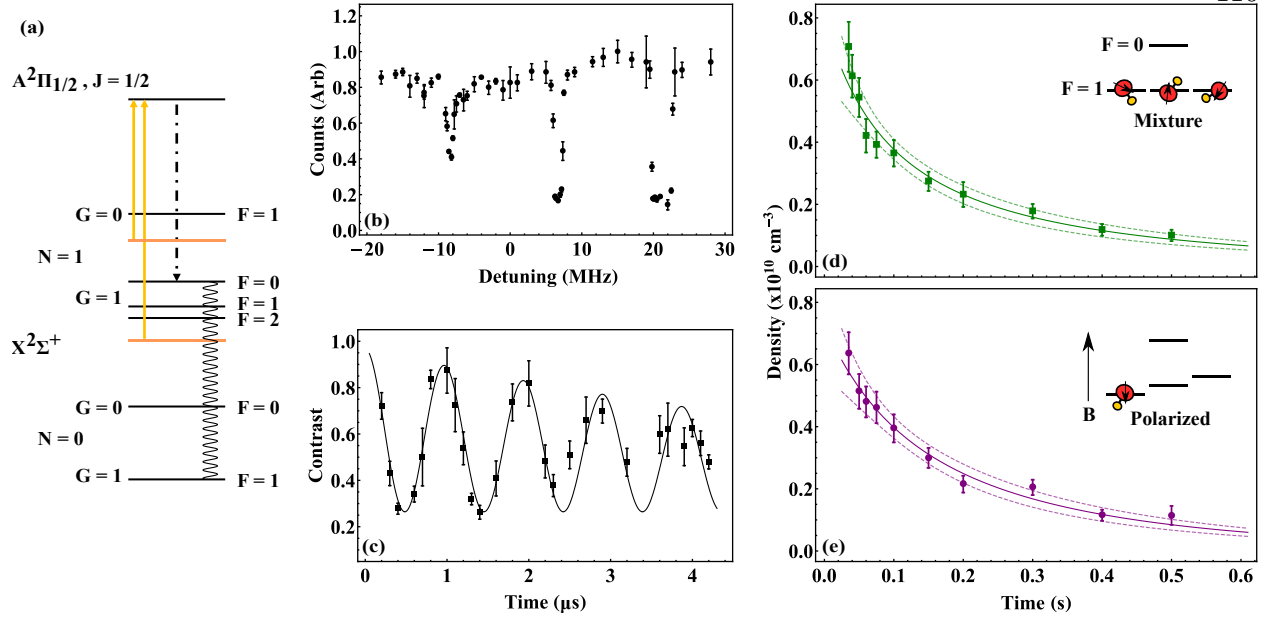


Figure 6.4: Shown are the preparation and collisional results of YO molecules in a spin mixture and polarized in the absolute ground state. (a) The transfer sequence to transfer molecules into  $N = 0, G = 1, F = 1$  as described in the text (b) Microwave spectroscopy of the transition with an applied magnetic field, showing splitting of the hyperfine sublevels in  $N = 0, G = 1, F = 1$ . (c) Rabi oscillations between  $N = 1$  and  $N = 0$ . (d) Collisional loss of YO molecules prepared in an equal mixture of spin states in  $N = 0, G = 1, F = 1$  (green-filled squares). (e) Collisional loss in single spin-polarized state  $N = 0, G = 1, F = 1, m_F = -1$  (purple-filled circles). The solid lines represent the fitting of the data points to the rate equation given in Eq. 6.14, and the dashed lines represent the 95% confidence interval bands from the fits. To quantify the fitting results  $\chi^2/\text{dof}$  of 0.8 and 0.7 are determined for the respective fits.

This process is shown in Fig.6.4 (a). A magnetic field is then applied along the z-direction to split the degeneracy of the  $N = 0, G = 1, F = 1$  hyper-fine sub-manifolds. For an incoherent mixture, no magnetic field is applied. A microwave Landau-Zener sweep is then applied linearly polarized perpendicular to the quantization axis induced by the magnetic field (if present) to transfer the molecules into a particular spin-manifold in the ground state. The resonant frequency addressing the  $N = 1, G = 1, F = 0 \rightarrow N = 0, G = 1, F = 1$  transition is 23.282405 GHz [70]. The microwave signal is generated by mixing in a tone at around 700 MHz generated from a Zurich Instruments HDAWG with an idler tone generated by a Signalcore SC5521A. This allows for arbitrary phase and amplitude modulation of the microwave signal which is beneficial for efficient population transfer

using the HDAWG. The signal is then amplified and launched out of a horn with a direct line of sight to the molecules at a distance of 80 mm. The direct line of sight was extremely important to be able to observe Rabi oscillations as without it, the decoherence rate was too fast.

Microwave spectroscopy is shown in Fig.6.4 (b) with an applied magnetic field. The measurement was taken in free space by applying a microwave field near 23.282405 GHz and letting the molecules decohere into a mixture between the  $N = 1$  and  $N = 0$  manifolds. The remaining population in  $N = 1$  was then measured with an MOT beam pulse of 2 ms as the frequency of the applied microwave field was adjusted. The offset magnetic field that splits the magnetic Zeeman levels is provided by a shim coil that is normally used to zero Earth's magnetic field. The current driver is home-built based on an APEX PA52 op-amp which is controlled by an arbitrary waveform generator. This allows for arbitrary ramping and modulation of the shim field which lays along the z-axis (along gravity). The speed of the modulation is only limited by the RL time constant of the coils which has been measured to be 2 ms.

From the figure, a clear separation of the three sub-manifolds with an applied B-field is observed. The optical pumping efficiency has high fidelity  $> 95\%$  at zero field as when the microwave frequency is red detuned, no mixing of the population between  $N = 1, G = 1, F = 1, 2$  and  $N = 0, G = 1, F = 1$  is found. Figure 6.4 (c) shows Rabi oscillations between the  $N = 1$  and  $N = 0$  rotational levels in free space as we had seen in Chapter 2. Rabi rates of  $\approx 1$  MHz are achieved this allows for fast Landau-Zener sweeps on the order of  $10 \mu\text{s}$ . Fast dephasing of the oscillations is observed with a coherence time of  $8.8 \mu\text{s}$ . We attribute this to the sidebands created by reflections off our metal chamber modulated by our vacuum turbo pumps. Similar modulations have been seen and measured in other experiments. This limits our coherent transfer of the molecules to 70% to the desired manifold in  $N = 0$ . As such, to remove all molecules after the microwave sweep in other rotational manifolds, 46 GHz microwaves mixing the  $N = 1$  &  $N = 2$  rotational levels are applied along with near-resonant light from the cooling transition. This boils all unwanted population in these manifolds out of the XODT. The loss of molecules in  $N = 0$  is read out by turning on 23 GHz microwave fields and near-resonant beams on the main cooling transition.

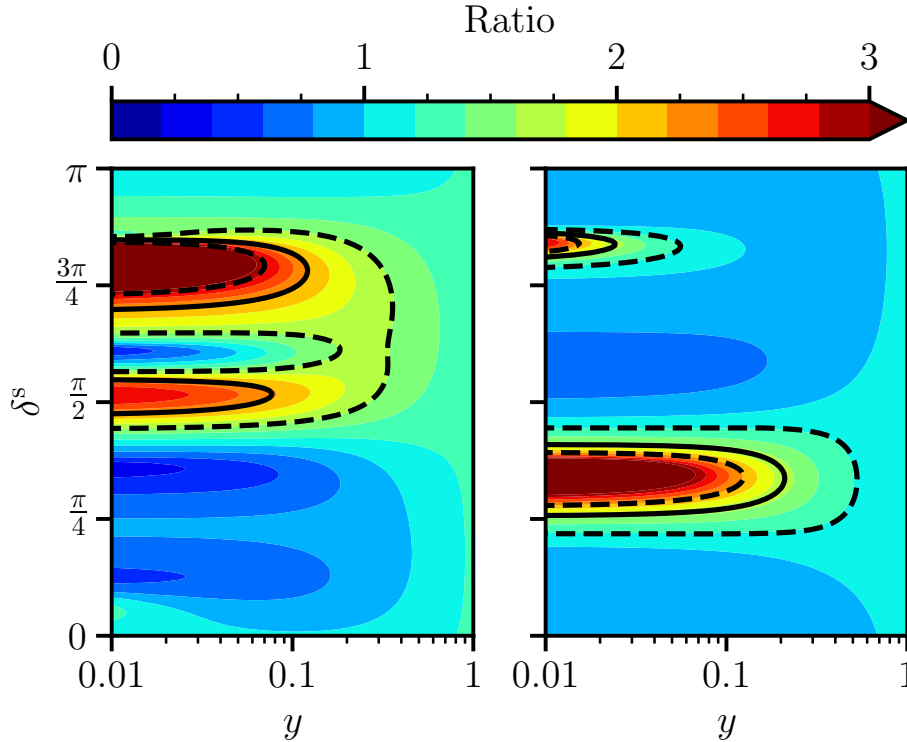


Figure 6.5: Shown are contour plots using QDT of measured ratios of the loss rates in  $N = 1$  (left) and  $N = 0$  (right). Experimentally measured ratios are shown as solid black lines, with uncertainties indicated by dashed lines. We see there are large regions that predict enhanced loss through resonant behavior. A covariance of 0.5 is assumed in the ratio of the rates.

The results for the spin mixture and spin-polarized are shown in panels Fig.6.4 c) and d). Rates of  $k_{\text{pol}} = 3.2(1.0) \times 10^{-10} \text{ cm}^3 \text{ s}^{-1}$  and  $k_{\text{mix}} = 5.4(1.5) \times 10^{-10} \text{ cm}^3 \text{ s}^{-1}$  at  $5.8 \mu\text{K}$  in the  $N = 0$  ground state at a trap depth of  $85 \mu\text{K}$  are measured. The ratio of the measured rates in  $N = 1$  between the  $3.7$  and  $14.5 \mu\text{K}$  traces and spin-polarized vs a spin-mixture in  $N = 0$ , are  $2.2 \pm 0.6$  and  $1.7 \pm 0.6$  assuming a covariance of 0.5. We see that for both cases the presence of higher order partial waves increases the rates particularly much more so in  $N = 1$ . This could suggest the presence of shape resonances.

Therefore we had some of our theory colleagues specifically Matthew D. Frye and Jeremy Hutson perform calculations on the predicted loss rates. The theory models are based on "Quantum Defect Theory" (QDT) which is a method that has been quite successful in describing collisional

loss in ultracold molecular systems [37, 30, 31]. The basic physical premise is to put an absolute absorbing boundary condition at a short range where the collision physics is determined by two parameters  $y$  and the phase shift  $\delta_l(k)$ . Where  $y$  represents the percentage of flux that reaches short-range distances less than  $\bar{a}$  and undergoes collisional loss, and  $\delta_l$  as we had previously described contains all the information of the interaction of the molecules at short range from  $U_{int}$ . Their results are shown in Fig.6.5.

The left contour plot shows the ratio of the rates in  $N = 1$  while scanning both  $y$  and  $\delta_l(k)$ . The dashed lines represent the experimental uncertainty. Two large regions correspond to resonant behavior from either a d or f-wave resonance. There is similar behavior for  $N = 0$  which corresponds to a p-wave resonance. If there are resonances in play, particularly in  $N = 1$  it would be interesting to map out the behavior. If the molecules could be brought to a lower temperature through evaporation the resonant behavior could be mapped out with lower error. Applying electric fields would shift these resonances around and confirm their existence.

Of course, the collisional loss is undesirable behavior and the collision of molecules is what I would call a "dirty" problem in that the loss is unwanted and the interaction potentials  $U_{int}$  are complicated. As such, in the field, I believe there has been a shift away from studying collisional physics and just jumping to shielding the collisional loss through either microwave or electric field shielding. These shielding techniques have been very successful and have brought three alkali molecular species to degeneracy already [22, 75, 62, 13, 7]. Currently, we are building a setup for microwave shielding as shown in Fig.6.6. The setup creates very pure circular polarization by feeding a dual-fed degenerate waveguide with crossed linear polarization. Two gold parabolic mirrors then collimate and then focus the microwaves. This has the benefit of reducing reflections in the vacuum chamber and drastically increasing the intensity for higher Rabi frequencies. The details of the setup will be described in future publications.

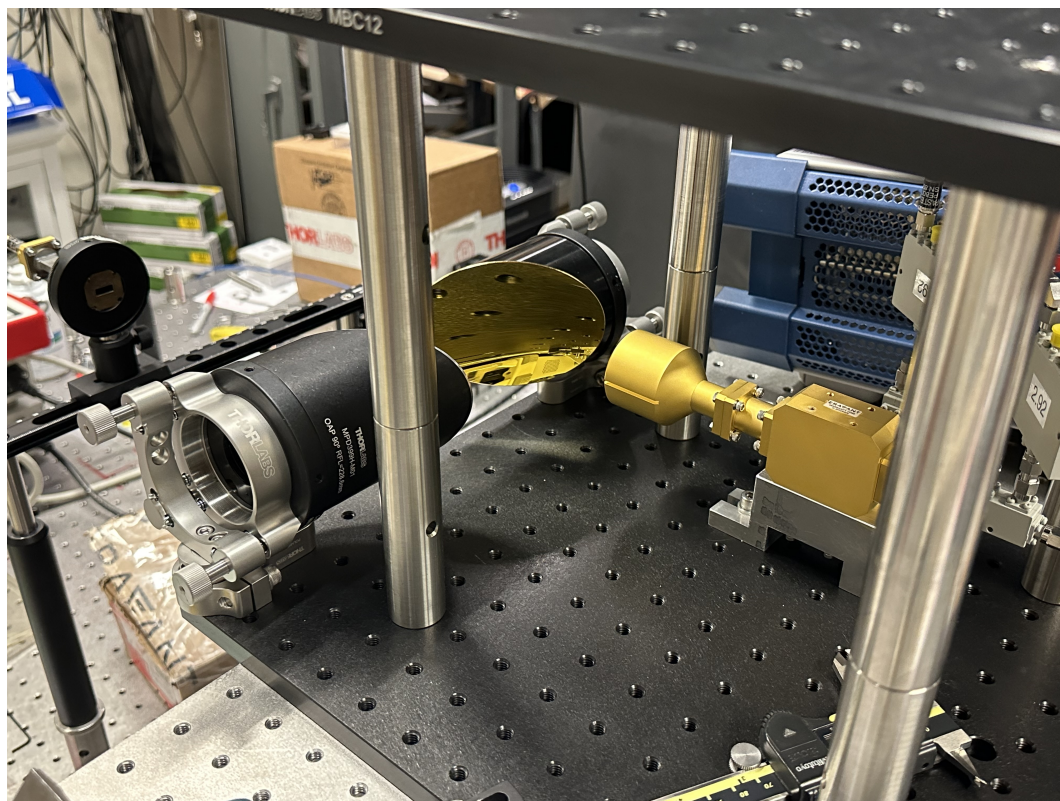


Figure 6.6: Shown is the new microwave shielding setup for shielding of collisional loss and subsequent evaporative cooling of YO molecules.

## Chapter 7

### Conclusion and Future Prospects

In this chapter, I would like to briefly discuss future experiments applicable to YO. It is indeed exciting that we now have a gas of directly laser-cooled molecules with an appreciably large ground state dipole moment, and a PSD high enough such that the molecules are interacting with each other, and we can study their collisional properties. Therefore I would like to delve into some future prospects.

#### 7.1 Magnetic Trapping

One interesting pursuit is that of magnetic trapping which has been mentioned in previous chapters. If we recall the absolute ground state of YO consists of the triplet state  $v = 0, X^2\Sigma^+, N = 0^+, G = 1, F = 1$ . From section 2.4, we know that this state is magnetically sensitive in that we have  $1 \mu_B$  sitting in the ground state from the unpaired electron spin. This is unique to most of the laser-cooled diatomic species as generally, the absolute ground state is not magnetically sensitive. The low field seeking state would be that of  $v = 0, X^2\Sigma^+, N = 0^+, G = 1, F = 1, m_f = 1$  in YO.

First, this has direct applications to magnetic transport. Currently, our vacuum lifetime is limited to around 600 ms due to the constant flow of helium into the chamber even with the in-vacuum shutters. To perform evaporation for future experiments, we need to significantly increase the vacuum lifetime. One way to do this (similar to our sister experiment on KRb molecules) is to trap the molecules in a strong quadrupole field and transport the molecules over roughly 0.5 m to a glass cell with lots of differential pumping (low conductance between chamber and cell). If the

molecules are appreciably hot then spin flip losses at the null of the field will be negligible, and we can transport a significant fraction of the molecules.

Additionally, it would be interesting to study collisional processes in the magnetic trap. Since YO is non-reactive the leading theory for such loss is sticky collisions described in the previous chapter. If the molecules are prepared into a significantly deep trap at low temperature it would be interesting to see if there is still two body loss. I would note similar experiments have been performed in Wolfgang Ketterle's group on NaLi molecules where two body losses were still seen. However, NaLi is reactive unlike YO and it would be interesting to repeat such an experiment on YO.

An update on magnetic trapping is shown in Fig.7.1. A magnetic trap of YO is shown in the top left panel of the figure after holding for 200 ms. The molecules are polarized in the  $v = 0, X^2\Sigma^+, N = 0^+, G = 1, F = 1, m_f = 1$  state. The lifetime is  $\approx 850$  ms with around 7000 molecules loaded at the time. The lifetime is limited by the background gas pressure. The average temperature of the the molecules after holding in the trap for 60 ms is  $\approx 7 \mu\text{K}$ . The density is  $2.5 \times 10^7 \text{ cm}^{-3}$ , with a phase space density of  $2.5 \times 10^{-9}$ . While this is significantly lower than the XODT, it is by far the highest densities achieved in a magnetic trap of directly laser-cooled molecules. Efforts are currently underway in the lab to improve the mode matching with the trap.

## 7.2 Microwave Shielding of YO

Another exciting avenue is that of microwave shielding discussed in brief in the previous chapter. This is currently being pursued in the lab as of writing this thesis. The basic intuition is that applying a blue-detuned circularly polarised microwave field dresses two rotational states. This creates an upper field dressed state that has a repulsive interaction at short range and a lower field dressed state that has an attractive interaction at a short range [62]. A simple diagram of the dressing is shown in Fig.7.2.

At long-range the dressing creates a dipole-dipole interaction given by [62],

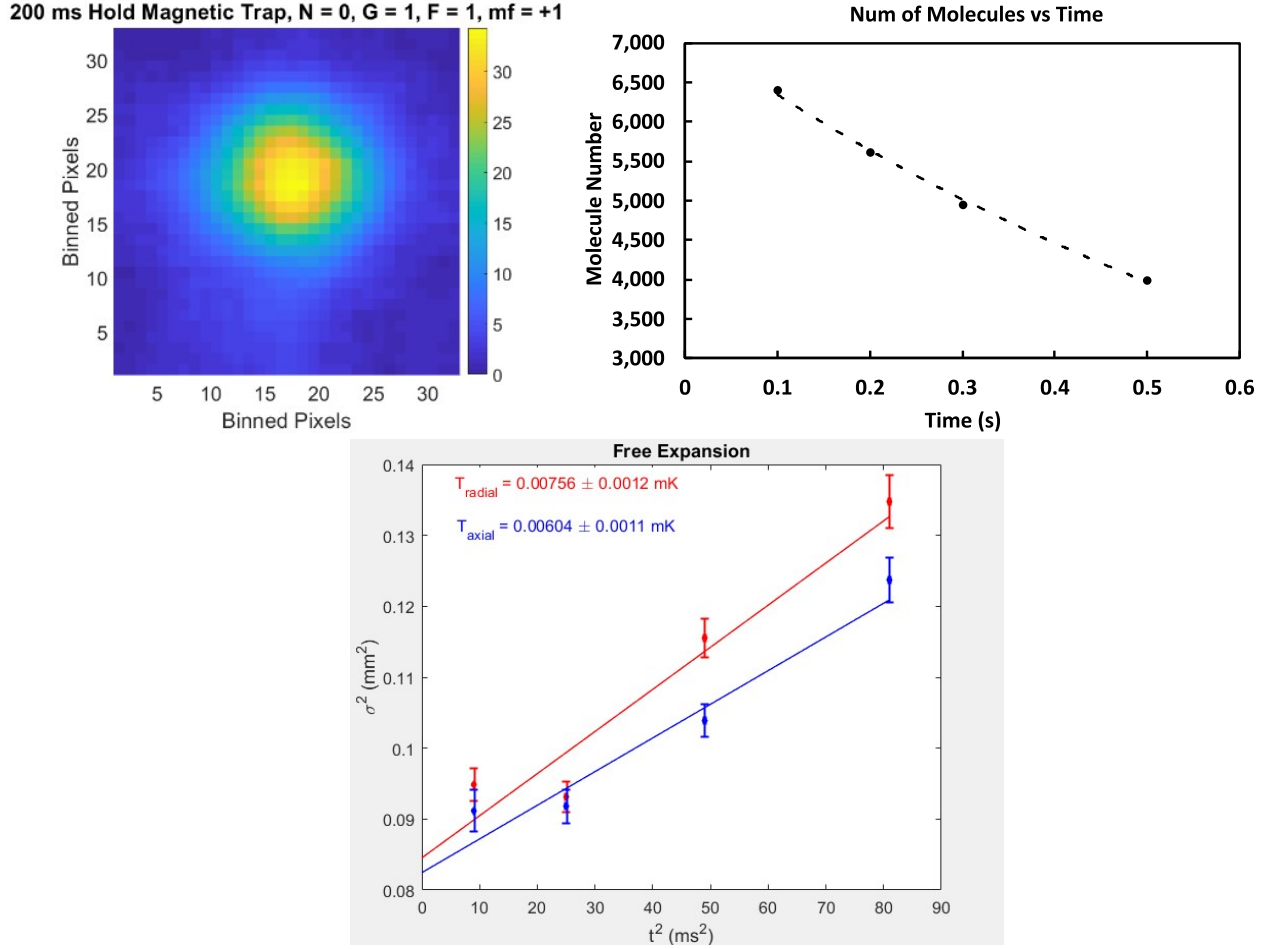


Figure 7.1: Shown is the recent results on a magnetic trap of YO molecules. A background gas limited lifetime of  $\approx 850 \text{ ms}$  is measured, and an average temperature of  $\approx 7 \mu\text{K}$  is achieved.

$$V_{\text{dipole}} = \frac{-d^2}{4\pi\epsilon_0} \frac{1 - 3\cos^2\theta}{12(\Delta^2 + \Omega^2)R^3}, \quad (7.1)$$

where  $R$  is the intermolecular distance between the molecules,  $d$  is the zero-field dipole moment,  $\Delta$  is the field detuning,  $\theta$  is the angle between the rotation axis from the microwave field and the intermolecular axis, and  $\Omega$  is the Rabi frequency. The beauty of this methodology is that you simply need to apply a sufficiently strong microwave field such that Rabi frequency is on the order of 10's of MHz without the need for large static DC fields to mix rotational states. The downside is that the polarization needs to be circular with a strong purity of around 100 left to right handedness

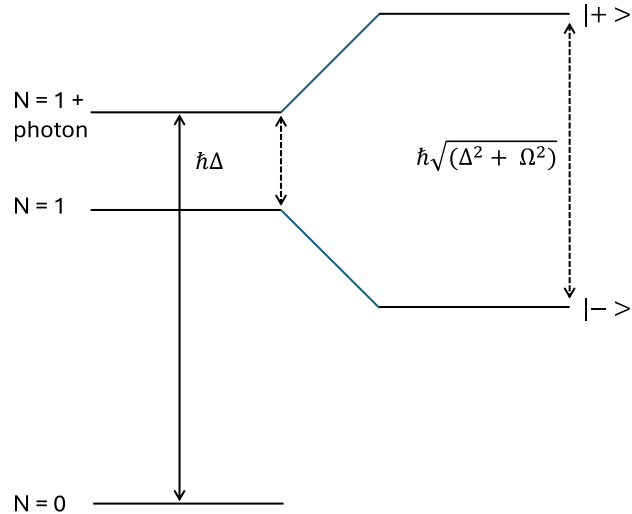


Figure 7.2: Dressing of rotational manifolds through blue-detuned microwaves.

or vice versa.

The shielding works regardless of the approach angle  $\theta$  and provides true 3D shielding. One caveat however is that at short range there can be a slight bound potential [7]. This can actually cause large three-body loss at short range in bosonic species. The demonstration of achieving degeneracy through microwave shielding in Sebastian Will's group used a  $\pi$  polarized field to tune the dipolar scattering length at short range to be relatively small vs the contact s-wave scattering length to create a stable dipolar BEC. I would like to note that a static DC field creates the same effect, but maybe with more experimental complexity.

We expect these methodologies to work well on YO where elastic to inelastic rates over a factor of 10 should be achievable and allow for evaporative cooling. However, we will be starting at a few  $\mu\text{K}$  which is hotter than most bi-alkali species before evaporation. As such, it will be imperative to increase the molecular number through several of the previously mentioned possible improvements throughout this thesis to achieve a BEC with a few thousand YO molecules.

### 7.3 Narrowline-Cooling of YO Molecules

The last prospect I would like to discuss is that of narrowline cooling of YO molecules which is also underway currently on the experiment. As stated previously the lifetime of the  $A^2\Delta_{3/2}, J = 3/2^\pm$  state is  $23 \mu\text{s}$ . This provides a tantalizing prospect for recoil-limited Doppler cooling similar to that used with great success in alkaline earth atomic species.

However, in YO it is much more complicated due to the large branching from this state. As a reminder the allowed branching from the delta state is  $A^2\Delta_{3/2}, J = 3/2^\pm \rightarrow X^2\Sigma^+, N = 0^+, 1^-, 2^+, 3^-$  if there are stray fields present that can polarize the molecules. As shown in Fig.2.14, fields of around  $1 \text{ V/cm}$  are detrimental. The current plan is to apply a few  $\text{V/cm}$  field and perform cooling on the pure parity stark states  $m_f = 0$  which do not have a linear stark shift at these small fields as per Eq.2.14. This has the advantage of reducing the branching to certain hyperfine manifolds and rotational manifolds as there is no mixing of the parity doublets in these states.

The current methodology is to apply a laser addressing  $X^2\Sigma^+, G = 1, F = 0, m_f = 0 \rightarrow A^2\Delta_{3/2}, J = 3/2^+, F = 1, m_f = 0$  this will allow a few photons to be scattered with around  $1 \mu\text{K}$  in temperature reduction. While this might not seem like a lot, the molecules are already  $1.5 \mu\text{K}$  in free space and around  $4 \mu\text{K}$  in a crossed dipole trap. So any temperature reduction will be very beneficial to the evaporative cooling efficiency.

One problem however is that the differential stark shifts between the delta state and the ground state from the trapping light at  $1064 \text{ nm}$  is quite egregious, and we have seen line broadening on the order of  $100$ 's of  $\text{kHz}$ . So the current plan is to perform the cooling in free space first and hope to create a magic trapping condition which could be created by seeding our ytterbium fiber amplifiers with a different seed. With the new seed the  $A^2\Delta_{3/2}, J = 3/2^+ \rightarrow D^2\Sigma^+$  and the  $X^2\Sigma^+, N = 1^-, G = 1, F = 0, m_f = 0 \rightarrow A^2\Pi_{1/2,3/2}$  transitions would be simultaneously driven which would match trap depths in the excited state and the ground state. This could be quite powerful in the future for resolved sideband cooling of the molecules in a 1D optical lattice.

## Bibliography

- [1] R. J. Ackermann, E. G. Rauh, and R. J. Thorn. Thermodynamic Properties of Gaseous Yttrium Monoxide. Correlation of Bonding in Group III Transition-Metal Monoxides. The Journal of Chemical Physics, 40(3):883–889, 02 1964.
- [2] ACME-Collaboration. Improved Limit on the Electric Dipole Moment of the Electron. Nature, 562:355–360, Oct 2018.
- [3] Loïc Anderegg, Benjamin L. Augenbraun, Eunmi Chae, Boerge Hemmerling, Nicholas R. Hutzler, Aakash Ravi, Alejandra Collopy, Jun Ye, Wolfgang Ketterle, and John M. Doyle. Radio frequency magneto-optical trapping of caF with high density. Phys. Rev. Lett., 119:103201, Sep 2017.
- [4] A. Aspect, E. Arimondo, R. Kaiser, N. Vansteenkiste, and C. Cohen-Tannoudji. Laser cooling below the one-photon recoil energy by velocity-selective coherent population trapping: theoretical analysis. J. Opt. Soc. Am. B, 6(11):2112–2124, Nov 1989.
- [5] Yicheng Bao, Scarlett S. Yu, Loïc Anderegg, Eunmi Chae, Wolfgang Ketterle, Kang-Kuen Ni, and John M. Doyle. Dipolar spin-exchange and entanglement between molecules in an optical tweezer array, 2022.
- [6] A. Bernard and R. Gravina. The emission spectrum of yttrium monoxide - New rotational and vibrational results on the A2Pi-X2Sigma+ system. , 52:443–450, August 1983.
- [7] Niccolò Bigagli, Weijun Yuan, Siwei Zhang, Boris Bulatovic, Tijs Karman, Ian Stevenson, and Sebastian Will. Observation of Bose-Einstein Condensation of Dipolar Molecules, 2023.
- [8] B.H. Bransden and C.J. Joachain. Physics of Atoms and Molecules. Pearson Education. Prentice Hall, 2003.
- [9] John M. Brown and Alan Carrington. Rotational Spectroscopy of Diatomic Molecules. Cambridge Molecular Science. Cambridge University Press, 2003.
- [10] H. P. Büchler, E. Demler, M. Lukin, A. Micheli, N. Prokof'ev, G. Pupillo, and P. Zoller. Strongly Correlated 2D Quantum Phases with Cold Polar Molecules: Controlling the Shape of the Interaction Potential. Phys. Rev. Lett., 98:060404, Feb 2007.
- [11] Justin J. Burau, Parul Aggarwal, Kameron Mehling, and Jun Ye. Blue-detuned magneto-optical trap of molecules. Phys. Rev. Lett., 130:193401, May 2023.

- [12] Justin J. Bureau, Kameron Mehling, Matthew D. Frye, Mengjie Chen, Parul Aggarwal, Jeremy M. Hutson, and Jun Ye. Collisions of spin-polarized yo molecules for single partial waves. Phys. Rev. A, 110:L041306, Oct 2024.
- [13] Jin Cao, Huan Yang, Zhen Su, Xin-Yao Wang, Jun Rui, Bo Zhao, and Jian-Wei Pan. Preparation of a Quantum Degenerate Mixture of  $^{23}\text{Na}^{40}\text{K}$  Molecules and  $^{40}\text{K}$  Atoms. Phys. Rev. A, 107:013307, Jan 2023.
- [14] Annette N. Carroll, Henrik Hirzler, Calder Miller, David Wellnitz, Sean R. Muleady, Junyu Lin, Krzysztof P. ZamarSKI, Reuben R. W. Wang, John L. Bohn, Ana Maria Rey, and Jun Ye. Observation of generalized t-j spin dynamics with tunable dipolar interactions, 2024.
- [15] Xing-Yan Chen, Shrestha Biswas, Sebastian Eppelt, Andreas Schindewolf, Fulin Deng, Tao Shi, Su Yi, Timon A. Hilker, Immanuel Bloch, and Xin-Yu Luo. Ultracold Field-linked Tetraatomic Molecules. Nature, Jan 2024.
- [16] Lawrence W. Cheuk, Loïc Anderegg, Benjamin L. Augenbraun, Yicheng Bao, Sean Burchesky, Wolfgang Ketterle, and John M. Doyle.  $\lambda$ -enhanced imaging of molecules in an optical trap. Physical Review Letters, 121(8), August 2018.
- [17] W. J. Childs, O. Poulsen, and T. C. Steimle. Fine and magnetic hyperfine structure in the A2 and X2+ states of yttrium monoxide. The Journal of Chemical Physics, 88(2):598–606, 01 1988.
- [18] Arthur Christianen, Tijs Karman, and Gerrit C Groenenboom. A Quasiclassical Method for Calculating the Density of States of Ultracold Collision Complexes. 100:032708, 2019.
- [19] Arthur Christianen, Martin W Zwierlein, Gerrit C Groenenboom, and Tijs Karman. Photoinduced Two-Body Loss of Ultracold Molecules. 123:123402, 2019.
- [20] Alejandra L. Collopy, Shiqian Ding, Yewei Wu, Ian A. Finneran, Loïc Anderegg, Benjamin L. Augenbraun, John M. Doyle, and Jun Ye. 3d magneto-optical trap of yttrium monoxide. Physical Review Letters, 121(21), November 2018.
- [21] J. Dalibard and C. Cohen-Tannoudji. Laser cooling below the doppler limit by polarization gradients: simple theoretical models. J. Opt. Soc. Am. B, 6(11):2023–2045, Nov 1989.
- [22] L. De Marco, G. Valtolina, K. Matsuda, W. G. Tobias, J. P. Covey, and J. Ye. A Degenerate Fermi Gas of Polar Molecules. Science, 363(6429):853–856, 2019.
- [23] Nicolò Defenu, Tobias Donner, Tommaso Macrì, Guido Pagano, Stefano Ruffo, and Andrea Trombettoni. Long-range Interacting Quantum Systems. Rev. Mod. Phys., 95:035002, Aug 2023.
- [24] D. DeMille. Quantum computation with trapped polar molecules. Phys. Rev. Lett., 88:067901, Jan 2002.
- [25] J A Devlin and M R Tarbutt. Three-dimensional doppler, polarization-gradient, and magneto-optical forces for atoms and molecules with dark states. New Journal of Physics, 18(12):123017, December 2016.

- [26] M D Di Rosa. Laser-cooling molecules. The European Physical Journal D - Atomic, Molecular, Optical and Plasma Physics, 31(2):395–402, November 2004.
- [27] Shiqian Ding, Yewei Wu, Ian A. Finneran, Justin J. Burau, and Jun Ye. Sub-doppler cooling and compressed trapping of yo molecules at  $\mu\text{K}$  temperatures. Phys. Rev. X, 10:021049, Jun 2020.
- [28] R; GERZ C; WALLIS H; ASPECT A; COHEN-TANNOUJDI C EMILE, O; KAISER. Magnetically assisted sisyphus effect. Journal de physique. II, 1993.
- [29] W. Ertmer, R. Blatt, J. L. Hall, and M. Zhu. Laser manipulation of atomic beam velocities: Demonstration of stopped atoms and velocity reversal. Phys. Rev. Lett., 54:996–999, Mar 1985.
- [30] Matthew D. Frye, Paul S. Julienne, and Jeremy M. Hutson. Cold atomic and Molecular Collisions: Approaching the Universal Loss Regime. New J. Phys., 17:045019, 2015.
- [31] B. Gao. General Form of the Quantum-defect Theory for  $-1/r^\alpha$  Type of Potentials with  $\alpha > 2$ . Phys. Rev. A, 78:012702, 2008.
- [32] K. Góral, L. Santos, and M. Lewenstein. Quantum Phases of Dipolar Bosons in Optical Lattices. Phys. Rev. Lett., 88:170406, Apr 2002.
- [33] Mingyang Guo, Bing Zhu, Bo Lu, Xin Ye, Fudong Wang, Romain Vexiau, Nadia Bouloufa-Maafa, Goulven Quémener, Olivier Dulieu, and Dajun Wang. Creation of an ultracold gas of ground-state dipolar  $^{23}\text{Na}^{87}\text{Rb}$  molecules. Phys. Rev. Lett., 116:205303, May 2016.
- [34] Christian Hallas, Grace K. Li, Nathaniel B. Vilas, Paige Robichaud, Loïc Anderegg, and John M. Doyle. High compression blue-detuned magneto-optical trap of polyatomic molecules, 2024.
- [35] Connor M. Holland, Yukai Lu, and Lawrence W. Cheuk. On-demand entanglement of molecules in a reconfigurable optical tweezer array. Science, 382(6675):1143–1147, December 2023.
- [36] Matthew T. Hummon, Mark Yeo, Benjamin K. Stuhl, Alejandra L. Collopy, Yong Xia, and Jun Ye. 2d magneto-optical trapping of diatomic molecules. Physical Review Letters, 110(14), April 2013.
- [37] Z. Idziaszek and P. S. Julienne. Universal Rate Constants for Reactive Collisions of Ultracold Molecules. Phys. Rev. Lett., page 113202, 2010.
- [38] K.N. Jarvis, J.A. Devlin, T.E. Wall, B.E. Sauer, and M.R. Tarbutt. Blue-detuned magneto-optical trap. Physical Review Letters, 120(8), February 2018.
- [39] Varun Jorapur, Thomas K. Langin, Qian Wang, Geoffrey Zheng, and David DeMille. High density loading and collisional loss of laser-cooled molecules in an optical trap. Physical Review Letters, 132(16), April 2024.
- [40] Mallikarjun Karra, Ketan Sharma, Bretislav Friedrich, Sabre Kais, and Dudley Herschbach. Prospects for quantum computing with an array of ultracold polar paramagnetic molecules. The Journal of Chemical Physics, 144(9):094301, 03 2016.

- [41] Thomas K. Langin, Varun Jorapur, Yuqi Zhu, Qian Wang, and David DeMille. Polarization enhanced deep optical dipole trapping of  $\Lambda$ -cooled polar molecules. Phys. Rev. Lett., 127:163201, Oct 2021.
- [42] Paul D. Lett, Richard N. Watts, Christoph I. Westbrook, William D. Phillips, Phillip L. Gould, and Harold J. Metcalf. Observation of atoms laser cooled below the doppler limit. Phys. Rev. Lett., 61:169–172, Jul 1988.
- [43] J. W.-H. Leung, Tongmei Ma, and A. S.-C. Cheung. Cavity ring down absorption spectroscopy of the  $b2\sigma^+ - x2\sigma^+$  transition of yo. Journal of Molecular Spectroscopy, 229:108–114, 2005.
- [44] J.-R. Li, K. Matsuda, C. Miller, A. N. Carroll, W. G. Tobias, J. S. Higgins, and J. Ye. Tunable Itinerant Spin Dynamics with Polar Molecules. Nature, 614:70–74, 2023.
- [45] Samuel J. Li, Connor M. Holland, Yukai Lu, and Lawrence W. Cheuk. Blue-detuned magneto-optical trap of caf molecules. Phys. Rev. Lett., 132:233402, Jun 2024.
- [46] Yu Liu, Ming-Guang Hu, Matthew A. Nichols, Dongzheng Yang, Daiqian Xie, Hua Guo, and Kang-Kuen Ni. Precision Test of Statistical Dynamics with State-to-state Ultracold Chemistry. Nature, 593(7859):379–384, May 2021.
- [47] Michael Mayle, Goulven Quéméner, Brandon P. Ruzic, and John L. Bohn. Scattering of Ultracold Molecules in the Highly Resonant Regime. Phys. Rev. A, 87:012709, Jan 2013.
- [48] Michael Mayle, Brandon P. Ruzic, and John L. Bohn. Statistical Aspects of Ultracold Resonant Scattering. Phys. Rev. A, 85:062712, Jun 2012.
- [49] H.J. Metcalf and P. van der Straten. Laser Cooling and Trapping. Graduate Texts in Contemporary Physics. Springer New York, 2012.
- [50] Peter K. Molony, Philip D. Gregory, Zhonghua Ji, Bo Lu, Michael P. Köppinger, C. Ruth Le Sueur, Caroline L. Blackley, Jeremy M. Hutson, and Simon L. Cornish. Creation of ultracold  $^{87}\text{Rb}^{133}\text{Cs}$  molecules in the rovibrational ground state. Phys. Rev. Lett., 113:255301, Dec 2014.
- [51] K.-K. Ni, S. Ospelkaus, M. H. G. de Miranda, A. Pe’er, B. Neyenhuis, J. J. Zirbel, S. Kotochigova, P. S. Julienne, D. S. Jin, and J. Ye. A high phase-space-density gas of polar molecules. Science, 322(5899):231–235, October 2008.
- [52] Kang-Kuen Ni, Till Rosenband, and David D. Grimes. Dipolar exchange quantum logic gate with polar molecules. Chem. Sci., 9:6830–6838, 2018.
- [53] E.B. Norrgard, D.J. McCarron, M.H. Steinecker, M.R. Tarbutt, and D. DeMille. Submillikelvin dipolar molecules in a radio-frequency magneto-optical trap. Physical Review Letters, 116(6), February 2016.
- [54] Nelson Darkwah Oppong. TOWARDS A DEGENERATE FERMI GAS OF STRONTIUM -87 IN A 3D OPTICAL LATTICE. Master thesis, University of Colorado, Boulder and ETH Zurich, 2015.
- [55] Jee Woo Park, Sebastian A. Will, and Martin W. Zwierlein. Ultracold dipolar gas of fermionic  $^{23}\text{Na}^{40}\text{K}$  molecules in their absolute ground state. Phys. Rev. Lett., 114:205302, May 2015.

- [56] L. Pollet, J. D. Picon, H. P. Büchler, and M. Troyer. Supersolid Phase with Cold Polar Molecules on a Triangular Lattice. *Phys. Rev. Lett.*, 104:125302, Mar 2010.
- [57] Goulven Quémener. Ultracold collisions of molecules, 2017.
- [58] Tanya S. Roussy, Luke Caldwell, Trevor Wright, William B. Cairncross, Yuval Shagam, Kia Boon Ng, Noah Schlossberger, Sun Yool Park, Anzhou Wang, Jun Ye, and Eric A. Cornell. An Improved Bound on the Electron’s Electric Dipole Moment. *Science*, 381(6653):46–50, 2023.
- [59] Timur M. Rvachov, Hyungmok Son, Ariel T. Sommer, Sepehr Ebadi, Juliana J. Park, Martin W. Zwierlein, Wolfgang Ketterle, and Alan O. Jamison. Long-lived ultracold molecules with electric and magnetic dipole moments. *Phys. Rev. Lett.*, 119:143001, Oct 2017.
- [60] T. A. Savard, K. M. O’Hara, and J. E. Thomas. Laser-noise-induced heating in far-off resonance optical traps. *Phys. Rev. A*, 56:R1095–R1098, Aug 1997.
- [61] Rahul Sawant, Jacob A Blackmore, Philip D Gregory, Jordi Mur-Petit, Dieter Jaksch, Jesús Aldegunde, Jeremy M Hutson, M R Tarbutt, and Simon L Cornish. Ultracold polar molecules as qudits. *New Journal of Physics*, 22(1):013027, January 2020.
- [62] A. Schindewolf, R. Bause, X.-Y. Chen, T. Duda, M. Karman, I. Bloch, and X.-Yu. Luo. Evaporation of Microwave-shielded Polar Molecules to Quantum Degeneracy. *Nature*, 607:677–681, 2022.
- [63] Matthias Schmidt, Lucas Lassablière, Goulven Quémener, and Tim Langen. Self-bound Dipolar Droplets and Supersolids in Molecular Bose-Einstein Condensates. *Phys. Rev. Res.*, 4:013235, Mar 2022.
- [64] Benoit Simard, Andrew M. James, Peter A. Hackett, and Walter J. Balfour. On the  $a_2-x_2+(0,0)$  band of yo. *Journal of Molecular Spectroscopy*, 154(2):455–457, 1992.
- [65] Alexander Smirnov, Victor Solomonik, Sergei Yurchenko, and Jonathan Tennyson. Spectroscopy of yo from first principles. *Physical Chemistry Chemical Physics*, 21, 10 2019.
- [66] Hyungmok Son, Juliana J. Park, Yu-Kun Lu, Alan O. Jamison, Tijs Karman, and Wolfgang Ketterle. Control of Reactive Collisions by Quantum Interference. *Science*, 375(6584):1006–1010, March 2022.
- [67] Daniel A. Steck. *Quantum and Atom Optics*. t <http://steck.us/teaching> (revision 0.8.3, 25 May 2012).
- [68] Benjamin K. Stuhl, Brian C. Sawyer, Dajun Wang, and Jun Ye. Magneto-optical trap for polar molecules. *Phys. Rev. Lett.*, 101:243002, Dec 2008.
- [69] R. D. Suenram, F. J. Lovas, G. T. Fraser, and K. Matsumura. Pulsed-nozzle Fourier-transform microwave spectroscopy of laser-vaporized metal oxides: Rotational spectra and electric dipole moments of YO, LaO, ZrO, and HfO. *The Journal of Chemical Physics*, 92(8):4724–4733, 04 1990.

- [70] R. D. Suenram, F. J. Lovas, G. T. Fraser, and K. Matsumura. Pulsed-nozzle Fourier-transform Microwave Spectroscopy of Laser-vaporized Metal Oxides: Rotational Spectra and Electric Dipole Moments of YO, LaO, ZrO, and HfO. The Journal of Chemical Physics, 92(8):4724–4733, 04 1990.
- [71] Tetsu Takekoshi, Lukas Reichsöllner, Andreas Schindewolf, Jeremy M. Hutson, C. Ruth Le Sueur, Olivier Dulieu, Francesca Ferlaino, Rudolf Grimm, and Hanns-Christoph Nägerl. Ultracold dense samples of dipolar rbc molecules in the rovibrational and hyperfine ground state. Phys. Rev. Lett., 113:205301, Nov 2014.
- [72] M R Tarbutt. Magneto-optical trapping forces for atoms and molecules with complex level structures. New Journal of Physics, 17(1):015007, jan 2015.
- [73] M. R. Tarbutt and T. C. Steimle. Modeling magneto-optical trapping of caf molecules. Phys. Rev. A, 92:053401, Nov 2015.
- [74] S. Truppe, H. J. Williams, M. Hambach, L. Caldwell, N. J. Fitch, E. A. Hinds, B. E. Sauer, and M. R. Tarbutt. Molecules cooled below the doppler limit. Nature Physics, 13(12):1173–1176, August 2017.
- [75] G. Valtolina, K. Matsuda, W. G. Tobias, J.-R. Li, L. De Marco, and J. Ye. Dipolar Evaporation of Reactive Molecules to Below the Fermi Temperature. Nature, 588:239 – 243, 2020.
- [76] N. Vanhaecke and O. Dulieu. Precision measurements with polar molecules: the role of the black body radiation. Molecular Physics, 105(11-12):1723–1731, 2007.
- [77] Nathaniel B. Vilas, Christian Hallas, Loïc Anderegg, Paige Robichaud, Andrew Winnicki, Debayan Mitra, and John M. Doyle. Magneto-optical trapping and sub-doppler cooling of a polyatomic molecule. Nature, 606(7912):70–74, June 2022.
- [78] T. E. Wall, J. F. Kanem, J. J. Hudson, B. E. Sauer, D. Cho, M. G. Boshier, E. A. Hinds, and M. R. Tarbutt. Lifetime of the  $a(v' = 0)$  state and franck-condon factor of the  $a-x(0-0)$  transition of caf measured by the saturation of laser-induced fluorescence. Phys. Rev. A, 78:062509, Dec 2008.
- [79] Matthias Weidemüller, T. Esslinger, M. Ol’shanii, A. Hemmerich, and Theodor Haensch. A novel scheme for efficient cooling below the photon recoil limit. EPL (Europhysics Letters), 27:109, 07 2007.
- [80] H J Williams, S Truppe, M Hambach, L Caldwell, N J Fitch, E A Hinds, B E Sauer, and M R Tarbutt. Characteristics of a magneto-optical trap of molecules. New Journal of Physics, 19(11):113035, November 2017.
- [81] Yewei Wu, Justin J. Bureau, Kameron Mehling, Jun Ye, and Shiqian Ding. High phase-space density of laser-cooled molecules in an optical lattice. Phys. Rev. Lett., 127:263201, Dec 2021.
- [82] S. F. Yelin, K. Kirby, and Robin Côté. Schemes for robust quantum computation with polar molecules. Physical Review A, 74(5), November 2006.
- [83] Mark Yeo. The Laser Cooling and Magneto-Optical Trapping of the YO Molecule. Phd thesis, University of Colorado, Boulder, 2015.

- [84] Chaoqun Zhang, Hannah Korlund, Yewei Wu, Shiqian Ding, and Lan Cheng. Towards accurate prediction for laser-coolable molecules: Relativistic coupled-cluster calculations for yttrium monoxide and prospects for improving its laser cooling efficiencies. Physical Chemistry Chemical Physics, 22:26167–26177, 11 2020.
- [85] Deping Zhang, Qiang Zhang, Boxing Zhu, Jingwang Gu, Bingbing Suo, Yang Chen, and Dongfeng Zhao. High-resolution electronic spectra of yttrium oxide (YO): The  $D2^+-X2^+$  transition. The Journal of Chemical Physics, 146(11):114303, 03 2017.

ProQuest Number: 31635624

INFORMATION TO ALL USERS

The quality and completeness of this reproduction is dependent on the quality and completeness of the copy made available to ProQuest.



Distributed by  
ProQuest LLC a part of Clarivate ( 2024).  
Copyright of the Dissertation is held by the Author unless otherwise noted.

This work is protected against unauthorized copying under Title 17,  
United States Code and other applicable copyright laws.

This work may be used in accordance with the terms of the Creative Commons license  
or other rights statement, as indicated in the copyright statement or in the metadata  
associated with this work. Unless otherwise specified in the copyright statement  
or the metadata, all rights are reserved by the copyright holder.

ProQuest LLC  
789 East Eisenhower Parkway  
Ann Arbor, MI 48108 USA